CZECH TECHNICAL UNIVERSITY IN PRAGUE

FACULTY OF CIVIL ENGINEERING

DOCTORAL THESIS

2023

SVITLANA KALMYKOVA

CZECH TECHNICAL UNIVERSITY IN PRAGUE

Faculty of Civil Engineering

Department of Steel and Timber Structures

Rectangular Hollow T-shaped Joint with Eccentricity

DOCTORAL THESIS

Ing. Svitlana Kalmykova

Doctoral study programme: Civil Engineering

Branch of study: Building and Structural Engineering

Doctoral thesis tutor: Prof. Ing. František Wald, CSc.

Prague, 2023

CZECH TECHNICAL UNIVERSITY IN PRAGUE
Faculty of Civil Engineering
Thákurova 7, 166 29 Praha 6

DECLARATION

Ph.D. student's name: Ing. Svitlana Kalmykova

Title of the doctoral thesis: Rectangular Hollow T-shaped Joint with Eccentricity

I hereby declare that this doctoral thesis is my own work and effort written under the guidance of the tutor Prof. Ing. František Wald, CSc..
All sources and other materials used have been quoted in the list of references.

The doctoral thesis was written in connection with research on the project:

In Prague on 25.08.2023

signature

ABSTRACT

The study addresses the lack of design techniques for welded rectangular hollow section (RHS) connections with offsets, where one branch is laterally shifted from the chord centreline. The research involves experimental and numerical analyses of welded T-joints using specific RHS. Various offsets and component sizes are tested in experiments, alongside steel strip coupon tests, and the results are thoroughly discussed.

Numerical models are created in Abaqus, considering nonlinearities, mesh size effects, and weld characteristics. These models are validated against full-scale laboratory tests. The resulting load-displacement curves for different joint geometries are analysed, focusing on failure modes and offset values. An analytical model is also developed to estimate the plastic resistance of the offset RHS T-shaped connection. This model is an extension of a plastic mechanism model for traditional stepped RHS T-connections and is verified against non-linear numerical simulations.

The proposed analytical model provides reliable predictions for yield and ultimate loads in offset connections. It's compared with other analytical methods and demonstrates accurate yield load computations, even for connections with matched faces of the chord web and brace lateral surface. Overall, the research contributes valuable insights into the behaviour of offset RHS connections and offers practical design tools for such cases.

ABSTRAKT

Studie se zabývá nedostatečnými technikami návrhu svařovaných spojů obdélníkových dutých profilů (RHS) s odsazením, kde je svislice odchýlena od osy pásnice. Výzkum zahrnuje experimentální a numerickou analýzu svařovaných T-spojů s použitím uzavřených čtvercových profilů. V rámci experimentů jsou testovány různé hodnoty odsazení a rozměry prvků, spolu s materiálovými testy ocelových vzorků, a výsledky jsou důkladně diskutovány.

Numerické modely jsou vytvořeny v programu Abaqus s ohledem na nelinearity, vliv velikosti KP sítě a charakteristiky svarů. Tyto modely jsou ověřeny na základě zkoušek v laboratoři v plném měřítku. Výsledné deformační křivky pro různé geometrie spojů jsou analyzovány s důrazem na způsoby selhání a hodnoty odsazení. Analytický model je také vyvinut k odhadu plastické odolnosti T spoje obdélníkových dutých profilů. Tento model je rozšířením plastického mechanismu pro tradiční T-spoje RHS a je ověřen proti nelineárním numerickým simulacím.

Navržený analytický model poskytuje spolehlivé predikce pro mez kluzu a mez pevnosti u spojů s odsazením. Je porovnán s dalšími analytickými metodami a prokazuje přesné výpočty mezního zatížení, dokonce i pro spoje se stejnou šířkou profilů. Celkově výzkum přináší cenné poznatky o chování spojů z RHS profilů s odsazením a nabízí praktické návrhové nástroje pro tyto případy.

ACKNOWLEDGEMENT

I would like to express my sincere gratitude to my supervisor, Prof. Ing. František Wald, CSc., for his invaluable suggestions, advice, and inspiration throughout the completion of this thesis. His guidance has been instrumental in shaping this research.

In addition, I extend my heartfelt thanks to my husband, Yuriy Kalmykov, CSc., who has been my invaluable source of support. I am deeply appreciative of his professional counsel, assistance, dedication, and patience, and for unwavering belief in me.

Furthermore, I want to thank my parents Yurii and Liubov Kaida for their unwavering belief in me. Their faith has fuelled my determination to pursue my educational and personal goals.

I would also like to express my gratitude to my children, Mark and Herman, who have patiently awaited my graduation and have been my driving force.

I extend my thanks to Illia Tkalenko, PhD, for his assistance during my initial steps in the university and for his friendship, which I deeply appreciate.

I would like to extend my gratitude to Roman Kotora, who generously assisted with the printing of this thesis.

Last but not least, I would also like to express my appreciation to the dedicated department staff who provided invaluable assistance with administrative paperwork, as well as to the diligent laboratory workers who played a crucial role in ensuring the seamless progress of our testing procedures. Your collective efforts have been instrumental in the successful completion of this thesis, and I am truly thankful for your support and contributions.

The thesis was partially written in Žilina Technical University in Žilina, Slovakia under CEEPUS freemover programme.

Also, it was partially performed under student grant SGS22/141/OHK1/3T/11 by CTU in Prague.

https://doi.org/10.14311/dis.fsv.2023.014

TABLE OF CONTENT

LIST OF FIGURES

LIST OF TABLES

NOTATION

ABBREVIATIONS

CIDECT	Comité International pour le Développement et l'Étude de la Construction Tubulaire
CBFEM	Component-Based Finite Element Method
CHS	Circular Hollow Section
DT	Directly Transferred [braces] (Chapter 2.3)
IIW	International Institute of Welding
IPB	In-plane Bending Moment
FE	Finite Element
FEA	Finite Element Analysis
FEM	Finite Element Model
HSS	Hollow Structural Steel; Hot-Spot Stress (Chapter 2.2.3)
OPB	Out-of-plane Bending Moment
RHS	Rectangular Hollow Section
SCE	Stepped Connection with Eccentricity
SHS	Square Hollow Section
SCF	Stress Concentration Factor
SNCF	Strain/stress Concentration Factor
V&V	Validation and Verification

LIST OF SYMBOLS

The symbols are introduced in relevant chapters. The terminology and symbols follow the rules applied in EN1993-1-8:2006. The major general variables are described below.

$F_{N,minRd}$	is	the minimum resistance of the active components (a)..(e) for joint under axial force
$M_{ip,i,Rd}$	is	the design value of the resistance of the joint, expressed in terms of the in-plane internal moment in brace *i* (*i* = 0, 1, 2 or 3)
$M_{ip,i,Ed}$	is	the design value of the in-plane internal moment in brace *i* (*i* = 0, 1, 2 or 3)
$N_{i,Rd}$	is	the design value of the resistance of the joint, expressed in terms of the internal axial force in brace *i* (*i* = 0, 1, 2 or 3)
$N_{i,Ed}$	is	the design value of the internal axial force in brace *i* (*i* = 0, 1, 2 or 3)

Q_f	is	the chord load function
P_{max}	is	the peak load
P_{ult}	is	the ultimate load
$P_{1\%b_0}$		the load taken at the serviceability deformation limit of $1\%b_0$
$P_{3\%b_0}$		the load taken at the ultimate deformation limit of $3\%b_0$
a_w	is	the effective throat thickness of fillet weld
b_0	is	the main chord width
b_e	is	the effective width of the brace
$b_{e.p.}$	is	the effective width of the brace for punching shear model
f_{y0}	is	the yield strength of the chord
f_{y1}	is	the yield strength of the brace
h_1	is	the height of the brace
n	is	the loading ration for fire resistance
r_{ext}	is	the chord's external corner radius
t_0	is	the chord thickness
Δ	is	the global displacement
Δ_w	is	the web deformation
α	is	the length-to-diameter ratio for CHS
β	is	the width-to-width ratio for RHS
		the diameter-to-thickness ratio for CHS
γ	is	the chord width-to-double-thickness ratio
η	is	the ring-to-chord width ratio
λ	is	the width ratio
θ	is	the outer brace inclination angle
μ_0	is	the chord width-to-thickness ratio
μ_1	is	the brace width-to-thickness ratio
τ	is	the brace-to-chord thickness ratio

CHAPTER 1: INTRODUCTION

1.1 STRUCTURAL APPLICATION OF HHS, DISCUSSION OF THEIR ADVANTAGES AND INEFFICIENCIES

In 1952, Stewarts and Lloyds produced the first rectangular hollow sections (RHS), marking the inception of the widespread usage of RHS structural members in modern construction and opening new vistas in the field of steel structures. In essence, steel structural hollow sections (HSS), whether circular (CHS), square (SHS), or rectangular (RHS), inherently exhibit higher efficiency as load-bearing components compared to other structural steel sections like I-, H-, or L-sections. This efficiency is owing to their geometric configuration. The production technologies for HSS profiles, now refined to perfection, coupled with contemporary architectural trends, fulfil specific requirements for both aesthetic appeal and the efficiency of long-span roofs and supporting systems in various buildings, as illustrated in Figure 1.1 and Figure 1.2. Consequently, HSS finds numerous applications in high-rise structures, earthquake-resistant buildings, halls, bridges (refer to Figure 1.3), towers, and specialized installations such as sign gantries, parapets, cranes, jibs, sculptures, and more.

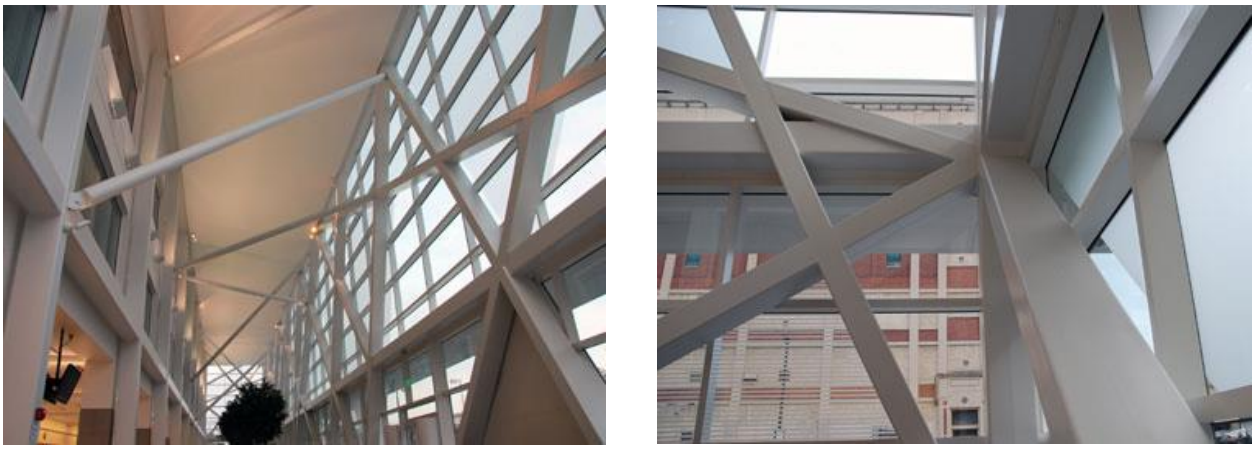

Figure 1.1 Examples of SHS application in bearing structures of transit terminals in Wiskonsine (USA) and in Milwaukee (USA)

Figure 1.2 Examples of RHS application in dome welded truss steel structure roofs (China)

Figure 1.3 Examples of RHS application in bridges
(left - Pedestrian bridge in Scotland (GB), right - Passage between buildings in CVUT (Czech Republic)

The structural benefits of HSS members, particularly in load-bearing situations involving compression or torsion, have become evident to architects and designers. Circular hollow sections (CHS) possess an aesthetically pleasing form and offer an efficient distribution of steel around centroid axes, along with minimal resistance to fluid flow and a smaller surface area compared to their I-section counterparts. However, it's important to note that fabricating joints for CHS is more expensive than for SHS and RHS. Even though electric-arc welding is a cost-effective method to connect HSS members, CHS joints often require profile cutting of tube ends, especially when tubes need to be directly fitted together. This process can be more complicated, involving varying bevels for welding access as one progresses around the tube. In cases where automated equipment isn't available, semi-automatic or manual profile cutting becomes necessary, which is more expensive than the simpler bevel cuts used for RHS. As a result, rectangular hollow sections (RHS) have emerged as a practical alternative. They allow for easy connections to the flat face and have gained popularity for use in columns and trusses.

Despite HSS members having a higher price per unit weight compared to I-section members, their greater efficiency leads to lower overall weight. This, in turn, results in reduced costs for HSS compression members compared to I-section members with similar properties. HSS is, therefore, an ideal and cost-effective choice for columns or truss members where approximately 50% of the members experience compression forces. The lighter weight of HSS also brings advantages such as decreased transportation expenses, lower erection costs, smaller foundation sizes, and reduced resource consumption, promoting sustainability.

Furthermore, the reduced surface area of HSS, in comparison to I-sections, leads to lower painting expenses and generally reduced costs for fire and corrosion protection. The absence of re-entrant corners simplifies the application of paint or fire protection, enhancing durability. RHS and SHS members, when closed at the ends, require painting on only four surfaces, whereas an I-section has eight flat surfaces requiring painting. Additionally, HSS members exhibit lower drag coefficients affecting wind and water forces. The interior space of HSS members can be utilized

for connection stiffening or internal fire protection, contributing to multifunctional designs. Being closed sections, HSS members possess inherent torsional strength far exceeding that of open sections – approximately 200 times for members of similar mass as per Wardenier et al. [145]. The substantial torsional rigidity of hollow sections plays a key role in preventing lateral buckling, resulting in improved buckling coefficients. As a consequence of joint end fixity and the members' exceptional torsional resistance, the bracing within lattice girders formed by hollow sections can be designed with an effective buckling length that's smaller than the length of the system or member intersections. Hollow structural sections offer the most efficient utilization of steel cross-sections in compression for truss members that experience primarily axial loads.

Connections between HSS members are often the most crucial and sensitive aspects of load-bearing steel structures. Despite the availability of modern building codes and guidelines like EN1993-1-8 (2005), ANSI/AISC 360-05 (2005), and CSA-S16-09 (2009), there are still gaps in knowledge concerning HSS connection analysis and design. Issues such as fire resistance, initial stresses, and stiffness estimations for various types of HSS joints lack comprehensive scientific solutions. An additional challenge for structural researchers involves offset joints, where HSS branch members are eccentrically welded and connections are shifted towards an open chord end. While offset connections are not extensively used in modern structural applications, studying their behaviour is vital for scenarios outside the scope of existing building standards in various countries, including the EU and the USA.

The current research aims to evaluate existing design guidelines for analysing and designing RHS connections, particularly T-type connections involving RHS members. The goal is to understand their foundations and propose a design approach for offset connections involving eccentrically welded joints, where the brace is shifted away from the chord's centreline towards its web. While the research includes experimental investigations within the scope of the thesis program, a significant focus is placed on validating finite element method (FEM) models of joints and conducting parametric studies. A substantial portion of the thesis is dedicated to developing an analytical model for estimating bearing capacity and stiffness, along with providing practical design recommendations for the studied eccentrically welded joints.

1.2 CONNECTION GEOMETRY

The practice of employing connections with a brace offset from the chord centreline toward its web is a frequent occurrence in the construction of load-bearing structures. Such instances arise when it's necessary to establish a shared surface that accommodates both the structural members and facade or finishing materials, or situations might arise where adhering to a coaxial design logic is not feasible due to specific constraints. In these scenarios, designers are compelled to shift brace members, which usually have smaller dimensions, away from the centrelines of the chord members.

The primary focus of this study centres around welded connections involving RHS structural members. Particularly, the investigation is focused on connections characterized by lateral offsets, specifically cases where the brace member is shifted toward the chord's lateral surface. In accordance with the terminology proposed by Bu, Wei, and Packer [11], a welded RHS connection with an offset from the chord centreline towards the chord web is referred to as a "laterally offset connection." In the scope of the present study, the scenario where one side of the branch aligns with a chord sidewall is considered a specific instance within a broader framework. This framework involves a defined separation between the surfaces of the brace and the chord, equal to the summation of the chord's external corner radius r_{ext} and the weld leg a_w, as illustrated in Figure 1.4. To simplify nomenclature, this type of RHS connection is commonly referred to as a "stepped connection with eccentricity" (SCE).

Geometrical parameters:

$\beta = b_1/b_0$ is width-to-width ratio;

$\mu_0 = b_0/t_0$ is chord width-to-thickness ratio;

$\gamma = b_0/2t_0$ is chord width-to-double-thickness ratio;

$\mu_1 = b_1/t_1$ is brace width-to-thickness ratio.

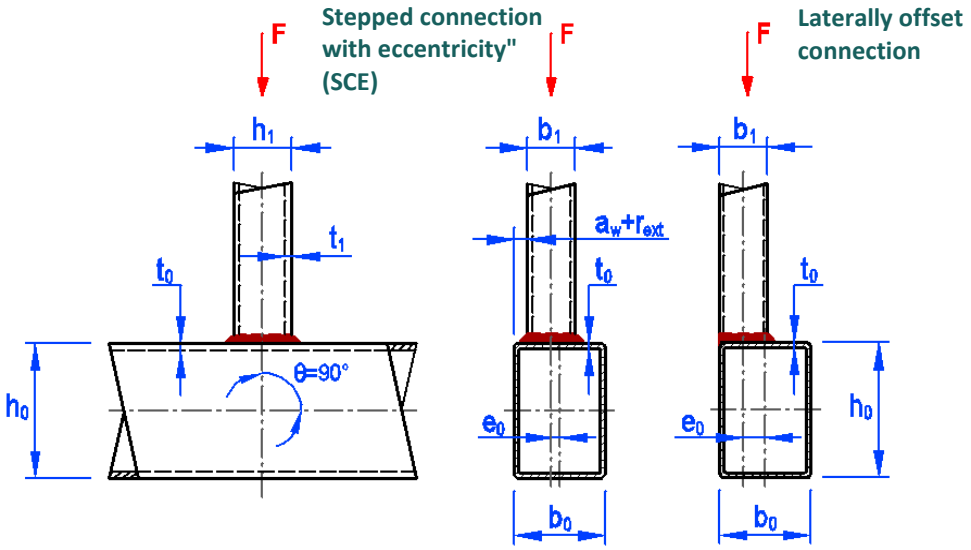

Figure 1.4 Geometry of Welded Offset RHS T-Connections

1.3 THESIS LAYOUT

This research project aims to validate and potentially improve the existing design guidelines for eccentrically welded T-type connections of RHS members within lattice steel structures. The study encompasses various phases, including experimental investigations, the development and validation of numerical finite element models against experimental data, numerical simulations

to expand the database, and the formulation of design recommendations based on the simulation results.

Chapter 2 presents a comprehensive review of pertinent research and current design guidelines. This review delves into historical and contemporary methods for assessing the ultimate limit state of connections between RHS structural members that lack a clearly defined yield capacity. It also explores the origins and specifics of present design guidelines. Additionally, a thorough examination of scientific papers published in the last few decades was conducted to outline the research objectives. The emphasis here was on papers involving numerical simulations of structural behaviour and experimental data. A key takeaway from this chapter is the dearth of studies focused on the behaviour of eccentrically welded structural connections, as well as the absence of a comprehensive analytical model for evaluating their structural resistance.

Chapter 3 outlines the specific goals and intentions of the study.

Chapter 4 provides an overview of the experimental program, which involves testing full-scale specimens primarily aimed at validating finite element (FE) models in subsequent phases. Detailed information regarding the specimens, methodology, test procedures, and experimental outcomes is presented in this chapter.

Chapter 5. To establish the applicability of nonlinear numerical finite element models and create a comprehensive numerical test database, a rigorous study was conducted to validate FE models using specimens and connections not included in the experimental program. These FE models, developed using the ABAQUS finite element software, accurately represent nonlinear geometric and material properties of the experimental connections. Moreover, a fracture criterion was applied to replicate the ultimate connection failure mode for both tension and compression-loaded connections. The validation process involved comparing FE model results with experiments in terms of overall load-displacement behaviour, local load-displacement behaviour, and ultimate failure mechanisms.

Chapter 6 introduces an analytical model based on plastic failure mechanisms, accompanied by design recommendations for T-connections with offset branches.

Chapter 7 provides a summary of these findings along with conclusions about connection behaviour. The impact of the proposed design recommendations is illustrated through comparisons with existing design guidelines and techniques, indicating whether the proposed expressions offer higher or lower connection capacities.

CHAPTER 2:
State-of-the-art

2.1 GENERAL DESCRIPTION

The widespread utilization of lattice HSS steel structures, particularly in the construction of roof systems, bridges, and offshore platforms, has led to extensive studies on the mechanical behaviour of their structural member connections over the past three decades. Despite the advancement of FEM-based computational analysis techniques, the derivation and evolution of simple and easily comprehensible criteria for evaluating strength and stiffness remain crucial in the overall scope of investigations.

The significant surge in research focused on HSS joint behaviour can be traced back to the early 1960s, driven by the indisputable benefits of HSS members, coupled with improvements in fabrication technologies and advancements in welding techniques for their connections in structures. Starting from 1965, preliminary tests on RHS connections were conducted by Stewarts and Lloyds and Redwood. A comprehensive exploration in this realm was initiated in the Netherlands in 1970. By 1973, an extensive research program was formulated by the Dutch Study Group SG-TC-18 3 in collaboration with the Joint Group of CIDECT (Comité International pour le Développement et l'Étude de la Construction Tubulaire). This initiative aimed to bridge existing knowledge gaps, compare data and formulae, and address the practical challenges of HSS joints.

As previous theoretical investigations had encountered limitations, the program focused largely on experimentation, encompassing approximately 450 joint tests. The ultimate objective was to establish recommendations and specifications for joints comprising various types of hollow sections and combinations of hollow and open sections. The culmination of these efforts resulted in the publication of the seminal work "Hollow section joints," authored by Wardenier in 1982 [141]. This pioneering book was rooted in the research conducted by the Dutch Study Group "Tubular structures" (Group SG-TC-18 3), providing a framework for assessing the design strength of CHS and RHS joints with an acceptable level of accuracy for engineering applications. "Hollow section joints" became a paradigm of thorough investigations and a catalyst for subsequent enhancements in the field of HSS joint design.

Preliminary research revealed that many HSS connection types undergo significant chord deformation and plasticization when subjected to relatively modest branch member loads. Consequently, connection deformation often surpasses practical thresholds well before conventional ultimate failure through factors like punching shear or other fracture criteria. In addition to the substantial connection deformation, behavioural non-linearity, which precludes a clear ultimate load point, prompted researchers to develop unconventional methods for determining serviceability and ultimate limit states.

Design recommendations that outline connection capacity and the primary failure modes are derived from theoretical models, experimental investigations, numerical analyses, and often a combination of these approaches. These design guidelines undergo a process of evolution over time, driven by advancements in analytical techniques, the application of novel theoretical models, and shifts in trends within international organizations responsible for publishing such recommendations.

The scope of design guidelines also expands to accommodate new fabrication methods, material properties, and emerging connection types developed by both industry and academia. In the process of developing new or refined design guidelines, it becomes crucial to examine the foundation laid by past recommendations. Thus, the second section of this chapter delves into the origins of the present design recommendations for hollow section (RHS) joints.

Given that this research aims to contribute to the development of design recommendations for both types of eccentrically welded RHS member connections in lattice structures, it is pertinent to concentrate the literature review on the origins of ultimate limit state criteria, the evolution of design codes, and the methodology used in the research of RHS member connections. This chapter provides comprehensive summaries and discussions of each of these topics in meticulous detail.

2.2 EXPERIMENTAL INVESTIGATIONS

During the last two decades of the previous century, experimental research played a crucial role in the formulation of design equations for both steel structural members and their connections. Frequently, the behaviour observed in experimental tests served as the foundation for the development of analytical models. However, the significance of experimental investigations in the field of steel structure design has diminished considerably in recent times. Typically, insights gained from experiments are now mainly utilized for validation and verification (V&V) studies within the framework of the System Response Quantity (SRQ) process, as comprehensively described by Kwasniewski and Bojanowski (2015) [59]. Experimental studies specifically focused on the strength and deformation of T-joints are not prominently featured in the papers examined below, and in many publications, they are supplemented by subsequent analytical analyses or validated using numerical models.

According to Wardenier (1982) [141], the initial tests on RHS structural member connections were conducted by Stewarts and Lloyds and Redwood (as reported in 1965). These early tests were followed by additional investigations in the UK and Germany during the 1960s, driven by the emergence of RHS profiles in the construction market. The contemporary repository of experimental research into the behaviour of welded HSS joints under various loading conditions is diverse and encompasses well-known test series conducted by research groups led by Wardenier (1982) [141] and Zhao & Hancock (1990) [155]. These test series are regarded as

foundational for RHS member T-joints and have formed the basis for the development of current building codes for connection design. In the same vein, it is worth noting additional tests carried out by Yu. Y. (1997) [153], and Lip et al. (2006) [69], which further contributed to this body of knowledge.

In the last decade, a fresh wave of experimental investigations into welded RHS T-type connections has been undertaken by Kvocak et al. (2010, 2012) [57], [58], Nizer et al. (2016) [90], Beque et al. (2017) [8], and Bu et al. (2021) [11]. This continued interest in experimental research on T-joints involving RHS structural members underscores the ongoing importance of such studies.

2.2.1 Modes and criteria governing the failure of T-type connections

The main purposes of experimental research on HSS joints, in general, are the study of behavioural phenomena and the definition of numerical characteristics of local and overall deformations, their relation to the applied forces, as well as the identification of failure modes of the test pieces. The failure modes obtained in the tests provide a strong basis for the development of analytical models for joint analysis and criteria for the failure of the joints.

Based on the results of numerous tests conducted by Wardenier (1982) [141] and Zhao & Hancock (1990) [156], four primary modes of failure for RHS T-joints were established, and a strict dependence of these failure modes on the geometrical parameters was experimentally revealed. According to the book by Wardenier et al. (2010) [145], the following distinctions are made for T-joints:

Plastic Failure (*a*-mode): Plasticization or plastic deformation of the chord face under the adjusting brace member.

Chord Side Wall Bearing or Local Buckling Failure (*b*-mode): Local buckling or bearing failure of the chord side wall under compression from the brace.

Punching Shear (*c*-mode): Punching shear of the chord face around a brace member under both compression and tension.

Rupture or Uneven Load Distribution (*d*-mode): Rupture of the tension brace or its welds due to uneven load distribution or local buckling of the compression brace.

Similar failure modes are described by Packer et al. in the "Design guide for rectangular hollow section (RHS) joints under predominantly static loading," published in 2009 under the aegis of CIDECT [99]. Drawn from Wardenier's test findings, these modes demonstrate that, in general, the *a*-mode failure occurs for joints with small to medium width-to-width ratios (β). For medium β ratios (0.6 to 0.8), this mode typically co-occurs with cracking in the chord or bracing (*d*-mode) in K- or N-joints. Local buckling (*b*-mode) is especially prominent in joints with high chord width-

to-double-thickness ratios (γ) and high β ratios. Additionally, in T-, Y-, and X-joints with $\beta = 1.0$, it can also occur in the side walls of the chord at lower chord height-wall thickness ratios.

Based on a detailed overview of test results referenced by Zhao (2000) [160], three primary failure modes for T-joints are identified: web buckling failure (*b*-mode), chord flange failure (*a*-mode), and branch local buckling failure (*d*-mode). The branch local buckling failure mode (*d*-mode) is similar to what is observed in a stub column test; therefore, it is not considered in the resistance analysis of the T-joint chord. The general conclusions drawn from the tests suggest that a clear peak load is typically found for the web buckling failure mode, while the chord flange failure mode usually exhibits a post-yield response due to the influence of membrane forces in the chord and strain hardening of the material.

In the tests presented by Zhao and Hancock (1990) [155], it is stated that a clear peak load is normally found for the web buckling failure mode, and the chord flange failure usually displays a post-yield response due to the effect of membrane forces in the chord and material strain hardening. In this research, an attempt was made to isolate the effect of local loading (pure concentrated force) on the chord web within the general pattern of T-joint resistance. It was established that in the series of pure concentrated force tests, where test specimens were directly placed on a solid steel base plate of the testing machine, the failure modes vary from local bending of the chord member face as β-ratios vary from 0.5 to 1.0. The web crippling capacity of specimens operating under the combined action of compression and bending, with specimens fixed as simply supported end conditions, is reduced for $\beta = 1.0$. For $\beta = 0.5$, the effect of bending moment reduces the failure load, and the load-displacement curve becomes flatter after failure. Across all tests, the web crippling capacity is diminished by the effect of bending moment, resulting in longitudinal stress in the web of the RHS section. For tests with $\beta = 1.0$, increasing the slenderness of the chord member has a minimal impact on the degree of interaction. However, for tests with $\beta = 0.5$, higher section slenderness of the chord member leads to greater interaction between bending and concentrated force, especially for slenderer sections.

Similar failure modes in T-joints subjected to axial forces acting in the brace are observed in more recent experimental investigations of RHS T-joints conducted by Chen et al. (2015) [18], Feng & Young (2008b) [40] in tests of T-joint specimens made from cold-formed stainless steel, Kvocak et al. (2012) [58] on connections consisting of various profiles of brace members, Lip et al. (2006) [69] in tests of arc-welded T-joints between equal-width cold-formed RHS, and Nizer et al. (2016) [90].

The studies of T-joint behaviour carried out by Szlendak and Brodka (1985) [114] and Szlendak (1991) [115] were designed to investigate the in-plane bending resistance of beam-column RHS connections. The experimental component of the study consisted of 52 tests conducted on T-joints of square and rectangular hollow sections, subjected to in-plane bending moments. Generally, three failure phenomena of the joints were observed: the first being a joint failure,

involving the failure of the loaded flange and/or webs of the chord member; the second being a local failure of the member in the vicinity of the joint, which is not the joint itself but rather a member failure; and the third being a failure of the welds. As seen in other tests, a clear dependence of the failure mode on the β-ratio was established. For weaker joints ($\beta \ll 1$), the maximum load is associated with very large local deformations of the chord flange, while for stronger joints ($\beta \to 1$), cracks typically appear in the area influenced by weld heat before reaching the maximum load. In the case of stronger joints, failure processes are accompanied by chord local buckling under the adjusting brace wall.

Packer (1993) [96] examined the resistance of Vierendeel truss connections and classified the possible failure modes for RHS T-joints subjected to in-plane bending moments into five basic types: chord face yielding; cracking in the chord flange; cracking in the bracing member, both on the side of tensile fibre; crippling of the chord side wall; chord shear failure.

It was established that the failure modes assume that neither the welds nor the members themselves are critical (e.g., local buckling of the bracing is precluded). Interestingly, cracking in the chord (chord punching shear) was not observed over the entire range of applied loads in any of the tests.

For all the mentioned modes of failure, different strength criteria exist, but in some cases, it is possible to predict the joint strength using only one or two decisive criteria. According to the classification provided by Wardenier (1982) [141], the resistance or strength of the RHS T-joint can generally be characterized by diagrams schematically shown in Figure 2.1. Commonly adopted characteristic points on the typical load-displacement diagrams correspond to various failure criteria: ultimate load capacity (point 5), deformation criteria (points 2 or 3), and visually observed crack initiation (point 4 on the diagram).

However, the applicability of design formulas developed based on the enumerated failure criteria is generally limited in a way that deformation criteria alone do not become the determining factor under service load conditions. For joints with significant deflections, including T-joints with low values of β-ratios, the strength might be primarily based on the ultimate load capacity. However, in such cases, additional criteria must be provided to address deformation concerns. These types of joints are of secondary importance in practical applications, thus simplified theoretical strength criteria are often provided, which indirectly consider the deformation criteria.

Although every deformation limit is arbitrary, as it depends on the type of structure, a deformation of 1% of the chord width is generally accepted under service load conditions. This limit coincides with the maximum tolerance in width and depth of RHS sections. The ultimate load capacity is commonly used as the unambiguous criterion of failure, particularly for connections characterized by high values of β-ratios. Experimental evidence from studies by Zhao and Hancock (1990) [155] and Kato and Nishiyama (1980) [52] supports the realization of ultimate load capacity for T-joints with β-ratio values of 0.8 to 0.85.

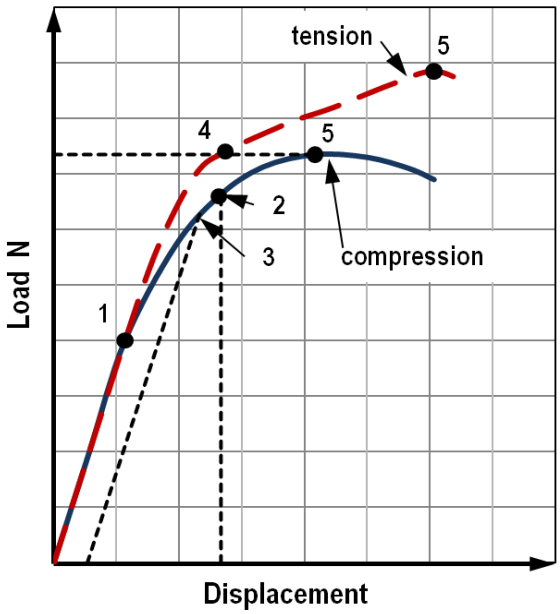

Figure 2.1 Load-displacement diagram of the RHS T-joint
1 – elastic limit; 2 – deformation limit; 3 – remaining deformation limit;
4 – crack initiation; 5 – ultimate load

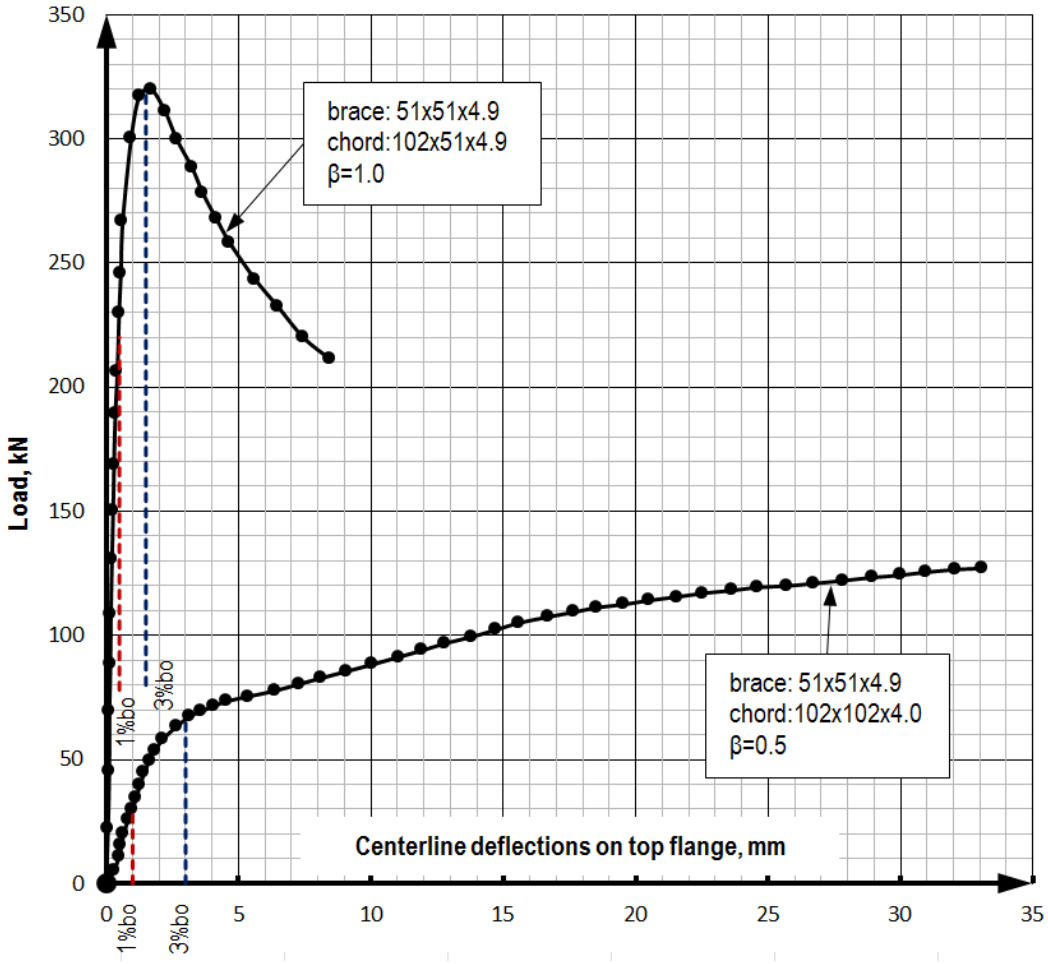

Figure 2.2 Experimental force-displacement curves for T-joint specimens subjected to pure axial force

Experimental force-displacement curves for T-joint specimens subjected to pure axial force (as described earlier) acting along a longitudinal axis of a brace member are presented in Figure 2.2. These diagrams clearly illustrate that the criteria for evaluating the limit state of T-joints are directly dependent on the width-to-width ratio β. Evidently, only the ultimate load criterion needs to be employed for assessing the bearing capacity of connections with a high β-ratio. On the other hand, the shape of the load-displacement diagram for T-joints with non-equal width components, where the β-ratio is near 0.5, suggests that additional conditions must be used for their limit state evaluation.

2.2.2 Deformation limits

A deformation limit serves to determine the strength of connections that lack a well-defined peak or yield load, which is common for flexible joints with low β-ratios. Consequently, the load corresponding to the deformation limit restricts the ultimate capacity of the connection. Since the mid-1970s, several ultimate and serviceability deformation limits have been proposed for RHS connections by various researchers. Mouty (1977) [88], who was developing a yield line method for RHS K-type gapped connections, found that the yield load predicted by his yield line analysis aligned with a connecting face deformation of 1% of the main chord width b_0. Based on 12 experimental tests, Mouty suggested that the deformation of the connecting face of the chord member should be limited to 1% at the ultimate design load.

Korol and Mirza (1982) [53] proposed that for RHS T-connections, the ultimate deformation of the connecting chord face should be limited to 25 times the deformation experienced at the connection's elastic limit. The deformation at this prescribed limit was generally around 1.2 times the chord thickness t_0 and often exceeded the limit set by Mouty (1977) [88], except for large width ratios ($\beta > 0.83$). The International Institute of Welding (IIW) Subcommission XV-E (1989) [33] adopted a serviceability deformation limit of $1\% b_0$. This serviceability deformation limit of 1% corresponds to the typical out-of-flatness or out-of-straightness tolerance for RHS wall faces imposed on HSS manufacturers.

The aforementioned deformation limits are specific to certain cases and apply only to either CHS or RHS connections (with the exception of the limit adopted by the International Institute of Welding (IIW) Subcommission XV-E (1989)) [33]. However, Lu et al. (1994) [76] proposed a single ultimate deformation limit that could be used for nearly any type of welded tubular connection (such as plate or I-beam-to-CHS connections, plate or I-beam-to-RHS connections, CHS X-connections, RHS X- and T-connections). This limit was based on both numerical and experimental results, and it was validated by Lu et al. (1994) [76] and Zhao (2000) [160] before being adopted by the International Institute of Welding (IIW) Subcommission XV-E. The ultimate deformation limit proposed by Lu et al. (1994) [76] has become widely accepted as the standard for limiting the ultimate strength of RHS connections among researchers. To fully understand the

implications of the $3\%b_0$. ultimate deformation limit for future research, it's important to delve into its origins and development.

The $3\%b_0$ ultimate deformation limit chosen by Lu et al. (1994) [76] and endorsed by the IIW was based on two fundamental premises. Firstly, this numerical parameter emerged from experimental and numerical tests conducted at Delft University of Technology by van der Vegte et al. (1991) [119], de Winkel et al. (1993), and Yu and Wardenier (1994) [77]. These studies revealed that for welded HSS connections (both RHS and CHS) that reached a peak load, the corresponding local deformation of the chord face ranged between $2.5\%b_0$ and $4\%b_0$, irrespective of the value of β. Drawing from these findings and their own tests, Lu et al. (1994) [76] proposed a local ultimate deformation limit of $3\%b_0$ for HSS connections that lack a clear peak load, approximating the deformation at ultimate load for connections that did exhibit a peak load. This assumption is further supported by the diagrams presented in Figure 2.2, where the total bearing capacity of a T-joint with $\beta = 1.0$ was attained at a deformation level of approximately $3\%b_0$. The second approach to establishing the $3\%b_0$ deformation limit involved numerous Finite Element simulations conducted in the late 1990s and early 2000s.

The established deformation limits corresponding to joint bearing capacity (ultimate strength) serve as the foundational points for the development of analytical models. The deformation limit for the web buckling failure mode of RHS T-joints is contingent upon geometry and, consequently, the joint's deformability. This relationship can be illustrated through the diagrams presented in Figure 2.3 and Figure 2.4.

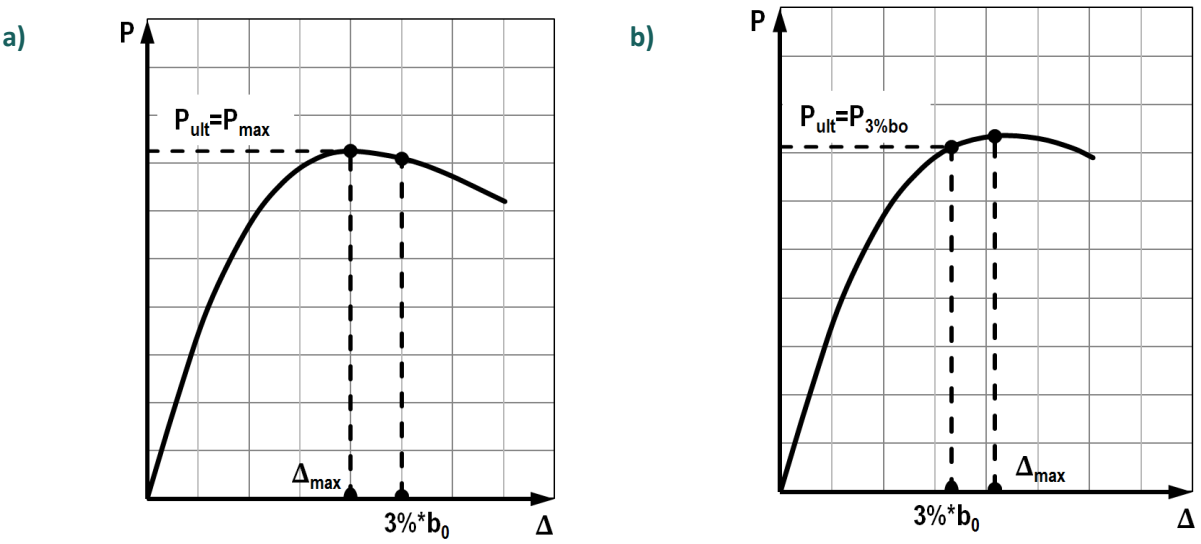

Figure 2.3 Force-displacements diagrams (web buckling failure): $\Delta_{max}<3\%b_0$ (a), $\Delta_{max}>3\%b_0$ (b)

The utilization of displacement limit values of $3\%b_0$ has been proposed to distinguish between T-joints with varying width-to-width ratios β and chord width-to-double-thickness ratios γ. Based on test results, the deformation limit is determined as $3\%b_0$ for $0.6 \leq \beta \leq 0.8$ or $2\gamma \leq 15$, and $1\%b_0$ for $0.3 \leq \beta \leq 0.6$ or $2\gamma > 15$. Consequently, the methods of determining the peak load P_{max} for the web buckling failure mode can be categorized into two types.

For joints where the peak load P_{max} occurs at a deformation smaller than $3\%b_0$, the peak load is considered the ultimate load P_{ult}, as depicted in Figure 2.3 *a*. Conversely, for joints with a peak load P_{max} at a deformation greater than $3\%b_0$, the load at the $3\%b_0$ deformation limit is regarded as the ultimate load P_{ult}, as shown in Figure 2.3 *b*. The conclusion drawn was that the $3\%b_0$ deformation limit proposed by Lu et al. (1994) [76] for ultimate strength is applicable to T-joints in cold-formed RHS sections with $0.8 \leq \beta \leq 1.0$.

Deformation limits for cases of chord flange failure mode were derived from the assumption that the deformation limit hinges on the ratio of ultimate load $P_{3\%b_0}$ to serviceability load $P_{1\%b_0}$. If this ratio is below 1.5, the ultimate deformation limit is $3\%b_0$, indicating strength control. In this scenario, the ultimate strength is considered as $P_{3\%b_0}$, as illustrated in Figure 2.4 *a*. On the other hand, if the ratio exceeds 1.5, the serviceability deformation limit of $1\%b_0$ is in effect. Here, the ultimate strength is taken as 1.5 times $P_{1\%b_0}$, as demonstrated in Figure 2.4 *b*.

a)

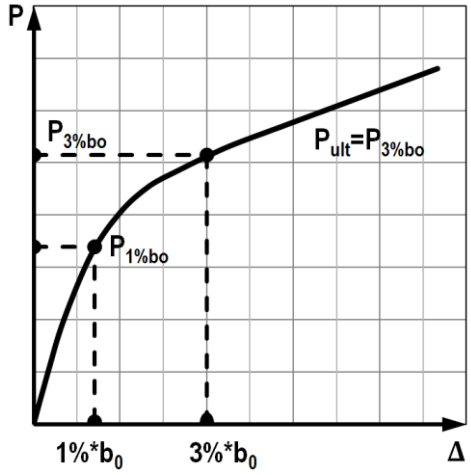

b)

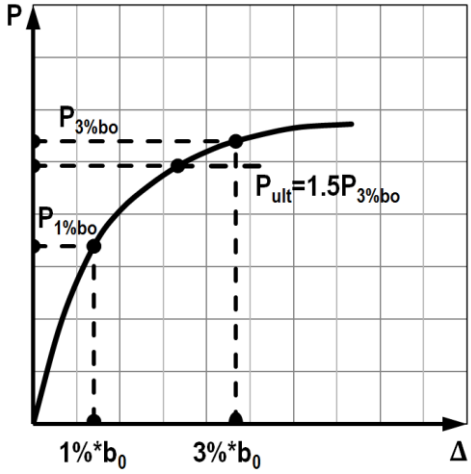

Figure 2.4 Force-displacements diagrams (chord flange failure): $P_{3\%\,b0} / P_{1\%b0} < 1.5$ (a), $P_{3\%\,b0} / P_{1\%b0} > 1.5$ (b)

The aforementioned failure modes and deformation limit designations are considered fundamental for the development of analytical models and the derivation of design formulas. However, the criteria for deformation limits in serviceability and ultimate capacity of welded RHS connections, which do not exhibit a clearly defined ultimate or yield load, have raised some complexities. Although these deformation limits have gained wide acceptance among researchers and have been adopted by the IIW Subcommission XV-E, various methods have been proposed to determine the "yield load" and "ultimate load" from load-displacement curves of connections that lack a distinct yield or ultimate point. The yield or ultimate loads obtained through these pseudo or approximate methods can be used to define the limit state of a connection, similar to how the definitive yield or ultimate load would be utilized.

Given the lack of consensus among researchers and the specificity of each pseudo yield or ultimate load determination method to certain types of analysis or research, many methods are not applicable in current research. One classic approximate yield load determination method, which has been employed since the 1970s (Packer (1978), Packer et al. (1980) [95], Zhao and

Hancock (1991) [157]), is illustrated in Figure 2.5 for RHS connections experiencing chord face plasticization. This method, often referred to as the double-tangent method or bi-linear method, involves approximating the load-deformation curve obtained from tests with two straight lines. The first line starts from the origin and follows the linear elastic portion of the load-deformation curve, while the second line follows the second linear portion or stiffness of the load-deformation curve. The yield load $N_{\mathrm{l,bi-linear}}$ is identified as the load at which these two lines intersect, indicating a significant change in stiffness. Packer et al. (1980) [95] resorted to the classical bi-linear method of determining the yield load, with deformation expressed as a normalized quantity, due to the absence of a consensus on the definition of the yield load from experimental load-deformation curves during that time.

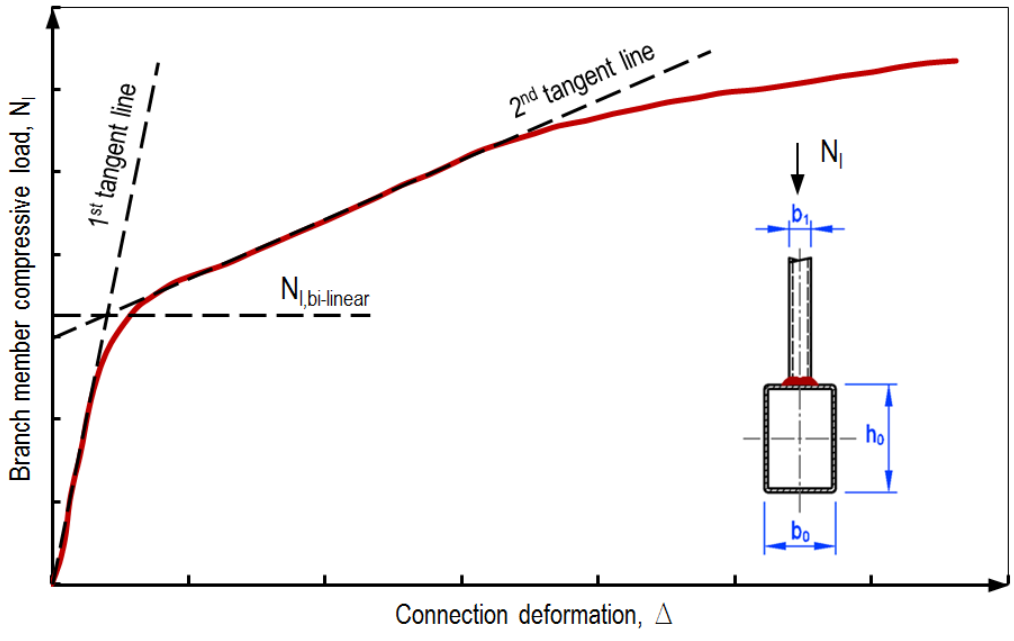

Figure 2.5 Bi-linear (double-tangent) method for yield load determination

The method presented for determining the pseudo yield or ultimate load from a load-deformation curve offers distinct advantages over a strict designation of the deformation limit. However, it relies on very specific circumstances and parameters of the load displacement diagram used as a basis. Furthermore, like the $3\%b_0$ ultimate deformation limit proposed by Lu et al. (1994) [77], certain methods possess an arbitrary nature, which can potentially undermine their credibility. For instance, as highlighted by Kosteski (2001) [54], setting point B of the tri-linear curve as one third of the initial stiffness as proposed by Kamba and Taclendo (1998) [51], and the 0.25 scatter band suggested by Kurobane et al. (1984) [60], are notably arbitrary and reliant on specific data. In contrast, the $3\%b_0$ ultimate deformation limit has garnered acceptance among numerous researchers and has been corroborated by multiple studies utilizing modified finite element modeling techniques.

In the past, some published experimental results have addressed the influence of chord stresses on brace load-bearing capacity. These findings revealed that compressive chord stresses significantly diminish joint resistance. However, few studies have indicated a comparable reduction in load-carrying capacity for joints subjected to tensile chord forces. This discrepancy is reflected in design codes such as EN 1993-1-8 and ABNT NBR 16239. Notably, it is important to note that the second edition of the CIDECT design guide for RHS joints (2004) [64] and ISO 14346 permit a reduction in joint resistance for both cases – tensile and compressive chord stresses. Additionally, Lipp and Ummenhofer (2007) [118], drawing from experimental and numerical results, proposed a reduction in the design capacity of CHS joints to account for the presence of tensile chord loads.

2.2.3 Fatigue of T-joints

Lattice structures, typically comprised of numerous welded connections, are commonly subjected to combined forces and moments acting in various directions. As a result, the robustness of lattice structures is predominantly determined by the strength and deformations of their welded joints and connections. Welded joints are particularly susceptible to fatigue crack initiation and propagation due to imperfections and defects that serve as stress concentrators, initiating fatigue cracks in the vicinity of weld seams. Furthermore, regions of non-uniform stress transfer along the perimeter of brace member surfaces, immediately adjacent to the chord face, can be observed. The non-uniform distribution of stresses near the weld is contingent upon the connection configuration (joint type) and its geometric parameters. Fatigue failure is a localized phenomenon, emphasizing the need to consider structural robustness on both global and local levels of analysis.

At the global level, the overall structural integrity is assessed, considering a comprehensive array of forces and actions. Meanwhile, the local level analysis scrutinizes connections between structural members in detail, accounting for local force effects and the influence of geometric shapes on connection resistance. This approach often necessitates evaluating the robustness of individual structural components, as their failure could result in the collapse of the entire structure. In such local analyses, it is pertinent to examine the sections of the structure or structural members located in zones vulnerable to fatigue damage, marked by the presence of stress concentrators.

This conceptual framework underlies a multitude of studies dedicated to the fatigue resistance of HSS joints. Researchers such as Van Wingerde et al. (1997) [122], Mashiri et al. (2004) [79], Bian et al. (2003) [9], Schumacher and Nussbaumer (2006) [106], Ahmadi et al. (2012) [4], Cheng et al. (2015) [21], among others, have identified regions termed "hot spot locations." These locations exhibit a significant spike in stresses near welds. In practical design, stress concentration factors (SCFs) are employed to quantify stress concentration. The SCF denotes the

ratio of the geometric stress at the weld toe to the nominal direct stress in the brace. The geometric stress at the weld toe is calculated by extrapolating stresses outside the notch region to the weld toe. The notch region, closely situated to the brace/chord intersection, governs stresses influenced by weld geometry factors. Geometric stresses, outside the notch region and known as the geometric stresses, are introduced to ensure compatibility between tubes undergoing wall bending. These stresses depend mainly on joint geometric parameters, overall joint configuration, and applied loading types. The "hot-spot stress" (HSS), as defined in the UK Department of Energy (UK DoE) Guidance Notes, represents the highest stress value around the brace/chord intersection, obtained by linearly extrapolating the geometric stress distribution to the weld toe. Consequently, HSS occurs at the peak SCF position. The SCF exhibits considerable variability contingent upon joint geometry, loading type, weld size and type, and the specific location around the weld under consideration.

Typically, contemporary investigations into stress concentration factor (SCF) and hot-spot stress (HSS) calculation methods employ Finite Element Method (FEM) approaches. FEM techniques have become available and highly effective over the past two decades. Experimental studies pertaining to the fatigue resistance of Rectangular Hollow Section (RHS) joints are both resource-intensive and technically intricate due to the requirement for precise stress distribution determination within the connection. Notably, pioneering efforts in the domain of fatigue assessment of HSS connections can be attributed to van Wingerde et al (1992) [121].

Van Wingerde's research program encompassed both experimental and numerical inquiries aimed at formulating design recommendations for predicting fatigue resistance in T- and X-joints subjected to axial forces or in-plane bending moments on the chord and brace. The scope of study involved a broad range of applicability. The foundation of these design recommendations rested upon the hot spot stress method, intended to incorporate the overall joint geometry's impact on stress distribution. This approach involved determining geometrical hot spot stress along specific established lines, using extrapolation to mitigate the localized influence of the weld. Experimental trials were conducted to ascertain the fatigue life of specific joint geometries, serving as calibration for the stress and strain concentration factors (SCF and SNCF) determined through Finite Element analyses.

In total, 28 specimens of hot-finished RHS with steel grades Fe430D and Fe430B were subjected to cyclic loading, with four of these specimens tested under bending moment conditions. The outcomes of these experimental studies were presented in the form of $S_{\mathrm{rh.s}} - N_F$ lines (based solely on experiments), along with an extensive database for parametric studies and validation of FE models. Additionally, the impact of stress level and thickness ratio $\tau = t_1/t_0$ on SCF and SNCF was identified and assessed. Specifically, T-joints with $\tau = 0.4$ exhibited failure in the brace, while those with $\tau = 0.64$ experienced fatigue failure in the chord. The comprehensive results of these T- and X-joints fatigue life studies are depicted in Figure 2.6.

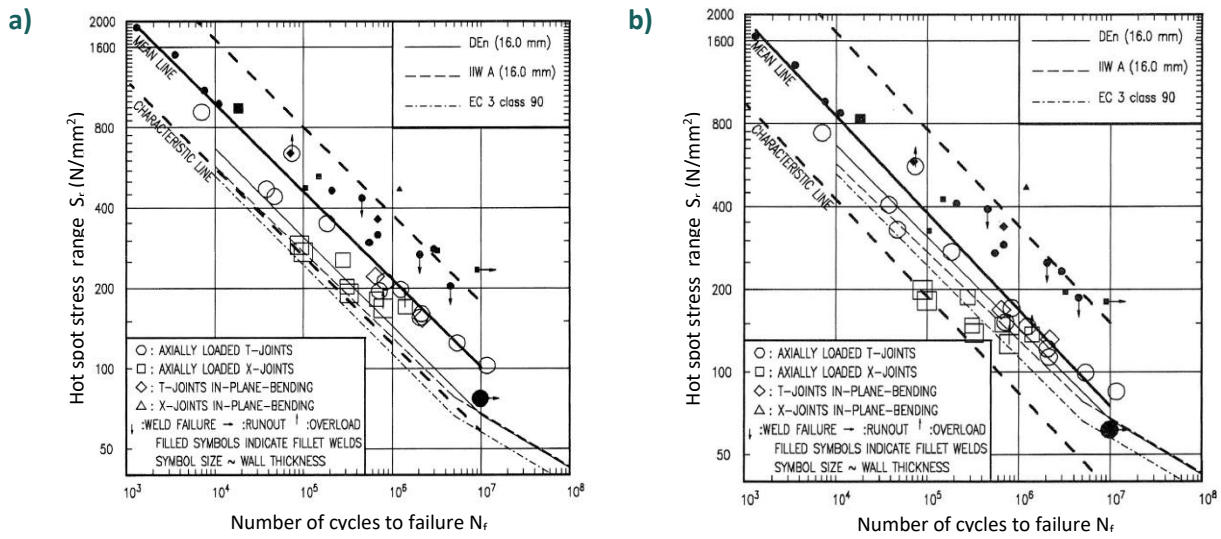

Figure 2.6 $S_{rh.s}$ – N_f lines, based on tests, without thickness correction, quadratic (a) and linear (b) extrapolation

Later, the fatigue behaviour of RHS joints of K- and KK-types was examined as an extension of T-joints fatigue studies by van Wingerde et al. (1997) [122]. The primary findings of these investigations, which incorporated both experimental trials and numerical analysis, were encapsulated in a series of equations. These equations establish the correlation between the geometry of a connection and the stress concentration factors (SCFs) within the connection. The resulting parametric SCF equations, along with $S_{\mathrm{rh.s}} - N_F$ lines and thickness correction factors, provide a comprehensive method for the fatigue design of welded K-connections between square hollow sections. This method covers both gap and overlap connection scenarios.

Mashiri et al. (2004) [79] conducted fatigue tests on welded thin-walled T-joints with CHS braces welded onto SHS chords. The loading conditions involved "in-plane bending in the brace." Stress distributions were measured at different hot spot locations around the chord-brace junction, where fatigue cracks were observed to initiate and propagate, leading to failure. The level of non-linearity in measured stress distributions around the weld toes of the brace-chord junction demonstrated significant non-linearity, particularly along specified locations for brace diameter to chord width ratios exceeding 0.5.

Based on stress measurements, a quadratic method of extrapolating local strains/stresses to determine hot spot stresses and identifying the hot spot location lines producing the highest hot spot stresses was adopted and recommended for further guidance. An approach for estimating SCFs in welded thin-walled CHS-SHS T-joints was also suggested, utilizing existing parametric equations for SHS-SHS T-joints. The maximum SCFs at weld toes in the chord of welded thin-walled CHS-SHS T-joints were approximately 0.38 times the maximum parametric equation SCF at the weld toes in the chord of an SHS-SHS T-joint. Stress distribution analysis at weld toes in the chord revealed that the degree of non-linearity of stress distribution increased as the brace diameter to chord width ratio β exceeded 0.5 for specific hot spot location lines (45° and 60°).

This non-linearity was significantly pronounced for β values exceeding 0.5. However, no notable effect of β on the degree of non-linearity of stress distribution was observed along the hot spot location line at 0°.

Bian and Lim (2003) [9] conducted experimental investigations into the static and fatigue behaviour of eight distinct hollow section T-joints exposed to axial and in-plane bending loads. These joints featured circular brace members and rectangular chords. Through experimental determination, hot spot stresses and stress concentration factors (SCFs) were identified. The test results underwent statistical evaluation, indicating that the experimental SCF values for CHS-to-RHS hollow section joints fell between those of CHS-to-CHS and RHS-to-RHS hollow section joints, aligning with findings by Mashiri et al. (2004) [79]. The fatigue strength, referenced to experimental hot spot stress, demonstrated reasonable alignment with relevant fatigue design codes for tubular joints. Additionally, a thickness effect was identified and assessed; new formulae accounting for the thickness effect were formulated and compared with analogous methods.

Several studies have investigated the fatigue resistance of K-joints made from CHS. Works by Gho et al. (2006) [31], N'diaye et al. (2009) [91], and Schumacher and Nussbaumer (2006) [106] stand out as notable examples of fatigue life investigations. The outcomes of these research endeavours typically manifest in experimental S-N curves for specific types of HSS joints, along with approximations for numerical SCF determination and recommendations for interpolating hot spot stresses.

A research group led by Ahmadi from Iran undertook an integrated series of investigations into the fatigue behaviour of multiplanar internal stiffened CHS joints, with a focus on offshore support structures. In their papers Ahmadi et al. (2014), (2016) [4] [5], they presented the outcomes of experimental and numerical studies concerning stress concentration in internally ring-stiffened tubular KT-joints. The research program involved experimental testing followed by parametric stress analyses of 118 steel ring-stiffened tubular KT-joints under balanced axial loading. The analysis results provided insights into the impact of geometrical parameters including τ (brace-to-chord thickness ratio), γ (chord wall slenderness ratio), η (ring-to-chord width ratio), β (brace-to-chord diameter ratio), and θ (outer brace inclination angle) on SCFs at specific positions (toe, saddle, and heel) along the weld toe of the intersection between the outer (inclined) brace and the chord.

Since the applied loads on inclined braces of a KT-joint are generally larger than those on the central (vertical) brace, hot-spot stresses tend to be higher along the intersections of outer braces with the chord. Therefore, the study primarily focused on the outer (inclined) braces. Drawing from the results of finite element (FE) models of ring-stiffened KT-joints, which were validated against experimental measurements, a comprehensive SCF database was compiled. This led to the establishment of a new set of SCF parametric equations, determined through nonlinear regression analysis, tailored for the fatigue design of internally ring-stiffened KT-joints.

These equations were evaluated using acceptance criteria recommended by the UK Department of Energy (DoE).

Key practical conclusions drawn from the research are as follows:

The SCFs on compressive braces are consistently greater than their counterparts on tensile braces.

In unstiffened KT-joints subjected to balanced axial loads, the peak chord-side SCF along the weld toe of the intersection between the outer brace and the chord typically occurs at the saddle position. In internally ring-stiffened KT-joints, the peak chord-side SCF is located at the toe and saddle positions for compressive and tensile braces, respectively. This suggests that the position from which fatigue cracks initiate can differ in stiffened and unstiffened KT-joints under axial loading.

SCFs in unstiffened KT-joints are generally much larger than those at the same positions in corresponding ring-stiffened joints. This observation indicates that using SCF design equations developed for unstiffened KT-joints often leads to overestimating and overly conservative SCFs for stiffened joints. Thus, specialized SCF formulae tailored for ring-stiffened tubular KT-joints are necessary.

The minimum chord-side SCF always resides at the heel position on both compressive and tensile braces.

Increasing parameters θ, γ, and τ leads to higher SCFs on both compressive and tensile braces at all three positions (toe, saddle, and heel).

The parameter η's increase results in decreased SCFs on both compressive and tensile braces at all three positions.

The parameter β generally increases SCFs on the tensile brace across all three positions. On the compressive brace, the SCFs at the toe and heel positions rise with an increase in β, while the maximum SCF at the saddle position depends on other dimensionless parameters and is usually observed in joints with an intermediate β value ($\beta = 0.5$).

The impact of changing τ on SCF values is more significant than the effects of β and γ; β's effect on SCFs is less pronounced than that of γ.

Additionally, Mashiri and Zhao (2004) [78] conducted static loading tests on strain-gauged SHS-SHS T-joints with concrete-filled chords to determine stress concentration factors (SCFs) at hot spot locations. They found that composite tubular T-joints demonstrated superior fatigue strength compared to empty hollow section SHS-SHS T-joints.

In the last decade, numerous experimental studies have explored the resistance of traditional and bird beak SHS T-joints. Bird beak joints involve a chord rotated by 45° about its longitudinal axis, resulting in common bird beak joints (chord rotated by 45°) and diamond bird beak joints (both chord and brace rotated by 45°). Research by Tong et al. (2014) [116] and Cheng et al [21]

included static and fatigue tests on bird beak T-joints. Their investigations encompassed failure modes, compression capacity assessment, and the analysis of cyclic loading patterns and SCF distribution. They concluded that the maximum SCF in the brace is consistently larger than in the chord for in-plane bending, but this scenario is reversed under axial force. The axial force-induced SCF is notably higher than that under in-plane bending, generally exceeding 2 and being less than 2, respectively. Moreover, for identical key parameters (β, 2γ, and τ), the SCF for diamond bird beak T-joints is notably lower than that for SHS-to-SHS and CHS-to-SHS T-joints. It approaches, and slightly surpasses, the SCF of CHS-to-CHS T-joints, consistent with the observed increased fatigue life in such joints compared to conventional T-joints.

2.2.4 Fire resistance of T-joints

Numerous researchers have conducted steady-state and transient analyses on the fire resistance of HSS (hollow structural section) joints. Some of these studies include:

- Nguyen et al. (2010) [92] investigated the structural behaviours of CHS T-joints and performed a parametric study on the ultimate strength of CHS T-joints subjected to brace axial compression under fire conditions.
- Feng and Young (2010) [41] studied the design of cold-formed stainless steel tubular joints at elevated temperatures.
- Liu et al. (2009) [72] analysed the load capacity and deformation of T-joints with stiffened rings at elevated temperatures, along with the mechanical performance of tubular T-joints used in offshore platforms under fire exposure.
- Xu et al. (2012) [151] explored the ultimate bearing capacity of tubular T-joints under fire conditions using artificial neural networks.

Transient analysis on the fire resistance of tubular joints has also been conducted:

- Liu et al. (2010) [73] examined the mechanical behaviour of steel planar trusses in fire through experimental testing.
- Jin et al. (2010, 2012) [47], building on Liu's work, carried out parametric analysis of the mechanical behaviour of steel planar tubular trusses under fire conditions. They studied the influence of geometrical parameters on the fire resistance of tubular trusses and investigated the residual bearing capacity of CHS T-joints after exposure to fire.
- Shao et al (2016) [103] investigated the effect of loading ratio on the critical temperature of tubular truss joints.

Based on these studies, several conclusions have been drawn:

- For CHS T-joints under compression at the brace end and localized heating, the general failure mode is plastic failure of the chord face around the brace/chord intersection. The failure process involves three stages: initial displacement decrease due to steel expansion,

subsequent displacement increase due to steel degradation at elevated temperatures, and abrupt displacement increase when temperatures reach a certain high level.

- The fire resistance of CHS T-joints is significantly affected by loading ratio n and diameter ratio β. Diameter/thickness ratio γ and length/diameter ratio α have relatively weaker influences. Increasing β and γ generally improves fire-resistant performance, while increasing n and α reduces performance. Pre-load on the brace also influences residual deformation after fire exposure.
- Residual strength after cooling slightly decreases with increased pre-load ratio under fire conditions. The effect of pre-load on braces and the cooling phase has minimal impact on the residual load-bearing capacity of T-joints.
- Increasing the brace diameter β and wall thickness of the chord γ can significantly improve the residual strength of the T-joint after fire exposure.

However, it's important to note that the studies mentioned above were primarily focused on CHS connections, and the results cannot be directly transferred to joints made from RHS (rectangular hollow section) profiles without proper validation. The specific fire behaviour of RHS joints requires separate investigation and detailed study to ensure accurate fire resistance assessment.

2.2.5 Accounting for size effect in design of RHS T-type connections

Mashiri et al (2007) [70] investigated the Size effect of welded thin-walled tubular joints. They summarized existing research within the context of newly defined terminologies and identified knowledge gaps related to designing tubular joints using the hot spot stress method. The study specifically focused on thin-walled tubular joints with wall thicknesses under 4 mm, excluding thick-walled joints with wall thicknesses exceeding 50 mm or diameter-to-thickness ratios below 24. Notably, the investigation centred on thin-walled tube-plate T-joints. Contrary to conventional expectations, the paper revealed that fatigue life trends for thin-walled sections did not conform to the anticipated pattern of improved fatigue life with reduced thickness. Moreover, the study highlighted the potential hazards of directly extrapolating existing fatigue design curves to thin-walled tube-tube T-joints, as it could lead to unsafe designs. The study also addressed the influence of chord stiffness on the fatigue behaviour of thin-walled tubular T-joints, providing significant insights into this critical aspect of joint behaviour.

2.2.6 Research of RHS T-type connections with offset

It is worth noting that prevailing design methods for HSS connections were tailored exclusively for coaxial configurations, implying that the centrelines of branch members should intersect with the chord centreline – an arrangement termed as 'Standard'. However, the mechanical behaviour

of offset joints, where branch members deviate from the chord centreline, has received limited attention in design guidelines.

The initial exploration into the behaviour of laterally offset T- and N-connections was undertaken by Dawe et al. (2006) [25], marking a pioneering contribution to the existing literature on this subject. Their experimental study involved 16 full-scale tests on cold-formed welded RHS connections, including ten T-connections and six N-connections. Among the T-connections, 10 specimens were tested to failure with axial compression on the branch members, while seven of these were full-width T-connections with a branch size of HSS 152x152x6.4. The remaining three specimens featured smaller branch members (HSS 102x102x6.4) fully offset towards the chord sidewall. Strikingly, when comparing the compressive strength of full-width T-connections to laterally offset connections with width-to-width ratio $\beta = 0.67$ under the same nominal chord loads, a mere 5% reduction was observed in the strength of the latter. This unexpected finding raised questions about the accuracy of the experimental program, despite its valuable insights into the challenges of shifted brace connections.

Notably, works by Kalmykova and Wald [49], [50] delved into laboratory and numerical exploration, and Wei and Packer [146] conducted testing on offset SHS T- and X-joints while proposing design approaches and analytical equations for predicting their resistance. Subsequently, a notable effort was made by Bu, Wei, and Packer (2021) [11] to address the design complexities posed by offset connections. Their comprehensive research spanned laboratory tests, numerical simulations, and theoretical analyses on offset T-type and X-type connections. Their aim was to formulate an analytical model for estimating the limit resistance of fully offset connections. The experimental phase of the study involved testing a significant number of X-type and T-type specimens to failure, while focusing on width-to-width ratios. Nevertheless, there are concerns about the adequacy of the premises underpinning these proposed equations, particularly regarding the absence of web resistance components in the virtual works equation and the verification principles of the resistance formula put forth in [11].

2.3 NUMERICAL RESEARCHES

Four decades ago, Finite Element Analysis (FEA) of structural connections was often regarded by researchers as an unconventional approach due to its novelty, mathematical limitations, and the substantial computational costs of that era. However, over the following two decades, it evolved into an accepted and even essential addition to experimental and theoretical investigations. Presently, computational analysis, particularly in the realm of computational mechanics, is widely used as an indispensable design tool and a driving force behind numerous research domains. In scenarios where experimental testing is constrained by the load-carrying capacity of laboratory equipment, FEM simulations have become an irreplaceable alternative. In fact, the

recommendations for advanced modelling in structural steel design are already discreetly integrated within Chapter 5 and Annex C of EN 1993-1-5:2005.

The majority of recent research on Circular Hollow Sections (CHS) and Rectangular Hollow Sections (RHS) joints has been conducted through numerical analyses utilizing the FEM approach, overshadowing traditional experimental studies. Typically, test results directly validate numerical FEM models developed to simulate the structural behaviour of these joints.

Efficient modelling using finite element techniques requires the creation of models that are both accurate and simple enough to avoid excessive consumption of computational resources during parametric studies. A valid model is often achieved through previous experiential knowledge, incorporating factors like the selection of elements, analysis types, options, and mesh densities. Additionally, calibration of the model against experimental data is highly recommended. To this end, moment-rotation or force-displacement curves are commonly employed for comparing test results with numerically derived data.

The earliest comprehensive application of the finite element method (FEM) to the study of RHS connections is attributed to Korol and Mirza (1982) [53]. They ventured beyond the elastic limit to model the behaviour of Rectangular Hollow Section (RHS) T-joints, determining their ultimate and working strengths. Their study included calculations of punching shear and rotational stiffnesses under branch axial force and bending moment. Both unreinforced and haunch type joints were analysed, with the top flange of the chord represented as a thin plate supported by coupled edge springs. Incorporating line loads along the perimeter of a rigid inclusion (the branch) simulated loading. In the elastic range, joint stiffness values closely correlated with available test results. Exploring geometric parameters such as width ratio λ, haunch size λ_1, and chord thickness t in the elastic-plastic range revealed ultimate branch moments or punching shear forces approximately five times their corresponding first yield values, suggesting the importance of basing design loads on ultimate strength or maximum deflection criteria.

Crocket's thesis work (1994) expanded upon this by conducting nonlinear geometric and material FE analyses of diverse tubular joint scenarios involving both CHS and RHS. An essential aspect of the work was assessing the influence of finite element density and the modelling of welds and corner radii on analysis outcomes. The study demonstrated that including welds is crucial for achieving realistic results in FE analyses of the ultimate static strength of tubular joints. A full corner weld model employing solid tetrahedral finite elements yielded the most accurate simulation results, aligning closely with the weld profile of known test specimens. A mesh convergence study demonstrated the adequacy of a "medium" mesh, suitable when the member's size ranged from $0.2b_0$ to $0.3b_0$, for predicting joint capacity.

Moreover, numerical simulations revealed that adding Directly Transferred (DT) braces to a planar T-joint significantly enhanced its capacity, particularly at $\beta = 1.0$. However, at $\beta = 0.25$, no such increase was observed. The presence of loads with the same sense in the Directly Transferred (DT) braces as those in the T-brace has minimal impact on capacity across all β ratios.

However, when the loads are in opposite senses in the DT braces (i.e., tension in one plane and compression in the other), capacity reductions below that of corresponding planar joints can arise in specific scenarios. The extent of these effects hinges on the β ratio. For cases where $\beta = 1.0$, the reductions are negligible. However, when $\beta = 0.6$ or 0.25, the capacity can drop below that of planar joints. Consequently, when designing based on a plane-by-plane analysis, the design of such joints may become overly optimistic, warranting a need to address this aspect in the design codes.

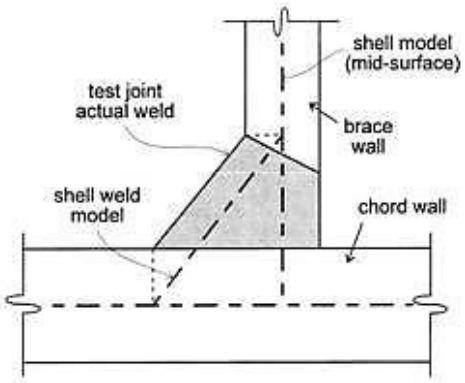

Figure 2.7 Weld modelling with shell elements

Prominent instances of Finite Element Analysis (FEA) application in modern research concerning RHS T-joints are exemplified by the work carried out by Matos et al. (2015a, 2015b) [82] [83]. These studies involved the development of a numerical model for RHS T-joints that considered material and geometric nonlinearities, employing the ANSYS software. The FEA utilized four-node shell elements (SHELL181) with six degrees of freedom per node, capturing bending, shear, and membrane deformations. Similar to earlier studies by researchers like Korol and Mirza (1982) [53], Lu et al. (1993, 1994), Lee (1999) [64], Kosteski et al. (2001) [55], Costa-Neves (2004) [89], Lima et al. (2007) [68], and Van der Vegte et al. (2010) [127], major finite element analysis options were applied. This encompassed the use of shell elements over solids, modelling welds and section corners, and adopting analysis types and options outlined in the work.

A well-proportioned mesh was applied to the model, maintaining element quality and avoiding numerical issues. For stress concentration areas and geometrical singularities, mesh refinement was employed. Welds were also represented using shell elements, as suggested by Lee (1999b) [65] and later adopted by Lima et al. (2007) [68], offering accurate results. In this approach, inclined shell elements possessed weld material properties, while their projection retained the unchanged properties of connected members. This methodology was initially validated in a previous study by the authors (Lima et al., 2007) [68] using experimental data from Lie et al. (2005) [67]. Calibration results exhibited an excellent fit between the experimental force-displacement diagram and the simulated outcome.

The numerical model was employed by Matos et al. (2015a, 2015b) [82] [83] to explore the behaviour of the chord face under varying dimensions of the loaded area and thickness of the loaded chord face, denoted by variables β and γ (1st set of analysis). Additionally, the influence of forces acting in the chord (varying tension and compression levels) on the connections' general resistance and stiffness was studied (2nd set of analysis). The first set involved 42 simulations with β ranging from 0.40 to 0.98 and γ varying from 9.38 to 25. Force-displacement curves from all simulations were presented, illustrating variations in initial stiffness and resistance with relevant variables. Resistance numerical results, derived from the $3\%b_0$ deformation limit criterion, were compared with EC3 (2005) outcomes. For β values up to 0.66, both methodologies yielded similar results. However, as β increased, EC3 (2005) started overestimating resistance, with this trend continuing up to $\beta \leq 0.80$ and a thickness not exceeding 12 mm. For larger chord thicknesses ($\gamma \leq 12.5$) and any thickness with $\beta > 0.80$, differences emerged. In the second set, comprising 168 simulations, it was deduced that axial force in the chord generally reduced joint resistance, with this effect magnifying for greater axial loads. Joint geometry was a determining factor, as larger β values seemed more affected than those with smaller values of this parameter. The mentioned numerical simulations underscore the efficacy of the FEA-based approach in structural connection research.

It's also noteworthy to mention that numerous recent numerical analyses, especially within the last decade, have employed more complex FE models that include volumetric finite elements. Utilizing brick elements with 16 or 20 nodes enhances accuracy but comes with increased computational complexity and CPU costs. Cheng et al. (2015) [21] undertook an investigation using the ANSYS12 program, focusing on strain/stress concentration factors (SNCFs/SCFs) for two types of SHS T-joints. The analyses were conducted under small deformation and material elasticity assumptions, utilizing solid elements (SOLID95) with 20 nodes and three degrees of freedom per node. Accurate geometries of fillet welds were incorporated into the FE models, with mesh refinement in stress concentration zones. Parameters controlling mesh sizes were validated against half-size refined meshes, and errors in SNCF ranged from 0.1% to 4%, indicating the adequacy of the established FE meshes.

Feng et al. [41] used the ABAQUS software for a nonlinear numerical study of CHS brace-to-H-shaped chord X-joints under in-plane bending. The finite element model integrated measured cross-section dimensions and material properties from tests. A three-dimensional eight-node solid element (C3D8I) with incompatible modes was employed to model the CHS brace and H-shaped chord members. The use of this element helped mitigate locking issues and improve accuracy. Geometric and material nonlinearities were both considered, with a focus on the in-plane flexural behaviour of the joints. The material model was based on elastic and post-yield tangential moduli from tensile coupon tests, and the Von-Mises yield criterion was used.

Among the global structural models in the literature, the works of Wardenier, van der Vegte, and Liu (2007a, 2007b) [142] [143] are significant. They derived new chord stress functions for RHS

K gap joints through comprehensive parametric analyses. In the CIDECT program 5BK, the influence of chord stress on the axial strength of CHS T, X, and K gap joints was re-evaluated. Various combinations, spanning different β and 2γ values, were numerically analyzed for different chord stress ratios. The accuracy of the proposed chord stress functions was assessed against experimental results and FE data, with thick shell elements (MARC element type 22) used to model the joints and welds. Geometric and material nonlinearity were considered, and corner radii were modelled. The FE model was calibrated using numerical and experimental load-deflection curves. The study resulted in new chord stress functions for RHS K gap joints, consistent with those for other types of joints. However, it was concluded that finding a single uniform function fitting all types of joints was not feasible based on the comparative results.

These instances highlight the evolving complexity and capabilities of numerical analysis in studying various types of joints, contributing valuable insights to structural connection research.

In their study on the fatigue resistance of multiplanar CHS joints, Ahmadi et al. (2016) [5] highlighted the critical importance of accurately modelling weld profiles to ensure accurate Stress Concentration Factor (SCF) results. Neglecting weld sizes can lead to substantial inaccuracies. The authors referred to previous research by Lee and Wilmshurst (1995) [62] and Lee (1999) [65] which explored the impact of welds. Notably, omitting the weld could result in a 20% underestimation of joint fatigue strength compared to experimental data. To address this, ANSYS element type SOLID95 was utilized to model the chord, braces, and weld profiles. These elements are compatible with curved boundaries and allow for precise representation of weld profiles. Defined by 20 nodes with three degrees of freedom per node, these 3-D brick elements can simulate the weld profile as a sharp notch. This approach was expected to yield more detailed and accurate stress distribution near intersections compared to simple shell analysis.

To ensure mesh quality, the authors employed a sub-zone mesh generation method during FE modelling. This technique involves dividing the structure into distinct zones based on computational needs, generating meshes for each zone separately, and then merging these meshes to form the entire structure. This method facilitates control over mesh quality and quantity and helps prevent distorted elements. Ahmadi et al. noted the importance of conducting convergence tests with various mesh densities before creating FE models for parametric studies.

Using the FEM models described above, Ahmadi et al. (2016) [5] conducted numerical investigations into SCFs in two- and three-planar CHS KT-joints subjected to in-plane (IPB) and out-of-plane (OPB) bending moments. They presented general observations about the impact of geometric parameters, including τ (brace-to-chord thickness ratio), γ (chord wall slenderness ratio), β (brace-to-chord diameter ratio), and θ (outer brace inclination angle), on SCFs at different joint positions. The study aimed to analyse the multi-planarity effect under various OPB and IPB loadings, comparing SCFs from multi-planar and uniplanar joints to identify critical scenarios with significantly higher multi-planar SCFs. In such cases, new SCF parametric equations for fatigue analysis and design were developed using nonlinear regression analyses. Based on the

performed numerical and nonlinear parametric studies, the authors proposed a system of safety factors for multiplanar CHS joints and established SCF distribution patterns in the connections. They also concluded that increasing parameters τ, γ, β, and θ led to increased SCFs at the saddle position. The effects of τ and γ changes were more pronounced than those of β and θ changes, and parameter θ exhibited a more significant effect than β.

In the study conducted by Matos et al. (2015b) [83] , the influence of axial force on the chord's initial stiffness in joint connections was numerically investigated using the FEA model previously described. The findings indicated that when a compressive axial force is applied to the chord, it has an adverse impact on the stiffness of the chord face regardless of the level of axial load. Moreover, this adverse effect becomes more pronounced as the level of compression increases. On the other hand, when tension axial forces are applied to the chord, the stiffness of the joint increases up to a certain threshold of tensile load. After reaching this point, the stiffness either stabilizes or begins to decrease.

Garifullin et al. (2017) [30] attempted to evaluate the initial in-plane rotational stiffness of welded RHS T-joints with axial loads in the chord member. The objectives of this study were twofold: firstly, to assess the existing calculation approach for the initial rotational stiffness of such joints, and secondly, to investigate the influence of axial force in the main member on the initial rotational stiffness of the joint.

To achieve this, the authors utilized a curve-fitting approach and proposed a chord stress function that resembles existing functions used for moment resistance. For their numerical modelling, they employed the Abaqus software, creating a model using 20-noded solid quadratic finite elements with reduced integration (C3D20R in Abaqus). Two elements were used in the thickness direction for both the tubes and the welds. Since the primary failure mode involved the deformation of the top face of the main member, they refined the mesh in that area closer to the connected face. All sections were modelled with rounded corners, in accordance with EN 10219-2 (2006) standards.

For modelling the welds, butt welds were treated as "no weld" using the TIE constraint in Abaqus to prevent relative motion between separate surfaces. Fillet welds were modelled as steel and were associated with the chord using the TIE constraint. The Finite Element Method (FEM) analyses were performed for a single main member size of 300 × 300, with wall thickness t_0 varying from 8.5 mm ($2\gamma = 35$) to 30 mm ($2\gamma = 10$). The width of the connected member changed from 75 mm ($\beta = 0.25$) to 300 mm ($\beta = 1.0$). The analyses were conducted in two steps: first, an axial load was applied to the main member, and then the end of the connected member was subjected to a concentrated in-plane moment in a single increment. This moment corresponds approximately to 0.1 rad and represents a situation where no yielding occurs at the joint area.

The simulation results led to the conclusion that the axial stress in the main member significantly affects its initial rotational stiffness. For compressive loads, the stiffness can decrease by up to 50%, while for tensile loads, it can increase by a maximum of 30%. This observed effect was found to be dependent on the brace-to-chord width ratio β and the chord width-to-thickness ratio γ.

In the context of increasing reliance on numerical modelling in the investigation of steel structures, Kwasniewski and Bojanowski (2015) [59] articulated essential principles for verification and validation in the process of developing integrated studies. The authors aimed to clarify the terminology and address questions related to the Validation and Verification (V&V) process. They discussed principles for comparing numerical results with experimental data, the importance of sensitivity studies, and new ideas about the relationship between research and design finite element models.

In the V&V process, the authors highlighted the distinction between validation and verification. Validation involves comparing numerical solutions with experimental data, while verification entails comparing computational solutions with highly accurate (analytical or numerical) benchmark solutions. Verification can be conducted through tests of agreement between computational solutions and benchmark solutions of various types, including analytical, highly accurate numerical, and manufactured solutions. The goal of verification is to test the agreement of the computational solution with known correct results.

Experimental data used for validation should be treated differently from benchmark solutions used for verification due to the inherent errors and uncertainties associated with experimental measurements. Errors in measurements and calculations are defined as the difference between the result of a measurement (calculation) and the value of the measured (accurate) solution. Uncertainty, on the other hand, characterizes the dispersion of values that could reasonably be attributed to the measured result.

Validating numerical results against experimental data in the design of structural connections, particularly in the context of beam tests for simple connections under shear and cruciform tests for moment-resistant connections under bending moments, is challenging and has limitations. The limitations stem from factors such as economic constraints, the complexity of connection tests, and uncertainties in the behaviour of specimens.

Given these challenges, the authors emphasized the significance of verification, which aims to demonstrate that mathematical models are accurately implemented and that the numerical solution is correct with respect to the mathematical model. The authors concluded that a methodical verification and validation process is essential to prove the correctness of simulated results. Without such a process, the analysis is rendered meaningless and cannot be used for decision-making.

In cases where the analysed events are too complex or costly to test experimentally, hierarchical validation is recommended. While the review of numerical models for HSS connections

demonstrated the adaptability of this approach in studying the structural behaviour of joints, the authors also acknowledged the difficulties associated with mathematical interpretation of phenomena like contact processes and weld modelling. Despite these challenges, numerical simulations have shown good agreement with tests in many cases, although the limitations and complexities of modelling should be carefully considered.

2.4 ANALYTICAL MODELS

Analytical models play a crucial role in understanding joint behaviour and identifying influential parameters. By combining analytical insights with experimental data, it becomes possible to formulate simple and effective expressions for joint strength and stiffness. However, purely analytical expressions can often become overly complex for practical application. As a result, simplified analytical approaches are sometimes employed, serving as lower-bound functions that provide conservative estimates of joint behaviour.

Various strength criteria are used to predict different modes of failure in joints. While multiple criteria may exist for assessing joint strength, there are instances where one or two decisive criteria can be used to predict joint strength. This simplification aids in making predictions more feasible and manageable in practice. The use of analytical models, combined with experimental evidence, helps in developing practical design guidelines for joint behaviour and contributes to the overall understanding of structural connections in steel and other materials.

2.4.1 Yield line model

Traditionally, the design rules for hollow structural section (HSS) joints are established based on either plastic analysis or deformation limit criteria. The use of plastic analysis aims to define the ultimate limit state of the joint, relying on a plastic mechanism that corresponds to an assumed yield line pattern. This approach is well-known and has been applied by researchers in various studies. Notable examples of such studies include Packer (1993) [96], Cao et al. (1998) [13], Packer et al. (2004), and Kosteski et al. (2003) [55].

Wardenier (1982) [141] proposed that for joints with low β-ratios (the ratio of brace-to-chord diameter), the joint strength can be conservatively estimated using a simple yield line analysis. This method, which forms the basis of many analytical strength investigations, relies on a basic technique. For joints with high β-ratios, the model predicts infinite strengths, indicating that other failure modes, such as chord side wall failure, will govern in these cases.

The yield line method provides an upper bound solution for the yield load, prompting the examination of a wide range of potential mechanisms to determine the lowest value that can be deemed acceptable as the failure load. However, various studies have demonstrated that using a simplified yield line pattern, as shown in Figure 2.8 (model *a*), results in only a minor increase

of 1 to 7% in strengths compared to more intricate patterns with yield fans, depicted in Figure 2.8 (model *b*). This finding suggests that the simpler approach can still yield accurate results within this range.

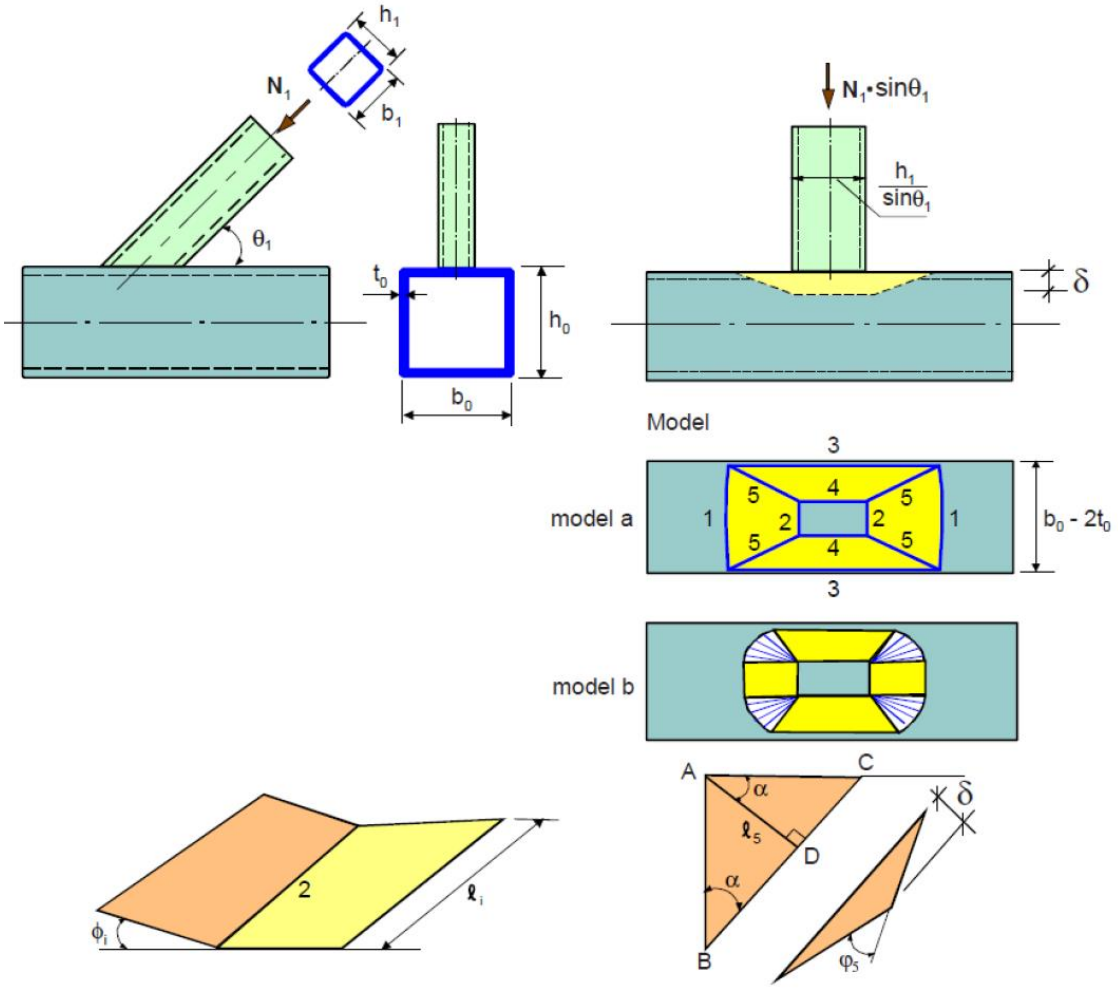

Figure 2.8 Yield line model for a T, and Y joint

Ultimately, these methods contribute to the development of design rules that ensure the structural integrity and safety of HSS joints under various loading conditions. The choice between different analytical techniques depends on the specific characteristics of the joint and the desired level of accuracy in predicting its behaviour.

The yield load capacity is only slightly influenced by a yield line pattern in the side walls of the chord. In the simplified model, the effects of membrane action and strain hardening are ignored. The calculation method consists of equating the work of the external force and the work done by the plastic hinge system, for example, for the T- and Y-joint shown in Figure 2.8. Equating the sum to the external work gives:

$$N_1 \sin\theta_1 = \frac{2f_{y0}t_0^2}{1-\beta}\left(\tan\alpha + \frac{(1-\beta)}{\tan\alpha} + \frac{\eta}{\sin\theta_1}\right) \quad (1)$$

or after improvements:

$$N_1 = \frac{f_{y0}t_0^2}{1-\beta}\left(\frac{2\eta}{\sin\theta_1} + 4\sqrt{1-\beta}\right)\frac{1}{\sin\theta_1} \quad (2)$$

In this model, certain simplifications have been incorporated; for instance, the thickness of the sections has been neglected ($b_0 - 2t_0 \approx b_0$). The same principle applies to the weld sizes, which have not been taken into consideration. Additionally, the impact of the chord load needs to be incorporated, and this will be achieved through a chord load function, Q_f.

For K joints, yield line models can also be utilized. However, the load transfer is more complex in these scenarios due to the intricate stress distribution within the yield hinge area, which is notably influenced by factors like membrane stresses, shear stresses, and work hardening. These complexities result in the analytical models becoming considerably more intricate, ultimately prompting the utilization of semi-empirical formulas for the purpose of design.

2.4.2 Punching shear model

When the bracing is pulled away from the chord connecting face, failure can occur through cracking and, ultimately, rupture of the chord face due to shear stress around the perimeter of the brace connection. This is depicted in Figure 2.9 for a Y-joint.

Because the stiffness along the perimeter is uneven, some parts may lack sufficient deformation capacity to contribute fully to the effective perimeter for punching shear resistance. In other words, only specific sections can be considered effective in resisting punching shear due to this nonuniform stiffness. For instance, in the case of a T or Y joint (as depicted in Figure 2.9), the sections along the chord walls exhibit greater stiffness. Depending on the ratio b_0/t_0 of the chord, a varying portion along the cross walls will be effective, denoted as $b_{e.p.}$.

Chord punching shear arises from the component of the brace load that is perpendicular to the chord face. As a result, the punching shear criterion is formulated as follows:

$$N_1 = \frac{f_{y0}}{\sqrt{3}}t_0\left(\frac{2h_1}{\sin\theta_1} + 2b_{e.p.}\right)\frac{1}{\sin\theta_1} \quad (3)$$

with an assumed yield punching shear of $\frac{f_{y0}}{\sqrt{3}}$ and $t_0\left(\frac{2h_1}{\sin\theta_1} + 2b_{e.p.}\right)$ as effective punching shear area of the chord wall for a T-, Y- or X-joint. It will be clear that $b_{e.p.}$ is a function of b_0/t_0. The smaller b_0/t_0, the larger $b_{e.p.}$. According to Wardenier (1982) [141] the value for $b_{e.p.}$ is determined experimentally.

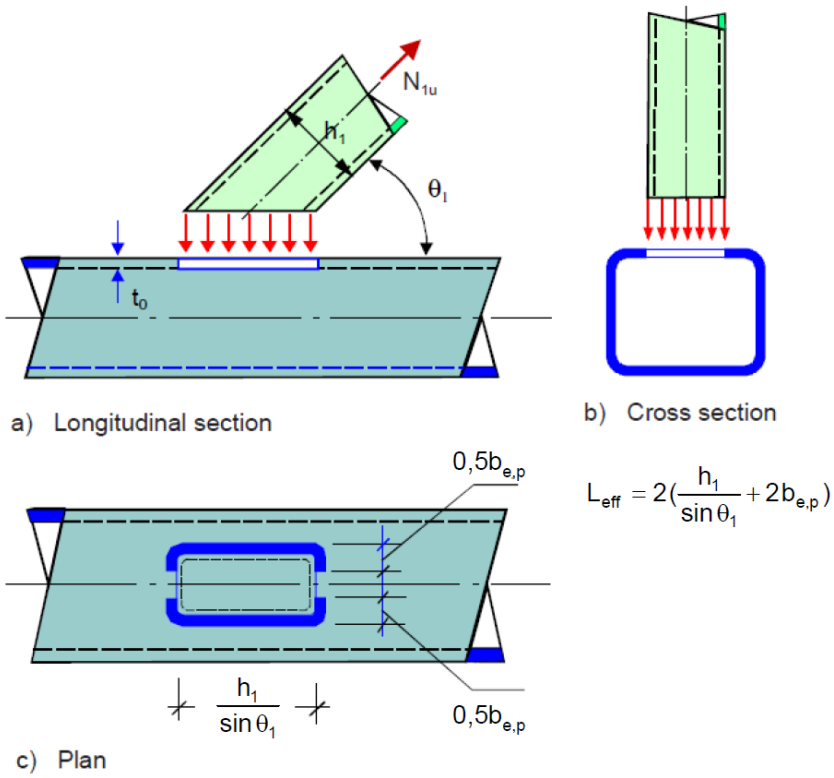

Figure 2.9 Punching shear model for a T-, Y- and X-joint

2.4.3 Local brace failure model

The model used to characterize local brace failure (as shown in Figure 2.10) shares a certain relationship with the chord punching shear model. This similarity arises from the nonuniform stiffness along the connection perimeter. In both models, an effective section is considered. However, due to the distinct deformation capacities associated with brace failure and chord punching shear, the values of b_e and $b_{e.p.}$ differ. Moreover, the causes of these failures differ: chord punching shear results from the brace load component that is perpendicular to the chord, while local brace failure is influenced by the brace load itself. The impact of the angle θ has not been definitively established and, as a precaution, it has been excluded from the current analysis.

For T-, X-, and Y-joints, the criterion for local brace failure can be expressed as follows:

$$N_1 = f_{y1} t_1 (2h_1 + 2b_e - 4t_1) \quad (4)$$

The term "$4t_1$" must be included to prevent double counting of the corners. Similar to the punching shear criterion, the effective width b_e was determined experimentally by Wardenier (1982) [141] and increases when the ratio b_0/t_0 decreases.

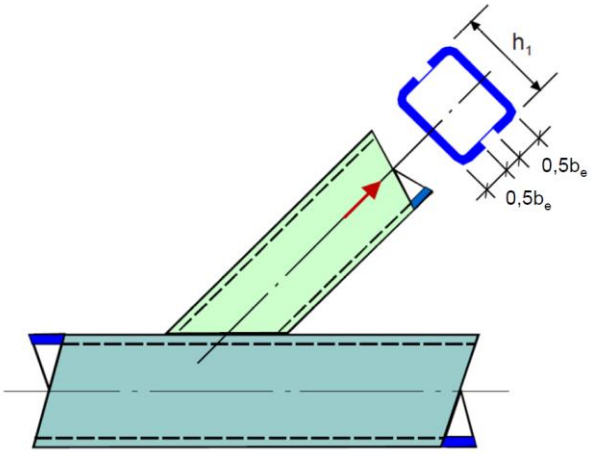

Figure 2.10 Local brace model for a T-, X- and Y-joint

2.4.4 Chord side wall bearing or buckling model

T, Y, and X joints with a high β ratio (typically when $\beta > 0.85$) typically experience failure due to yielding or buckling of the chord side walls, as depicted in Figure 2.11. The model employed for these cases is akin to that used for connections between I-section beam and column joints.

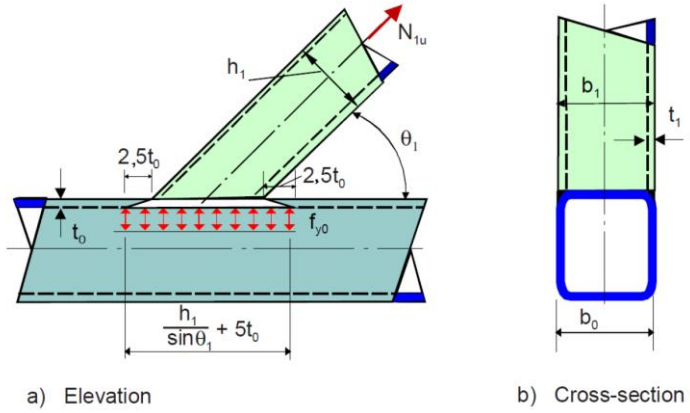

Figure 2.11 Local brace model for a T-, X- and Y-joint

For joints where $\beta = 1.0$, the capacity can be readily determined by:

$$N_1 = 2f_{y0}t_0\left(\frac{h_1}{\sin\theta_1} + 5t_0\right)\frac{1}{\sin\theta_1} \quad (5)$$

For slender walls, the yield stress f_{y0} is replaced by a buckling stress f_k, which is influenced by the chord web slenderness h_0/t_0. This model is straightforward and provides a larger margin of safety for highly slender walls. An improved model that aligns better with test results for all

slenderness values is based on the "4 hinge yield line" mechanism, dating back to the 1970s (Packer, 1978). In cases where the chord side walls are subjected to compression, Yu (1997) [153] also used a buckling stress, but with a buckling length of $(h_0 - 2t_0)/2$.

Based on these models and experimental evidence, both analytical and semi-empirical formulas have been developed. In the context of T, Y, and X joints, the yield line model functions as a conservative lower bound for test results and is also incorporated into established recommendations (EN 1993-1-8:2005 [15], IIW (1989, 2013) [33] [34], Packer (1978), Packer & Henderson (1997) [97], Packer (1993) [96], Packer et al. (2009) [99], Wardenier (1982) [141]). For T, Y, and X joints with β values up to 0.85, the yield line model for chord face plasticization serves as the foundational lower bound formula for joint resistance. However, when β exceeds 0.85, the joint resistance is influenced by factors like chord side wall failure, brace failure, or chord punching shear, specifically when the condition $b_1 < b_0 - 2t_0 - 2(1.4a_w)$ is satisfied.

2.4.5 Models for the in-plane and out-of-plane bending moments

Similar to axially loaded joints, the strength of connections can be characterized either by their ultimate bearing capacity or by a deformation or rotation limit. In cases where bending moments are applied to joints with rectangular chords, stiffness can often play a crucial role in determining their behaviour. According to Wardenier (1982) [141], only joints with a β value of 1.0, as well as joints with β values below 1.0 and low γ ratios, can be considered rigid. All other joints should be treated as semi-rigid. The moment capacity of joints with low β ratios is influenced by limited rotations, wherein the analytical yield criterion of the chord face is taken into account while disregarding the effects of membrane action and strain hardening.

The design resistances for joints subjected to brace bending moments are determined in a manner similar to that for axially loaded joints. To simplify the design process, guidelines also provide limitations on the range of applicability, thereby streamlining the criteria that need to be assessed. For Vierendeel girders, selecting joints with β values of 1.0 is recommended to ensure adequate stiffness and strength. The design resistance formulas are derived from analyses conducted by Wardenier (1982) [141], Dutta & Mang (1983) [28], Yu (1997) [153], and Packer et al. (2009) [99], and they are outlined in relevant guidelines such as those developed by Packer et al. (2009) [99].

As per Packer et al. (2009) [99], in situations where the ratio of bracing width to chord width remains reasonably modest, the simplified yield line model can be employed to ascertain the strength. Consequently, the moment capacity of T-joints can be formulated as follows:

$$M_{ip,1,Rd} = f_{y0} t_0^2 h_1 \left(\frac{1}{2\eta} + \frac{2}{\sqrt{1-\beta}} + \frac{\eta}{1-\beta} \right) Q_f \qquad (6)$$

In T-joints, the occurrence of local buckling in the side walls is relatively less critical compared to joints subjected to axial loading, primarily due to the more localized forces at play. However, when the critical stress linked to side wall buckling is below the yield stress, it results in a shift in the neutral axis. This alteration introduces complexities in adopting a generalized approach.

To maintain consistency with axially loaded joints, the same critical stress is adopted. The distribution of actual stress across the side walls depends on the side wall's slenderness ratio, h_0/t_0, and can exhibit considerable variation. The forthcoming strength formulas will be confined to $h_0/t_0 \leq 35$, thus excluding extremely thin-walled chords. This selection allows for the assumption of a full plastic stress distribution.

Subsequently, the bearing or buckling capacity of the chord's side wall is expressed as follows:

$$M_{ip,1,Rd} = 0.5 f_k t_0 (h_1 + 5t_0)^2 Q_f \tag{7}$$

While the effective width for the tension side may vary from that of the compression side, the decision is made to utilize the same effective width b_e for the bracing cross walls. This choice is substantiated by the assertion made by Wardenier (1982) [141] that there exists no compelling rationale for a disparity in effective width between bracing and axial loading scenarios. Therefore, the effective width b_e, as defined by Eq. (4), is consistently applied.

Thus, the criterion for the effective width is established as follows:

$$M_{ip,1,Rd} = f_{y1}\left[W_{pl,1} - \left(1 - \frac{b_e}{b_1}\right) b_1 (h_1 - t_1) t_1\right] \tag{8}$$

In cases where brace members within joints experience combined loading, the impact of axial load on the joint's moment capacity hinges on the critical failure mode. This interaction is intricate and entails a multifaceted set of interactions. In light of this complexity, a prudent approach is suggested: employing a linear interaction relationship as a conservative measure.

$$\frac{N_{1,Ed}}{N_{1,Rd}} + \frac{M_{ip,1,Ed}}{M_{ip,1,Rd}} \leq 1.0. \tag{9}$$

2.4.6 Component method for T-joints

The component method serves as an approach for characterizing the mechanical properties of structural joints. Initially developed for joints involving open sections, the component method is referenced in Eurocode 3 Part 1.8. It enables the theoretical assessment of resistance, stiffness, and ductility attributes based on mechanical models. However, when it comes to joints concerning tubular HSS (Hollow Structural Sections), a distinct approach is followed.

In the case of tubular HSS, a joint – more precisely, a joint configuration where multiple members connect – is evaluated as a unified entity when determining its resistance(s). Research by Jaspart and Weynand (2015) [35] indicates that existing design regulations for tubular HSS joints derive

from straightforward theoretical mechanical models and are subsequently refined through comparison with experimental tests. This leads to limitations in their applicability, often confined to the range for which the rules have been validated.

Within the framework of CIDECT, a project is underway to establish a unified design approach for steel joints, irrespective of the section type of the connected elements. This endeavour involves expanding the scope of the "component method". To achieve this goal, rules that are recommended for hollow section joints need to be translated into a component-based format.

The research conducted at Liege University under Jaspart's supervision in the mid-2010s has laid the groundwork for this unified design approach. In this context, components specific to typical HSS joints in lattice girder structures have been identified. Moreover, the research presents design regulations encompassing component resistances and assembly guidelines for certain hollow section joints, serving as illustrative examples of the approach in practice.

The approach endorsed by CIDECT Report 5BP-4/05 suggests treating any joint as an aggregation of distinct individual components. Aligning with the principles of the component method, the initial step involves establishing what is referred to as the "list of active individual components". This task entails considering not only the geometrical arrangement of the joint under study but also the nature of the loads it faces, including axial forces, bending moments, shear forces, and combinations thereof.

Following this, the subsequent stage encompasses formulating design resistance equations for each of these individual components in terms of shear, tension, or compression. This derivation is drawn from Chapter 7 of EN 1993 Part 1.8 and involves an appropriate "conversion" process that will be specified.

Once the components are identified and their characteristics defined, the focus shifts to determining how these components interact when assembled. The assembly of components signifies the allocation of forces within the joint's entirety in a manner that fulfils certain criteria:

- The internal forces within components maintain equilibrium with the external forces applied to the joint.
- The resistance of a component remains within acceptable limits.
- The deformation capacity of a component is not exceeded.

Concerning the joint's overall resistance to external forces, adherence to these three principles is adequate to ensure that the calculated design resistance is less than the actual resistance of the joint.

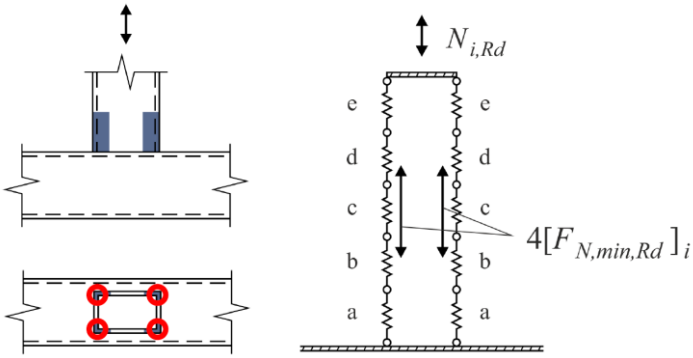

Figure 2.12 Component method assembly

As per the proposed component method, it's conceivable to visualize a joint as a system of springs, where each spring signifies a specific component. Figure 2.12 illustrates this notion for a T-joint involving RHS profiles subjected to axial force. In the diagram, the labels "a" through "e" correspond to the active components, identified as follows:

- Chord face in bending.
- Chord side wall(s) in tension or compression.
- Chord side wall(s) in shear.
- Chord face under punching shear.
- Brace flange or web(s) in tension or compression.

Within Figure 2.12, it's evident that axial forces are transmitted from the brace to the chord through four loading zones situated at the corners of the brace sections. Once this assumption is accepted, it's vital to uphold it throughout the design process. For each brace cross-section type, meticulous consideration must be given to defining the number and positions of the load transfer zones. In the specific scenario depicted, the design resistance of the joint under axial force can be calculated using the following derivation:

$$N_i = 4\left[F_{N,minRd}\right]_i \tag{10}$$

where $\left[F_{N,minRd}\right]_i$, the minimum resistance of the active components (*a*)..(*e*) for joint under axial force. The procedure may be extended similarly to all loading situations and so, at the end, the design resistances of the joint under $N_{i,Ed}$, $M_{ip,i,Ed}$ and $M_{op,i,Ed}$.

The conversion of EN 1993-1-8 chapter 7 into a “component style” requires therefore, for each joint in each joint configuration covered in the normative document, to identify the active components, derive the resistance of these active components and assemble the components successively for each individual loading situations (axial force, in-plane bending moment and out-of-plane bending moment). When this is achieved, the resistance of each joint may then be checked through Eq. (8) of this Chapter adding summand of $M_{op,i}$.

For each joint belonging to a joint configuration, Eq. (8) has to be applied, what requires first to evaluate its three individual resistances $N_{i,Ed}$, $M_{ip,i,Ed}$ and $M_{op,i,Ed}$. To derive these individual resistances, reference is made to the component approach and special rules derived from analytical models presented above.

Component method is acknowledged as perspective and serves as a base of computer oriented approaches development.

2.4.7 Plastic mechanism model by Zhao and Hancock [157]

A plastic mechanism has been formulated by Zhao and Hancock (1991) [157] for T-joints featuring rectangular hollow sections (RHS) subjected to concentrated loads. This model encapsulates various critical factors, including plastic hinges located in the web, membrane forces in the flange, and the influence of material strain hardening. Consequently, this model possesses the capability to project crucial aspects such as the yield load, the post-yield behaviour, and the ultimate load of a T-joint subjected to concentrated force.

In assessing its efficacy, the developed model was benchmarked against existing models, including the CIDECT model, the Kato model, and the modified Kato model. The model's predictions concerning the yield load, post-yield response, and ultimate load are then compared with empirical data from experimental tests. These tests encompass 6 T-joint experiments conducted by Zhao and Hancock (1991) [157] and 20 T-joint experiments conducted by Kato and Nishiyama (1979) [52]. The range of the tested T-joint ratios (denoted as "beta") varies from 0.291 to 0.890.

Figure 2.13 represents the membrane mechanism formulated by Zhao and Hancock (1991) [157].

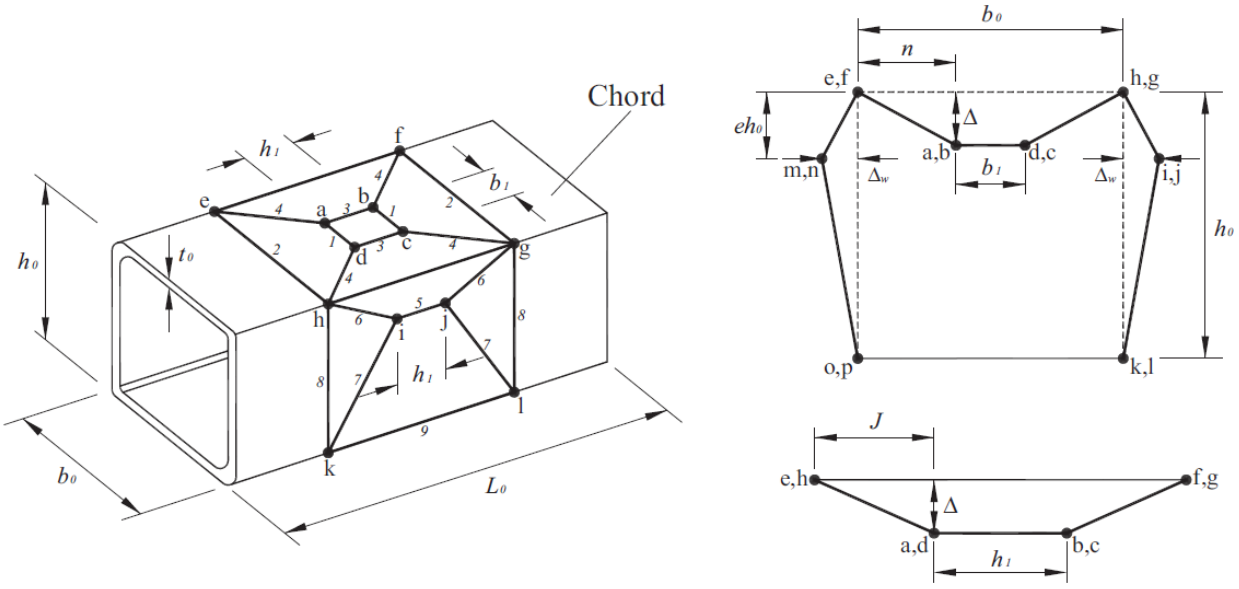

Figure 2.13 Membrane mechanism model for welded tubular T-joint by Zhao and Hancock (1991) [157]

The design strength of connections based on the abovementioned model can be determined using the design equation obtained from virtual work principle, which is summarized as follows:

$$N_{Rd} = P_m + \sum_{i=3,5}^{9} k_i P_i, \tag{11}$$

where $P_m = 2S_y \sin\alpha_y$ is the partial yield load resulted from the membrane force of the chord flange, $S_y = \frac{b_0+b_1}{2} t_0 f_{y0}$ is the membrane force, $\sin\alpha_y = \sqrt{1-\frac{1}{(1+\varepsilon_y)^2}}$ is the plastic hinge rotation angle, k_i is the total number of the i^{th} plastic hinge, P_i is the partial yield load resulted from each i^{th} plastic hinge. The terms k_i and P_i are summarized in Table 2.1.

Table 2.1 Terms k_i and P_i of membrane mechanism model for RHS tubular T-joint [157]

Yield line no. (i)	Number of yield line (k_i)	Contribution of each i^{th} yield line (P_i)
3	2	$P_3 = M_p\left(\frac{h_1}{n}\right)$
5	2	$P_5 = M_p\left(\frac{h_1}{n}\right)\left(\frac{1}{1-e}\right)$
6	4	$P_6 = M_p\left(\frac{e^2\left(\frac{h_0}{b_0}\right)^2 + K^2}{K\left(\frac{n}{b_0}\right)}\right)$
7	4	$P_7 = M_p\left(\frac{(1-e)^2\left(\frac{h_1}{b_0}\right)^2 + K^2}{K\left(\frac{n}{b_0}\right)}\right)\left(\frac{e}{1-e}\right)$
8	4	$P_8 = M_p\left(\frac{e}{K\left(\frac{n}{b_0}\right)}\right)\left(\frac{h_0}{b_0}\right)^2$
9	2	$P_9 = M_p\left(2K\left(\frac{b_0}{n}\right) + \frac{h_1}{n}\right)\left(\frac{e}{1-e}\right)$

The values utilized for the calculation of P_i are represented as follows:

$$M_p = \frac{f_{y0}t_0^2}{4},\ e = \left(\frac{n}{h_0}\right)\beta,\ n = \frac{b_0(1-\beta)}{2},\ \beta = \frac{b_1}{b_0},$$

$$K = 0.5D_1^2D_3 + 0.5D_1\sqrt{D_1^2D_3^2 + 4D_2},\ \varepsilon_y = \frac{\sigma_y}{E},$$

where

$$D_1 = \sqrt{1-\beta}\sqrt{\frac{1-e}{1+e}},\ D_2 = \left(\frac{eh_0}{n}\right)\left(\frac{h_0}{b_0}\right),\ D_3 = \left(\frac{b_0}{t_0}\right)\left(\frac{1+\beta}{2}\right)\sqrt{(1+\varepsilon_y)^2 - 1}.$$

2.5 COMPONENT BASED FINITE ELEMENT METHOD

The Component-Based Finite Element Method (CBFEM) was developed through a collaborative effort involving Czech Technical University in Prague, Brno University of Technology, and the software company IDEA StatiCa. The primary objective was to establish a comprehensive approach capable of addressing connection designs across various types, rather than being limited to specific templates or cases. This initiative sought to create a versatile and adaptable method that could effectively accommodate a wide range of structural connection scenarios. The methodology was documented in publications authored by Šabatka et al. (2014) [165], Wald et al. [134]. Several papers have delved into this subject, including works by Wald et al (2015, 2019, 2020) [135], [137], [138],) Weynand et al (2017) [150], Jaspart & Weynand (2001, 2002) [148], [149]. These contributions encompass a variety of applications, adapting the technology to tubular connections, and diverse scenarios such as seismic joint design and the design of prequalified joints.

The CBFEM is an advanced structural analysis technique that combines the advantages of both the finite element method (FEM) and the component method. It aims to provide a more efficient and accurate approach for analysing complex structures and assemblies.

In traditional FEM, the structure is discretized into finite elements, and the behaviour of the entire structure is analysed based on the interactions between these elements. On the other hand, the component method breaks down a structure into individual components and analyses their behaviour and interactions. It is commonly used for joints and connections, where the focus is on the interaction between different members. CBFEM integrates these two approaches by considering the global structure as a collection of interconnected components, each of which can be analysed independently with a focus on their internal behaviour and interactions. This method allows engineers to handle complex systems while maintaining the accuracy and efficiency of the component method.

Here's a simplified explanation of how CB-FEM works:

Component Modelling: Each structural component (beams, columns, connections, etc.) is modelled individually using traditional FEM. This provides detailed insight into the behaviour of each component under various loads.

Component Interaction: Components are then connected to each other using interfaces that define how they interact. These interfaces could represent joints, connections, or any other type of interaction between components.

Global Analysis: The interconnected components are assembled to create the complete structure. The analysis considers the interactions at the interfaces to capture the global behaviour of the structure.

The benefits of CB-FEM include improved accuracy in capturing localized behaviour, reduced computational effort compared to a full FEM analysis, and the ability to handle complex assemblies more effectively. It is particularly useful for large and complex structures where accurate representation of connections and localized effects is crucial.

The component model offers the advantage of integrating contemporary knowledge of components' behaviours (including bolts, welds, and plates) from both experimental and analytical realms. This leads to highly accurate predictions of behaviour across elastic and ultimate loading levels. The model's validation is feasible through simplified calculations. However, a limitation arises in that experimental assessment of internal force distribution is viable only for a restricted range of joint configurations.

In current academic literature, the description of atypical components is either lacking or possesses limited validity and supportive references. Models for hollow section connections, outlined in Ch. 7 of EN1993-1-8, rely on curve fitting procedures, rendering their compatibility with the component model somewhat unreliable. The complexity of component models can render hand calculations intricate, often necessitating the use of tools or design tables.

The component model of connections builds upon established procedures for evaluating internal forces within connections and their subsequent validation. Zoetemeijer (1990) [164] was the pioneer in imbuing this model with predictive capabilities for stiffness and deformation capacity. Subsequent refinements were made to elastic stiffness, as evidenced in Steenhius's work (1994) [112]. A foundational depiction of component behaviour in major structural steel connections was established by Jaspart for beam-to-column connections [147], followed by Wald et al (2008) [136] for column bases. The model's scope was broadened by da Silva [108]. This methodology is now integrated into the prevailing European structural standard for steel and composite connections, as detailed in [15] and [17]. It finds application in a majority of software used for structural steel in Europe.

Based on [165], the procedure commences with the disassembly of a joint into individual components (for instance, the one illustrated in Figure 2.14). Each component's behaviour is described in terms of its normal and shear force deformation characteristics. These components are then grouped to examine the joint's moment-rotational behaviour. Then, obtained information is employed for classification and representation in a spring/shear model and subsequently utilized in global analyses.

What is more, CBFEM models help visually represent all kind of modes of failure modes and supplements the traditional engineering approach by a well-predicted joint behaviour and safe standard approved resistance.

The multilevel FEA analyses of the structural steel connections based on components (CBFEM) is about to replace the curve fitting and component method designs.

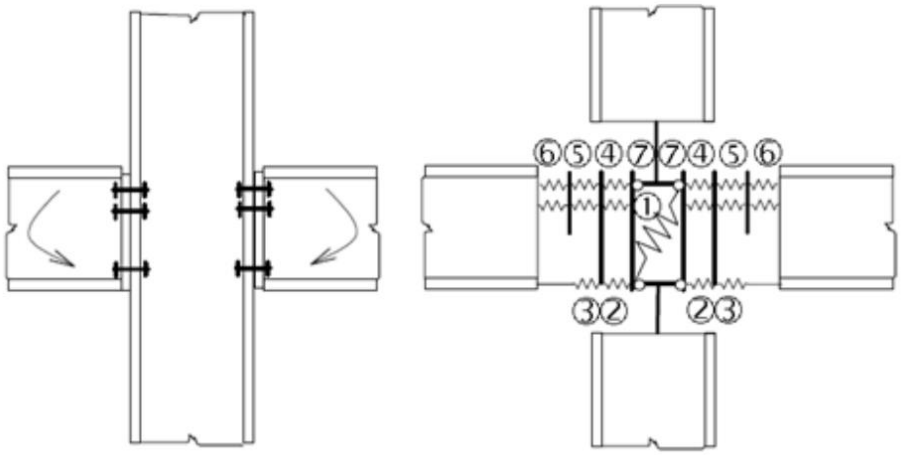

Figure 2.14 Symmetrical beam-to-column connections with end plates in a component model 1 – column web in shear, 2 – column web in compression, 3 – beam flange and web in compression, 4 – column flange in bending, 5 – bolts in tension, 6 – end plate in bending, and 7 – column web in tension

2.6 CONCLUSIONS

Many of the existing design equations are primarily applicable to tubular sections that closely resemble the material properties and dimension ratios found in the specimens used during the experimental validation of these equations. Consequently, while research and design standards for statically loaded 2D truss welded connections among tubular sections (as discussed in IIW (1989) [33], Packer et al. (1990) [95], Syam & Chapman (1996), Packer & Henderson (1997) [97], and AWS (2002) [3]) have been considered mature by certain authorities, there persists a continuous demand for applied research pertaining to the behaviour and strength of such connections when involving rectangular hollow sections with material properties or dimension ratios not addressed by the current standards.

This ongoing need for applied research is driven by the fact that real-world engineering applications often involve a wide range of structural configurations and materials. These may deviate significantly from the idealized conditions assumed in existing design standards. Therefore, engineers and researchers must continually explore and analyse connections involving rectangular hollow sections with unique material properties or dimension ratios to ensure their safety and reliability.

The pursuit of such applied research contributes to a more comprehensive understanding of the behaviour of these connections, enabling the development of more accurate and versatile design approaches. As engineering continues to evolve and adapt to diverse challenges, this research remains a crucial component of ensuring the structural integrity of complex systems involving non-standard sections.

CHAPTER 3:
AIMS AND OBJECTIVES

The main objective of this thesis is to investigate welded connections of RHS structural members, specifically focusing on cases with a lateral offset, particularly situations where the brace member is shifted towards the lateral surface of the chord (referred to as SCE RHS T-shape joints). An example of this joint configuration is illustrated below in Figure 3.1:

Figure 3.1 Stepped connection with eccentricity (SCE) in real-world design practice (photo: S. Kalmykova, Prague)

The aim of this thesis is to determine the resistance of SCE RHS T-shape joints, with a particular focus on stepped connections in the general case of offset.

This doctoral thesis will address the following research tasks:

1. Evaluation of developed design recommendations
   This task involves a critical assessment of existing design guidelines and recommendations related to the T-shaped connections between RHS members with offsets. It aims to evaluate the adequacy and applicability of these recommendations in practical scenarios, identifying areas for improvement if necessary.

2. Experimental study
   This task entails conducting physical experiments to gather empirical data on the behaviour and performance of the welded connections in question. Through carefully designed experiments, the key parameters such as load-carrying capacity and deformation characteristics will be measured.
3. Advanced numerical simulation
   Advanced numerical simulations involve using computational models (a finite element analysis (FEA)) to simulate the behaviour of the connections under various loading conditions. This task allows to explore a wide range of scenarios, including complex geometries and loadings, providing a deeper understanding of connection performance.
4. Validation of numerical simulation
   In this step, the results obtained from numerical simulations are compared and validated against the experimental data collected earlier. This validation process ensures that the computational models accurately represent the physical behaviour of the connections and helps establish confidence in their predictive capabilities.
5. Sensitivity study
   The sensitivity study involves varying key parameters within the numerical models to assess how changes in these parameters impact the performance of the connections. This helps identify critical factors that significantly affect connection behaviour and may inform design considerations.
6. Development of an analytical model

This task focuses on creating a simplified analytical model or method for estimating the strength and behaviour of laterally offset T-connections. It includes the development of a plastic mechanism model for laterally offset joints with varying brace-to-chord eccentricities, a comparative analysis of analytical models for estimating the strength of laterally offset T-connections, and a procedure for verifying the proposed model through numerical simulations conducted by the authors.

Overall, these research tasks encompass a comprehensive approach to investigating and understanding the behaviour of welded connections between RHS members with offsets, combining experimental testing, advanced computational analysis, and the development of practical design tools.

CHAPTER 4:
Experimental research of T-connections with offset

In order to examine the structural behaviour of laterally offset RHS T-connections and corroborate the outcomes of finite element simulations, an experimental program was devised. This program entailed conducting 7 full-scale connection tests on cold-formed RHS members, in addition to performing material tests on relevant HSS members. Throughout these tests, measurements were taken to determine the vertical displacement of the brace at the loaded tip and local strains. Simultaneously, observations were made to identify the failure modes displayed by the specimens. Ultimately, the final ultimate axial compressive and rotational capacities were ascertained based on the results obtained from these experiments.

4.1 PROGRAMME AND METHODOLOGY OF LABORATORY TESTS

The research program presented as part of this current study involves conducting experimental tests on full-scale offset T-joints with the parameters $\beta = 0.3$, $\mu_0 = 25.0$, $\mu_1 = 7.5$, $\gamma = 12.5$, These particular parameters were intentionally chosen to lie at the boundaries or beyond the scope indicated in reference [34]. This specific parameter selection aims to encompass a comprehensive range of joint geometries.

Each individual specimen consisted of cold-formed rectangular hollow sections that adhere to the EN 10219-2 standard. This includes employing a 150x100x4 mm RHS member as the chord and a 50x30x4 mm RHS member as the brace. The testing conditions encompassed applying an axial force along the brace's centreline and an in-plane bending moment at the top of the brace.

The welds that joined the brace and chord members were designed in accordance with EN 1011-1:1998 specifications and were executed using shielded metal arc welding techniques. The dimensions of the welds in the test specimens exceeded both 4t and 4 mm. Welding was carried out utilizing 4.0 mm electrodes of E4303 type, which have a nominal 0.2% proof stress, tensile strength, and elongation of 378 MPa, 421 MPa, and 32%, respectively. These specific electrodes were selected for welding low carbon steel (S235 and S355) specimens. These strict welding criteria and the required thickness of the brace member were established to ensure that failure in the specimens would occur within the chord members rather than the welds or brace.

The experimental program consisted of conducting 7 distinct tests on isolated welded RHS-to-RHS T-type connections. The specific details of the test program are outlined in the table below.

Table 4.1 Details of T-type specimens

Label of specimen	Number of tested specimens	Type of Specimen	Steel grade		Type of applied load
			Brace	Chord	
1.01.T.Ec.Co.235	1	Offset from the centreline	S355	S235	Axial force
1.02.T.Ec.Co.355	1	Offset from the centreline	S355	S355	Axial force
1.03.T.Ec.Be.235	1	Offset from the centreline	S355	S235	In-plane moment
1.04.T.Ec.Be.355	1	Offset from the centreline	S355	S355	In-plane moment
2.02.T.Sy.Co.235	1	Without offset	S355	S235	Axial force
2.04.T.Sy.Be.235	1	Without offset	S355	S235	In-plane moment

NOTE. The specimens are categorized based on their joint configuration, steel grades, and the type of external load applied. For instance, the label "1.01.T.Ec.Co.235" delineates the following aspects of the T-joint: "1." signifies the joint's number, "01." corresponds to the specimen's index number, "T.Ec" designates the joint type as T-eccentric (or alternatively, "E.Sy" for Edge-symmetric), "Co" specifies the applied load type as Compression (or "Be" for Bending), and "235" denotes the steel grade, such as S235 JRH (or "355" for S355 J2H).

Table 4.2 Test specimens' nominal geometry

Specimen label	Chord sizes $h_0 \times b_0 \times t_0$ [mm]	Brace sizes $h_0 \times b_0 \times t_0$ [mm]	Ratios		Chord length [mm]	Brace length [mm]	Weld size [mm]
			β	2γ			
1.01.T.Ec.Co.235	150x100x4.0	50x30x5.0	0.3	12.5	924	262	5.0
1.02.T.Ec.Co.355	150x100x4.0	50x30x5.0	0.3	12.5	924	262	5.0
1.03.T.Ec.Be.235	150x100x4.0	50x30x5.0	0.3	12.5	924	262	5.0
1.04.T.Ec.Be.355	150x100x4.0	50x30x5.0	0.3	12.5	924	262	5.0
2.02.T.Sy.Co.235	150x100x4.0	50x30x5.0	0.3	12.5	924	262	5.0
2.04.T.Sy.Be.235	150x100x4.0	50x30x5.0	0.3	12.5	924	262	5.0

All the specimens were constructed using a specialized setup consisting of a supporting frame and a bearing platform, as depicted in Figure 4.1. During the experimental tests involving compression, the underside of the RHS steel chord was in direct contact with the bearing platform, while an axial compressive load was applied at the brace's tip. This close contact was ensured by affixing two specifically designed plates at the ends of the specimen's chord, securely fastened to the platform using screw clamps.

To ensure stability, the support frames were robustly anchored to the solid floor using anchor bolts. The application of axial compression and lateral force to the brace members of the test

specimens was facilitated by a hydraulic jack with a capacity of 1000 kN. This process was carefully monitored using a load cell, which was positioned concentrically between the hydraulic jack and the reaction frame.

Figure 4.1 Test setup of the T-joint specimens

The measurement arrangement for displacement and strain gauges is depicted in Figure 4.2, using specimen "2.02.T.Sy.Co.235" as an illustrative example representing the entire test series. This specimen was selected due to its representativeness.

For the specific case of specimen "2.02.T.Sy.Co.235," two displacement gauges, namely TS01 and TS02, were strategically positioned on separate supports to measure the principal displacements of the chord face within the punching area. Additionally, eight strain gauges were employed to assess local displacements. Among these, four strain gauges (SG01 to SG04) were aligned with the direction of the most pronounced web deformations and were affixed to the chord webs' opposite faces, parallel to the axis line. Another four strain gauges (SG05 to SG08) were oriented to capture the maximal flange strains and were placed on the top surface of the chord flange.

Throughout the tests, a data acquisition system was utilized to systematically record both the applied load and the strain measurements at regular intervals. This comprehensive measurement plan provided invaluable insights into the structural behaviour of the specimen under the specified testing conditions.

The tests were executed using a varying loading rate. The loading program for all specimens was composed of four distinct stages. In the initial stages of the tests, ranging from an unloaded state to approximately 30% to 35% of the ultimate load capacity (P_{ult}), the rate of loading was marked by higher values of 0.25 mm/min. As the deformations of the specimens increased, the rate of loading gradually decreased to 0.1 mm/min, with a reduction step of 0.5 mm/min. This approach allowed for a controlled assessment of the specimens' behaviour across different deformation levels and loading conditions.

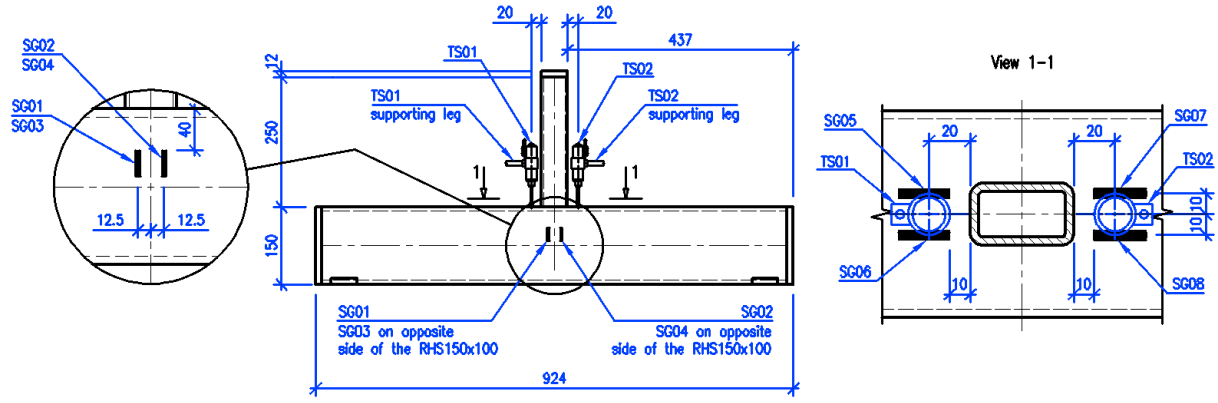

Figure 4.2 Arrangement of displacements gauges

4.2 MATERIAL PROPERTY TESTS

Tensile coupon tests were carried out to acquire accurate material properties for an advanced finite element model. These coupons were extracted from material specimens (additional pieces made from the same material) and subjected to testing in the rolling direction. A total of 8 tensile tests were conducted: 3 on S235 JRH steel and 3 on S355 J2H material sourced from chord elements, along with 2 tests on S355 J2H material taken from brace elements. To prevent hardening-affected zones in corners, all coupons were cut from the mid-plane of the profile facets.

The material properties, encompassing Young's modulus E, ultimate tensile stress σ_u, and the corresponding strain ε_u, were meticulously recorded. Each tested coupon had a nominal thickness of 4 mm and a nominal width of 18 mm in the necked region. Figure 4.3 depicts a representative coupon both before and after testing. The tensile tests were conducted with a focus on strain control, adhering to the strain rates defined in line with ISO 6892-1 standards: 0.1 mm/min for the initial phase of testing, up to approximately 1% strain, and subsequently increased to 2.2 mm/min.

For accurate longitudinal strength measurement, an MTS extensometer with two contact points was directly affixed to the testing coupons. The resulting stress-strain curves for each individual specimen are illustrated in Figure 4.4, presenting a comprehensive insight into the behaviour of the materials under tension.

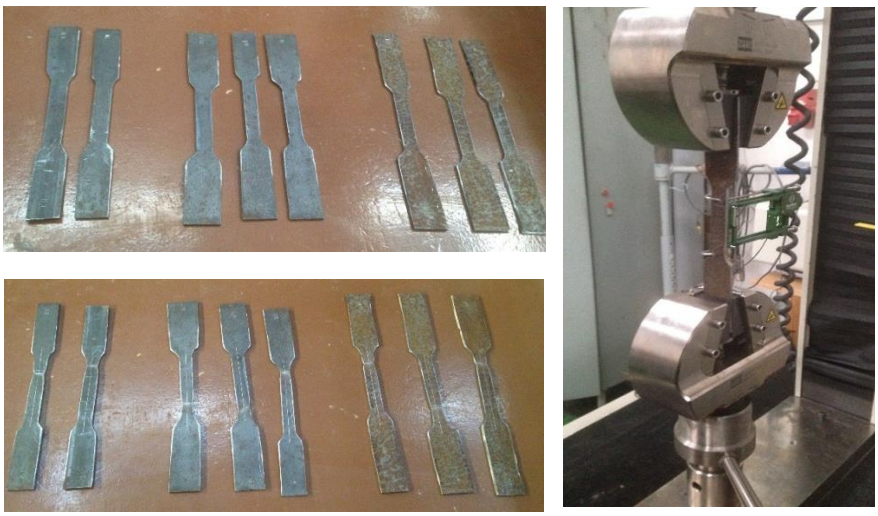

Figure 4.3 Coupon tests specimens and scheme of loading

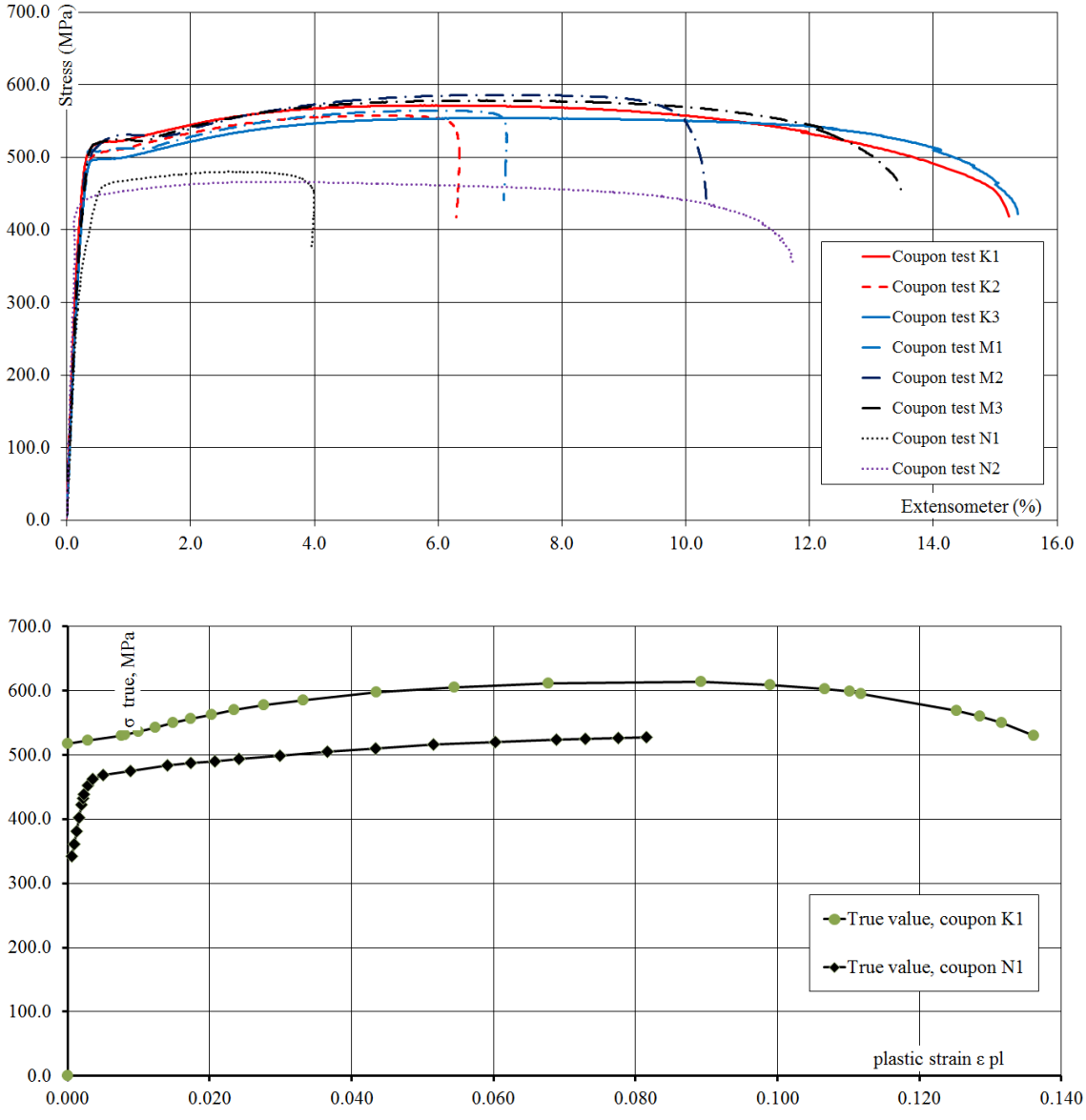

Figure 4.4 Stress-strain curves: a) measured stress-strain curves, b) true strength-strain curves

4.3 TESTS RESULTS AND DISCUSSION

During the vertical loading phases, the joints experienced destruction following a sequence of elastic and significant plastic deformations. In the initial elastic stage, the deformations were notably modest. As the load increased, the RHS brace member exhibited minimal deformation due to its relatively high stiffness in comparison to the RHS chord member. The chord's flange and webs exhibited gradual yielding based on the loading scheme and the type of specimens.

The failure modes of the specimens without offset, specifically specimen "2.02.T.Sy.Co.235", are visually illustrated in Figure 4.5. These modes are characterized by the initial yielding of the flange within the joining area, followed by a progressive involvement of the adjacent zones of the chord webs in the plasticization process. In both types of specimens, plasticisation of the chord webs commenced subsequent to the flange yielding phase. These observations collectively depict the intricate mechanical behaviour and deformation patterns exhibited by the tested specimens under various loading conditions.

2.02.T.Sy.Co.235

Figure 4.5 The mode of failure of the joint without offset

The failure patterns exhibited by the “1.XX..” specimens revealed a simultaneous occurrence of local buckling in the web beneath the brace and yielding of the flange, as depicted in Figure 4.6.

1.01.T.Ec.Co.235

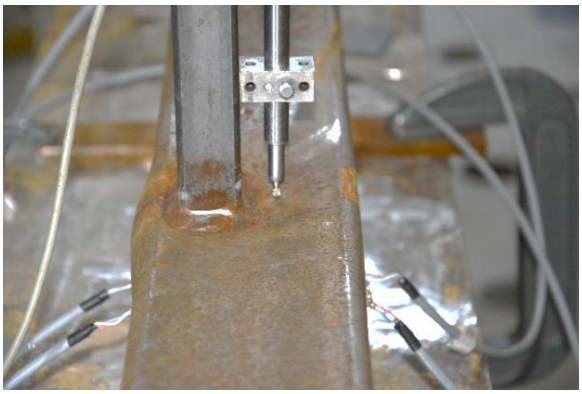

1.02.T.Ec.Co.355

1.03.T.Ec.Be.235

1.04.T.Ec.Be.355

Figure 4.6 The mode of failure of the joint with offset

Local buckling was observed at the upper third section of the chord web, and no noticeable variations in the failure modes were detected between the chords made from steel with differing grades.

4.4 LOAD-DISPLACEMENT CURVES

The load-displacement diagrams, which serve as essential validation data, have been derived from laboratory experiments. These diagrams are visually presented in Figure 4.7. Within this dataset, there is "Specimen 1.01.T.Ec.Co.235," distinguished by its offset from the centreline, and "2.02.T.Sy.Co.235," representing a joint with a traditional geometry.

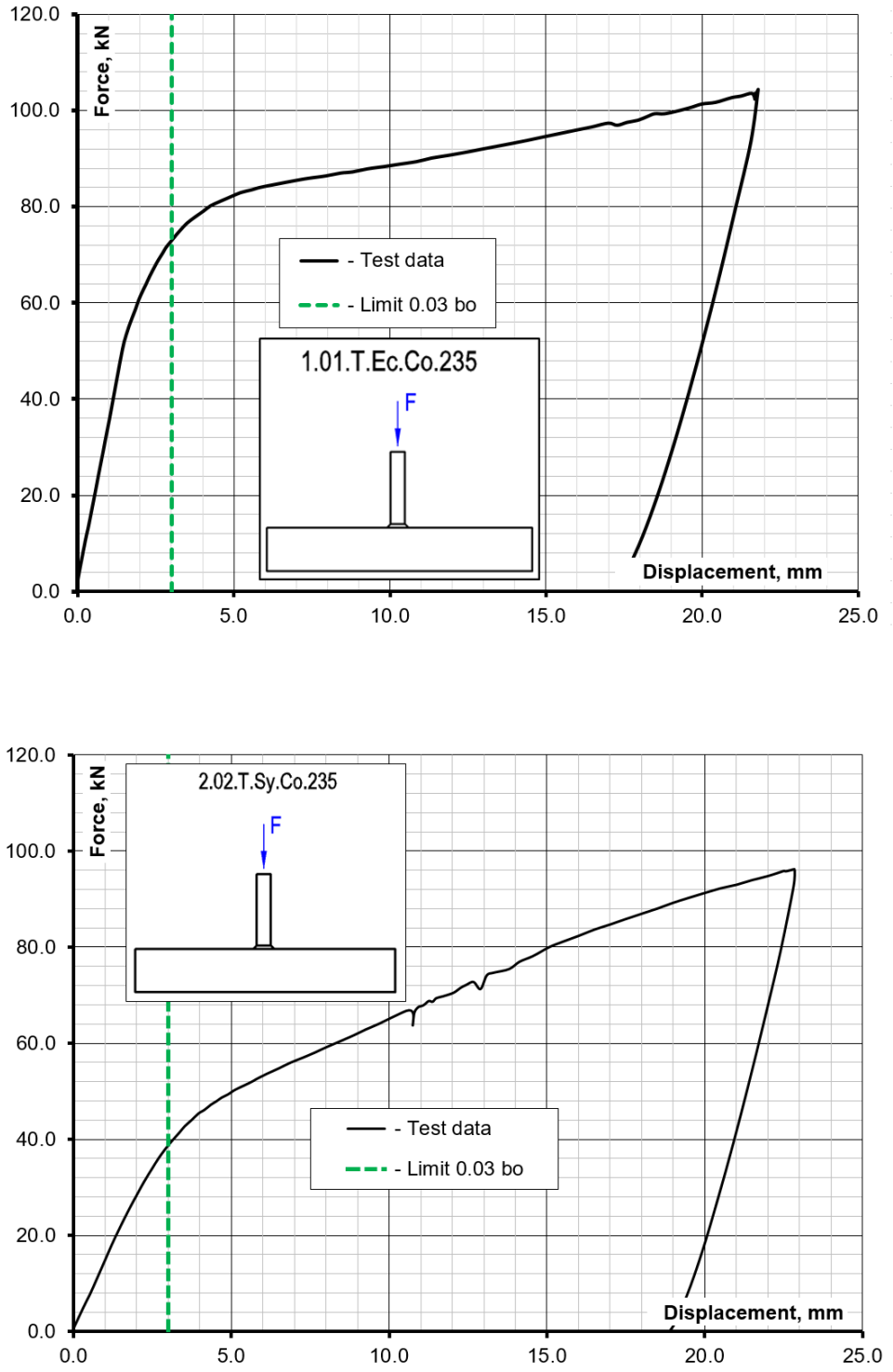

Figure 4.7 Load-displacement diagrams

CHAPTER 5:
FINITE ELEMENT SIMULATIONS

The joint strength, failure modes, and load-displacement curves of the joints can be determined through accurate numerical analysis. Given the cost-intensive nature of physical laboratory experiments, it becomes highly crucial to explore methods for efficient numerical simulation of joints to reliably anticipate their structural behaviour.

The utilization of finite element techniques for modelling demands the creation of models that strike a balance between accuracy and simplicity. These models must be sufficiently accurate to provide reliable results while also being streamlined enough to prevent excessive consumption of computational resources, especially when conducting parametric studies.

5.1 METHODOLOGY OF FE SIMULATION

5.1.1 General modelling

The comprehensive finite element software ABAQUS 6.14 was employed to carry out numerical modelling for the fully welded offset T-joints. These joint models were constructed in line with the evolving prEN 1993-1-14: 2020 standard. To analyse the load-displacement behaviour nonlinearly, the (STATIC, RIKS) procedure available in the ABAQUS library was utilized. Both geometric and material nonlinearities were incorporated into the FE models. To ensure precise outcomes while maintaining computational efficiency, the selection of element types and mesh sizes for the RHS members and welding materials underwent meticulous evaluation through sensitivity studies and verification procedures.

The FE analysis encompassed crucial aspects, including material and weld modelling, as well as loading and boundary conditions. This rigorous approach facilitated the incorporation of various significant factors, resulting in accurate and comprehensive simulations of the joint behaviour.

5.1.2 Finite element selection

A finer finite element (FE) mesh contributes to improved calculation results. The necessary mesh density can be influenced by a variety of factors, including the types of elements utilized, the shapes of elements, and the size of elements. Ensuring an appropriate aspect ratio for the elements is also of significance to maintain accurate simulations.

Three types of solid elements and one type of shell elements were employed for the sensitivity study. Figure 5.1 illustrates the primary Abaqus elements that were utilized.

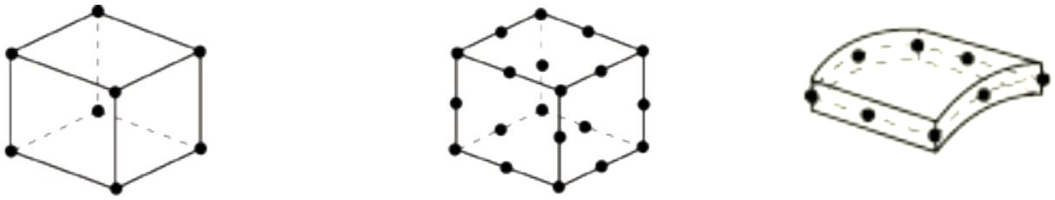

Linear element, 8-node brick | **Quadratic element, 20-node brick** | **Shell element**

Figure 5.1 Element library covered in the study

The following are the types of elements used:

C3D8I: This 8-node linear *brick* element incorporates incompatible modes and serves as an improved version of the C3D8 element. It effectively eliminates shear locking and significantly reduces volumetric locking. This is achieved through the addition of "bubble functions" to the standard shape functions, which possess zero values at nodes and non-zero values between them.

C3D8R: An 8-node linear *brick* element with reduced integration and hourglass control. The utilization of reduced integration minimizes the occurrence of locking phenomena observed in the C3D8 element. However, this element may exhibit reduced stiffness in bending and other limitations.

C3D20R: This 20-node quadratic *brick* element incorporates reduced integration. It performs exceptionally well for general purposes. It excels in cases of isochoric material behaviour and bending, while seldom demonstrating hour-glassing despite reduced integration. It may increase model complexity and CPU usage, but the trade-off results in more accurate outcomes.

S4R: A 4-node quadrilateral stress/displacement *shell* element featuring reduced integration and a large-strain formulation. These general-purpose elements offer robust and precise solutions across all loading conditions, effectively addressing thin and thick shell problems.

The selection of these diverse element types was made with the intention of facilitating the sensitivity study, thereby allowing for a comprehensive investigation into their behaviours and performance across a range of scenarios.

5.1.3 Loading

To facilitate numerical analysis and enhance convenience, the loading plates were emulated through the incorporation of an analytical rigid plate. This approach was complemented by the inclusion of a reference point, strategically designed to streamline the numerical evaluation process. The visual representation of this setup can be observed in Figure 5.2.

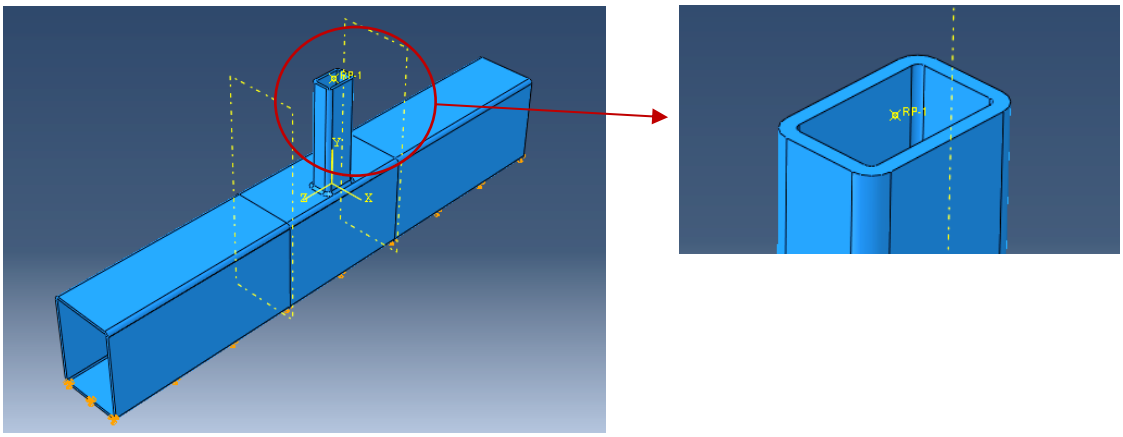

Figure 5.2 Displacement of the reference point and boundary conditions on the model

5.1.4 Material properties

In the context of analysing elastic-plastic bodies using Abaqus, material properties of a specimen are allocated through two dialogue boxes: the mechanical elastic properties box and the plastic material behaviour box (see Table 5.1). The elastic behaviour of steel is represented by linear elasticity involving Young's modulus. Elastic characteristics are characterized as isotropic properties. To model isotropic plastic behaviour in ABAQUS, the Mises yield surface is utilized, and plasticity data are defined in relation to true stress versus logarithmic plastic strain.

Table 5.1 Mechanical behaviour properties of materials assigned in Abaqus for the specimens

Elastic Isotropic

	Fracture Strain	Stress Triaxiality	Strain Rate
1	1	0.3	0
2	0.3	1	0

Ductile Damage

	Young's Modulus	Poisson's Ratio
1	201000	0.3

Plastic Isotropic

	Yield Stress	Plastic Strain
1	320	0
2	355.594	2E-005
3	365.568	0.01806
4	420	0.04679
5	459.563	0.07013
6	492.25	0.09297
7	517.5	0.11532
8	537.625	0.1372
9	567	0.17962
10	587.5	0.22035

5.1.5 Boundary conditions

When modelling welded tubular T-joints, the upper end of the brace and the lower supporting plate were restricted in all directions except for the displacement aligned with the applied load direction.

In terms of the joint's boundary conditions, the chord member was positioned on a rigid base, effectively preventing any rotation or displacement.

5.1.6 Description of FE model: brick model

The section presents a description of the finite element (FE) model, focusing on the brick model. The FE model in Abaqus was constructed using all three types of solid elements proposed for the analysis.

Dimensioning and aspect ratio

The illustrative finite element mesh of the T-joint, as depicted in Figure 5.3, consists of two distinct regions with varying mesh sizes. Specifically, a more refined mesh, composed of four elements, was applied to the corner sections. This finer meshing was deemed necessary due to the critical role these corners play in transferring stress from the flange to the web.

The smaller mesh region employed brick elements (FE bricks) with dimensions of up to 4×4×4 mm. These elements were systematically distributed along the chord's longitudinal axis at an interval of 240 mm. The propagation of the smaller mesh region along the brace chord extended over a distance of 300 mm. In designing the FE bricks, careful attention was paid to maintain an aspect ratio of less than 3, and isoparametric angles were controlled to prevent any distortions within the FE bricks.

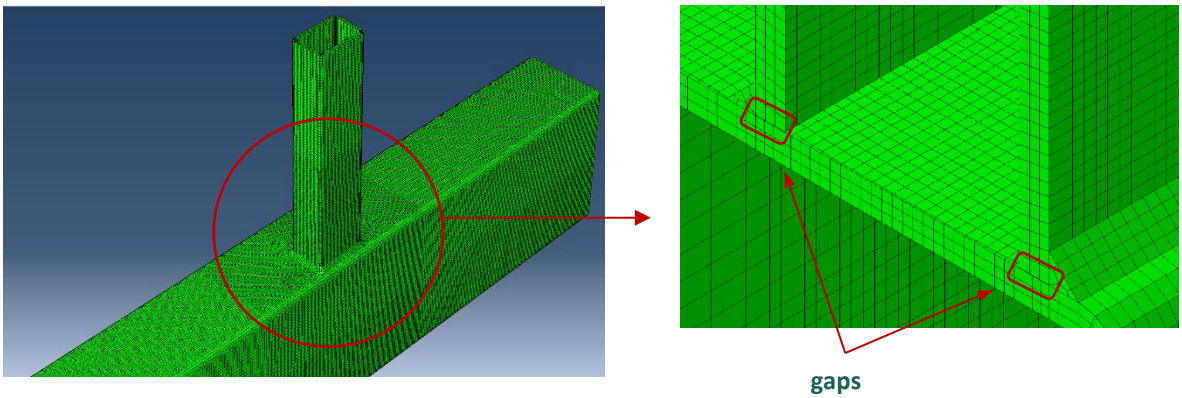

Figure 5.3 The finite element mesh employed for the T-joint analysis

Welding seam

Considering welding seam in FE models is crucial due to it substantial impact on the behaviour of T-joints, particularly in the corner zones of the welds. Welding introduces localized changes in material properties, stress concentrations, and potential failure points. Including weld in FE models provides a more realistic representation of the actual behaviour of the joint. This enhances the model's predictive capability. Therefore, a weld seam was decided to include into the models.

For simplification purposes, the material attributes of the welds were approximated to be identical to those of the entire model. This is because investigating weld material properties becomes complex when the electrode's composition mixes with the joint's main material.

The types of FE solid elements employed in the analysis harmonize seamlessly with the selected model type. The linkage between the brace and the chord was established exclusively through the implementation of weld seams. To achieve this, a deliberate gap was introduced at the juncture of the brace's cutting section and the chord's surface (see Figure 5.3). This advanced modelling strategy was executed during the inception of the FE models, taking into account specialized prerequisites within the meshing procedure.

In-depth quantity of layers

A detailed analysis was conducted to investigate the optimal number of in-depth quantity of layers in relation to element size and the layers within the thickness of the RHS wall. The outcomes of this investigation are provided below.

To assess the impact of the number of elements across the thickness, a specimen denoted as “2.02…” was simulated using one, two, and three layers of elements. These simulations were then compared to the results obtained from the corresponding experimental test.

Table 5.2 Sensitivity study, specimen “2.02…”

Model No.	Number of elements through thickness	Element type acc. to CAE classification	Approximate element size at intersection, [mm]	Experimental strength F_{Ex} , [kN]	FE model strength F_{FE}, [kN]	$\frac{F_{Ex}}{F_{FE}}$
Step 1						
A	1	C3D8R	5		2.57	0.065
B	1	C3D8I	5		40.08	1.016
C	1(2)*	C3D20R	5		35.94	0.911
Step 2				39.45		
D	2	C3D8I	4		38.57	0.978
E	2	C3D8R	4		32.61	0.827
Step 3						
F	**3**	**C3D8R**	**3**		**33.81**	0.857

Model No.	Number of elements through thickness	Element type acc. to CAE classification	Approximate element size at intersection, [mm]	Experimental strength F_{Ex} , [kN]	FE model strength F_{FE}, [kN]	$\frac{F_{Ex}}{F_{FE}}$
G	-	S4R	3		35.39	0.897

* Results for one and two layer of elements are almost equal

The design of HSS joints is grounded in the concept of limit states, specifically the "maximum load carrying capacity". This concept, as defined by IIW Sub-commission XV-E, is determined by the lower of two factors, namely, a) the ultimate strength of the joint and b) the load corresponding to an ultimate deformation limit.

For condition b), the ultimate deformation limit is commonly established as a 3% deformation of the RHS chord face relative to the width of the connecting face ($0.03b_0$). This criterion is generally utilized in defining the strength of both physical (F_{Ex}) and FE models (F_{FE}). The application of this strength criterion is one of the considerations in identifying the most suitable combinations of FE model settings. The selection process also accounts for computational expenses and alignment with experimental outcomes.

The sensitivity study was conducted in three phases. In the initial phase, a single layer of elements was chosen for each type of solid element. For C3D8R elements (model A), the determined strength falls below the defined resistance, revealing an inadequacy in the quantity of layers. C3D8I elements (model B) yield a slightly higher value, while the quadratic brick C3D20R (model C) demonstrates that a single layer of elements is sufficient to attain results with acceptable accuracy. However, the computational costs associated with a model using these elements are notably higher compared to other elements, rendering them less favourable for further application.

The second phase involves augmenting the number of element layers to two. Despite C3D8I elements (model D) showing minimal disparity in strength compared to laboratory test results, they exhibit inadequate agreement with the experimental force-displacement curve during the plastic phase (Figure 5.4).

Model F, composed of three layers of C3D8R elements, emerges as the optimal choice, offering a blend of sound convergence with the experimental force-displacement curve, manageable computational expenses, and alignment with the $0.03b_0$ strength criteria.

Furthermore, the viability of model G, formulated with S4R shell elements, was also assessed. This model satisfies all three criteria, warranting its suitability for continued utilization in the modelling process.

It is evident that with an increase in the number of elements across the thickness, both the strength of the numerical model and its convergence toward the experimental result also increase, as depicted in Figure 5.4.

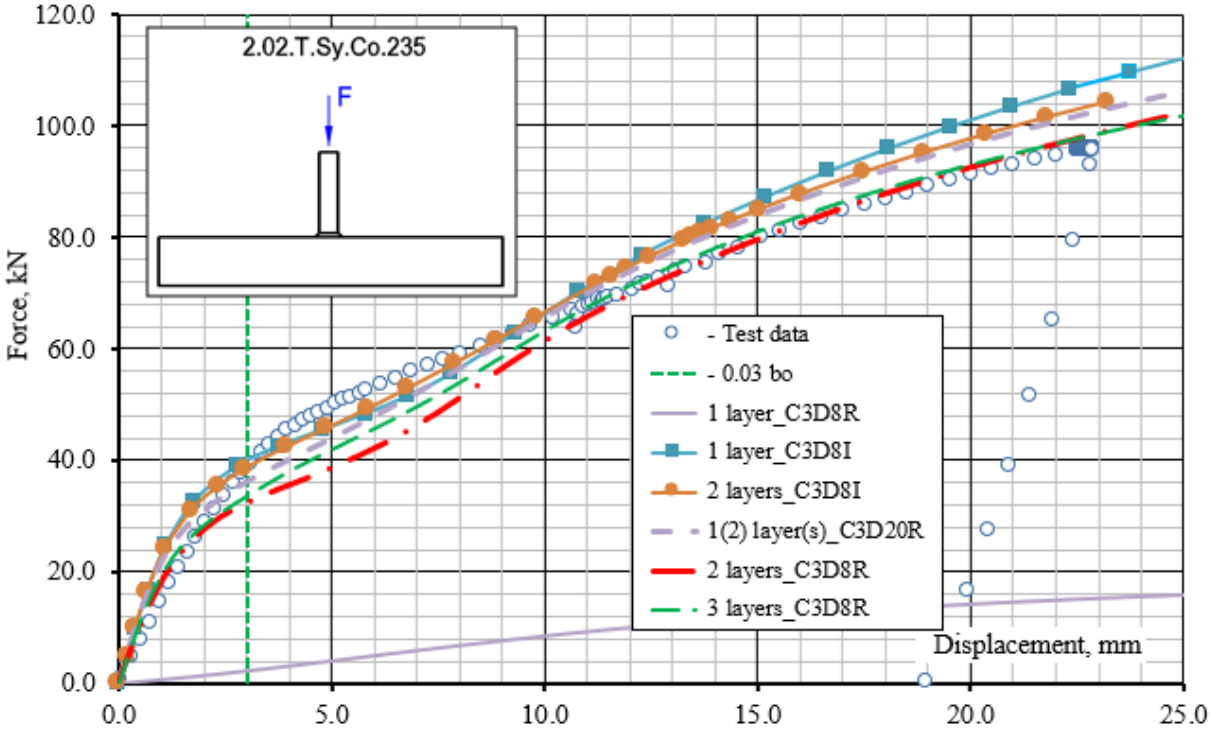

Figure 5.4 Force-displacement curves for sensitivity study, Specimen "2.02…"

FE models constructed using 3-layer C3D8R solid elements and S4R shell elements were chosen for validation purposes.

5.1.7 Description of FE model: shell model

In addition to the primary procedure for validating the numerical model, a comparative analysis of similar finite element (FE) models was undertaken. These models consisted of solid elements (C3D8R) described above, as well as their corresponding counterparts constructed with shell finite elements.

For the modelling of brace and chord members, a four-node doubly curved shell element with reduced integration (S4R) was employed. A five-point integration scheme was applied across the shell's thickness, offering a full set of six degrees of freedom per node. During modelling, the sections of the joint's brace and chord were represented by their mid-surfaces, incorporating thicknesses corresponding to the actual component thicknesses. This approach aligns with findings from previous studies (Korol and Mirza [53], Matos et al. [82], [83]) that indicate shell elements yield accurate solutions for various applications, effectively considering transverse shear deformation, a vital factor for simulating thick shell elements.

It's worth noting that some researchers choose to omit welds when employing shell elements to model welded tubular joints, simplifying the process but potentially leading to an underestimation of joint strength. However, in the case of the discussed specimens, the weld

seam was taken into account. A solid "ring" of shell elements was utilized along the intersection region of the brace and chord, accurately representing a filled weld with a throat thickness of 10 mm, as per the methodology outlined by van der Vegte et al. [124].

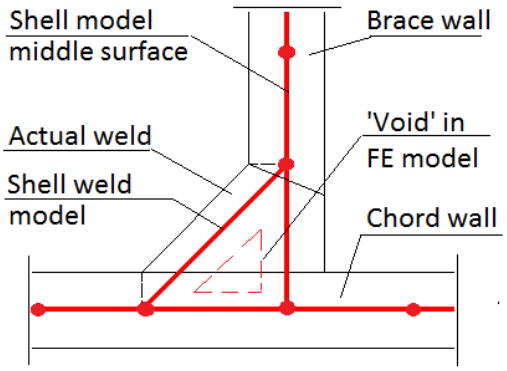

Figure 5.5 Inclusion of Weld Seam in Shell FE Models

5.2 VALIDATION OF FE MODELS AGAINST EXPERIMENTAL RESULTS

In preparation for the finite element study, a comprehensive analysis was conducted to compare experimental data with numerical outcomes. The validation procedure adhered to the principles set forth by Wald et al. [134]and was further informed by laboratory investigations undertaken by the authors [49].

Experimental tests were carried out on a typical T-joint consisting of RHS profiles with dimensions of 50×30×4 mm for the brace and RHS 150×100×4 mm for the chord. The load-displacement curve derived from these tests served as a foundation for validation. The physical dimensions and material properties of the joints were accurately replicated in the modelling process. This enabled an examination of joint strengths, load-axial shortening curves, and deformed shapes, while considering various failure modes of the RHS T-joint.

Material nonlinearity behaviour was effectively incorporated into the finite element models by leveraging preliminary coupon tests conducted by the authors, as outlined in [49].

The finite element models used for testing comprised both brick models and a model composed of shell elements. Multiple types of volumetric finite elements (C3D8R, C3D8I, C3D20R) from the ABAQUS library were employed to assess time consumption and the accuracy of results for models employing brick elements. The sensitivity of the models was evaluated by varying the number of layers across the chord and brace wall thickness. After a thorough sensitivity analysis, a mesh with 3 layers across the member's thickness was chosen due to its optimal balance of computational efficiency and acceptable calculation results (see Chapter 5.1.6).

Comparisons of load-axial shortening curves obtained from both experimental and numerical analyses are illustrated in Figure 5.6 for the general (coaxial joints) and offset T-joints,

respectively. The agreement between experimental and numerical results is remarkable, and all three-dimensional finite element types exhibit satisfactory convergence with the test curve.

Notably, the model composed of C3D8R brick elements closely aligns with the envelope curve, particularly at higher applied load levels. Therefore, it was chosen for the further analysis.

a)

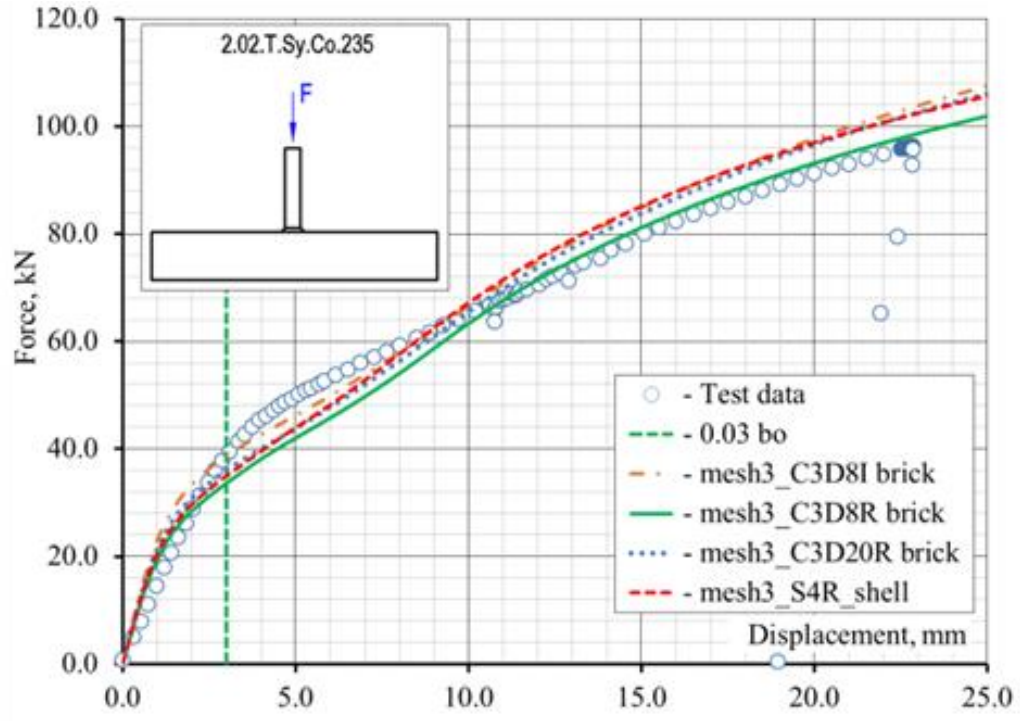

b)

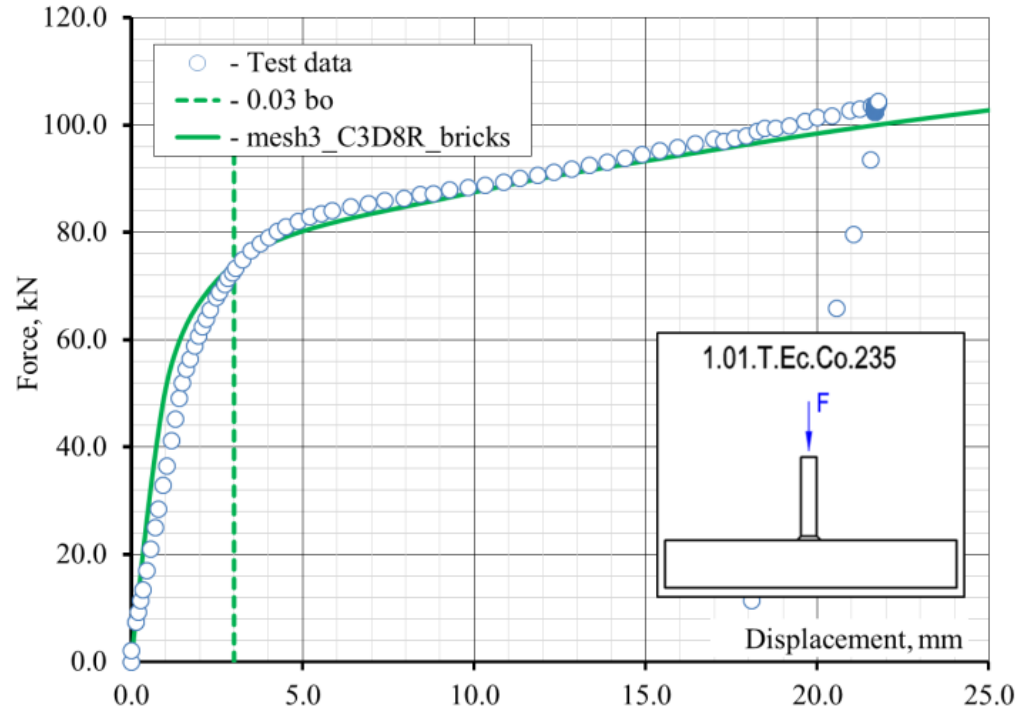

Figure 5.6 Validation of FE models against experimental data

5.3 SENSITIITY STUDY

Taking into consideration that the behaviours of the analysed welded joints are governed by parameters tied to the dimensions of the loaded region (brace section dimensions) and the dimensions of the loaded chord face (represented by parameters β and γ), a comprehensive range of geometries was established, outlined in Table 5.3.

For the T-geometry structure, a cross-section of 300×250 mm was adopted for the chord. The parameter γ_0 was systematically varied by utilizing different wall thicknesses for the chord. To explore the effect of different brace sections on parameter β, various brace configurations were considered. Across all 33 simulations performed, the brace underwent axial compression until reaching its ultimate joint capacity, as detailed in Table 5.3. This table also presents the variations in parameter β (ranging from 0.32 to 0.8), parameter γ (ranging from 7.8 to 19.8), and the brace's eccentricity (ranging from 0.0 mm to 63.0 mm).

The brace eccentricity was defined as the gap between the hypothetical intersection point of the longitudinal axes of the chord and the brace, calculated as $0.5b_0 - (r_{ext} + a_w + 0.5b_1)$. Parameter β was determined using the conventional method, excluding the legs of the fillet weld from the definition. The range of geometrical parameters β and γ specified in Table 5.3 was thoughtfully chosen to encompass the most significant behavioural characteristics of T-joints. Specifically, small values of γ result in a negligible membrane effect, while large values of β significantly enhance the resistance derived from pure bending mechanisms. It's important to acknowledge that other phenomena also need to be considered and accounted for in this context.

Table 5.3 The scope of numerical experiments

Specimen label	Chord				Brace							
	RHS	h_0, [mm]	b_0, [mm]	t_0, [mm]	RHS	h_1, [mm]	b_1, [mm]	t_1, [mm]	β, [-]	γ, [-]	e, [mm]	P_{ult}, [kN]
CH6_B80-10	350×250×6.3	350	250	6.3	120×80×10	120	80	10.0	0.32	19.8	63.0	172.28
CH8_B80-10	350×250×8	350	250	8.0		120	80	10.0	0.32	15.6	63.0	289.79
CH10_B80-10	350×250×10	350	250	10.0		120	80	10.0	0.32	12.5	60.0	391.58
CH12_B80-10	350×250×12.5	350	250	12.5		120	80	10.0	0.32	10.0	56.2	536.02
CH14_B80-10	350×250×14.2	350	250	14.2		120	80	10.0	0.32	8.8	53.7	641.18
CH16_B80-10	350×250×16	350	250	16.0		120	80	10.0	0.32	7.8	51.0	762.22
CH6_B100-10	350×250×6.3	350	250	6.3	150×100×10	150	100	10.0	0.4	19.8	53.0	197.05
CH8_B100-10	350×250×8	350	250	8.0		150	100	10.0	0.4	15.6	53.0	319.87
CH10_B100-10	350×250×10	350	250	10.0		150	100	10.0	0.4	12.5	50.0	447.93
CH12_B100-10	350×250×12.5	350	250	12.5		150	100	10.0	0.4	10.0	46.2	608.54
CH14_B100-10	350×250×14.2	350	250	14.2		150	100	10.0	0.4	8.8	43.7	724.60
CH16_B100-10	350×250×16	350	250	16.0		150	100	10.0	0.4	7.8	41.0	868.98
CH6_B120-12.5	350×250×6.3	350	250	6.3	200×120×12.5	200	120	12.5	0.48	19.8	43.0	229.80
CH8_B120-12.5	350×250×8	350	250	8.0		200	120	12.5	0.48	15.6	43.0	381.53
CH10_B120-12.5	350×250×10	350	250	10.0		200	120	12.5	0.48	12.5	40.0	563.68
CH12_B120-12.5	350×250×12.5	350	250	12.5		200	120	12.5	0.48	10.0	36.2	752.84
CH14_B120-12.5	350×250×14.2	350	250	14.2		200	120	12.5	0.48	8.8	33.7	907.42
CH16_B120-12.5	350×250×16	350	250	16.0		200	120	12.5	0.48	7.8	31.0	1092.12
CH6_B150-12.5	350×250×6.3	350	250	6.3	250×150×12.5	250	150	12.5	0.6	19.8	28.0	278.06
CH8_B150-12.5	350×250×8	350	250	8.0		250	150	12.5	0.6	15.6	28.0	450.18
CH10_B150-12.5	350×250×10	350	250	10.0		250	150	12.5	0.6	12.5	25.0	665.56
CH12_B150-12.5	350×250×12.5	350	250	12.5		250	150	12.5	0.6	10.0	21.2	928.94
CH14_B150-12.5	350×250×14.2	350	250	14.2		250	150	12.5	0.6	8.8	18.7	1141.75
CH16_B150-12.5	350×250×16	350	250	16.0		250	150	12.5	0.6	7.8	16.0	1370.94
CH6_B180-12.5	350×250×6.3	350	250	6.3	260×180×12.5	260	180	12.5	0.72	19.8	13.0	327.33
CH8_B180-12.5	350×250×8	350	250	8.0		260	180	12.5	0.72	15.6	13.0	536.51
CH10_B180-12.5	350×250×10	350	250	10.0		260	180	12.5	0.72	12.5	10.0	794.25
CH12_B180-12.5	350×250×12.5	350	250	12.5		260	180	12.5	0.72	10.0	6.2	1164.09
CH14_B180-12.5	350×250×14.2	350	250	14.2		260	180	12.5	0.72	8.8	3.7	1454.14
CH16_B180-12.5	350×250×16	350	250	16.0		260	180	12.5	0.72	7.8	1.0	1774.19
CH6_B200-12.5	350×250×6.3	350	250	6.3	300×200×12.5	300	200	12.5	0.8	19.8	3.0	471.43
CH8_B200-12.5	350×250×8	350	250	8.0		300	200	12.5	0.8	15.6	3.0	744.56
CH10_B200-12.5	350×250×10	350	250	10.0		300	200	12.5	0.8	12.5	0.0	1071.50

5.4 NUMERICAL ANALYSIS RESULTS

5.4.1 Failure modes and behaviour

A comprehensive analysis of load-displacement curves reveals consistent propagation features, characterized by the absence of extremes or abrupt changes. This consistent behaviour is indicative of a shared failure mode across all types of offset joints. Notably, unlike T-joints created without eccentricity, offset joints exhibit intricate failure modes. These modes are defined by a simultaneous deformation pattern of the chord web and indentation of the chord face, even in models featuring low β values.

The degree of loading on opposing chord webs is notably influenced by the magnitude of offset eccentricity. Larger eccentricities result in more pronounced differences in loading levels between opposite webs. Furthermore, in models with higher β values, beginning from specimens with $\beta = 0.6$, localized brace buckling was observed on the outer side of the brace under high loading conditions.

The intricate interplay of these combined failure modes in the deformation of offset joints warrants meticulous examination. These modes of failure serve as additional factors prompting a thorough reconsideration and potential adjustment of the deformation criteria initially developed for general T-joints. Such considerations are especially pertinent when adapting, modifying, or possibly even revising the deformation criteria to accommodate the complexities introduced by offset joints.

Numerical simulations performed for the models with different types of offset but with equal geometrical parameters of the braces and chords reveal the difference in behaviour of fully offset RHS T-connections and SCE RHS T-type connections as it is demonstrated by the Figure 5.7. The load-displacement diagrams obtained for the SCE RHS T-type connections are mostly characterized by a typical diagram of combined failure mode according to the classification given in [52], in which the chord face and the chord web reach their strengths almost simultaneously, and their resistance to the load can be defined by their limit strains prior to yielding. Whereas, the load-displacement diagram of the fully offset connection studied by Bu et al. in [11] (Figure 5.7, *a*) demonstrates a pattern of pure web crippling which is usually observed in tests [8] and [94], or numerical simulations [165]. These facts explicitly prove the complex nature of deformation of the SCE RHS T-type connections and the correctness of the adopted assumptions for the developed analytical model.

a)

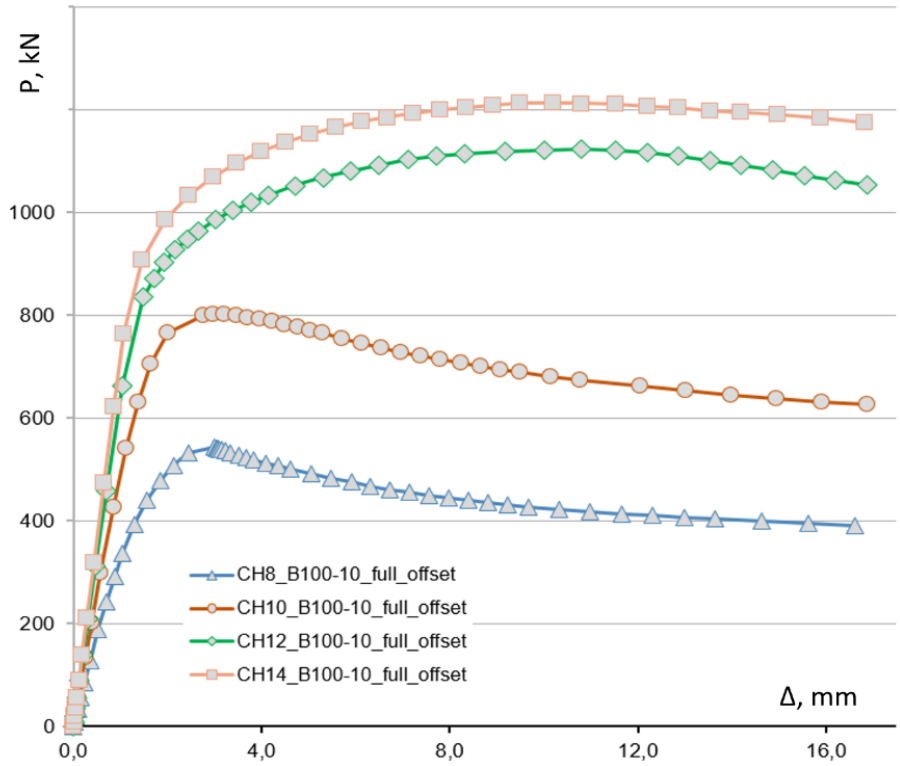

b)

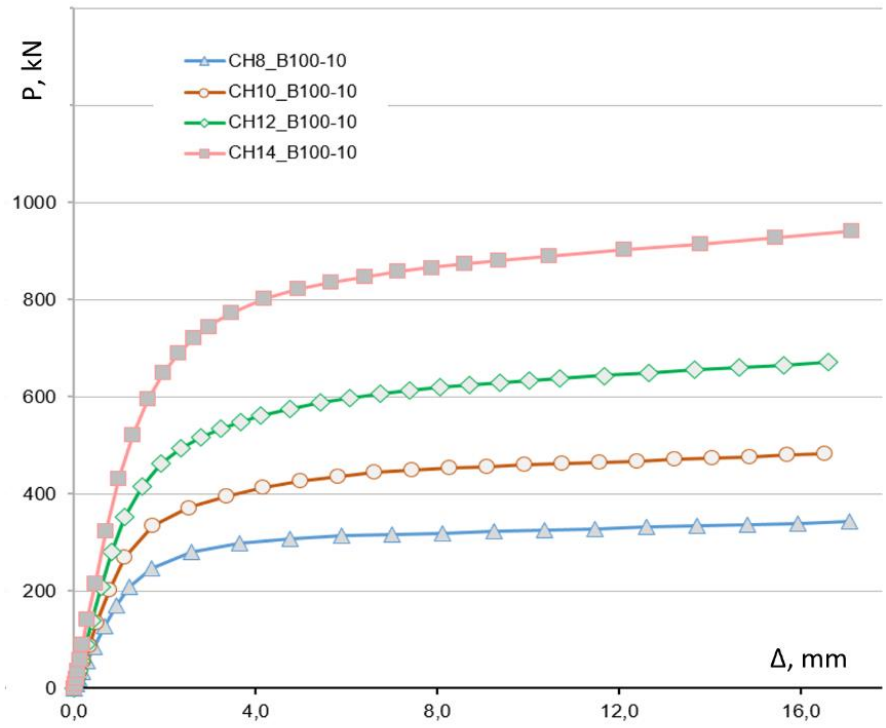

Figure 5.7 Comparing load-displacement diagrams for fully offset connection (a) and stepped connection with eccentricity (b)

5.4.2 Ultimate resistance

The numerical outcomes for resistance (P_{ult}) are showcased in the final column of Table 5.3. The adoption of the $3\%b_0$ deformation criterion, following Lu et al. [76], guided the assessment. Based on this limit, a deformation criterion was employed according to Zhao [160]:

Chord face failure

$$\beta < 0.8. \quad \text{If } P_{3\%}/P_{1\%} \leq 1.5, \quad P_{ult} = P_{3\%}. \qquad (12)$$
$$\text{If } P_{3\%}/P_{1\%} > 1.5, \quad P_{ult} = 1.5P_{1\%}.$$

Web buckling failure

$$\beta \geq 0.8. \quad \text{If } \Delta_{\%} \leq 3\%b_0, \quad P_{ult} = P_{max}. \qquad (13)$$
$$\text{If } \Delta_{\%} > 3\%b_0, \quad P_{ult} = P_{3\%b_0}.$$

Overall, the patterns depicting the relationships between key geometrical parameters and ultimate loads, as established for joints without offset (as presented in Matos et al. [82]), are replicated in the results of the current numerical investigation.

Graphical representation of these outcomes (refer to Figure 5.8) unmistakably reveals that the joint's resistance escalates alongside increased wall thickness (equivalently, a decrease in the parameter γ), regardless of the specific constellation of diagrams centred around distinct β values. Furthermore, resistance exhibits a robust correlation with the brace width, rising in tandem with an augmentation of the parameter β, irrespective of the chord thickness.

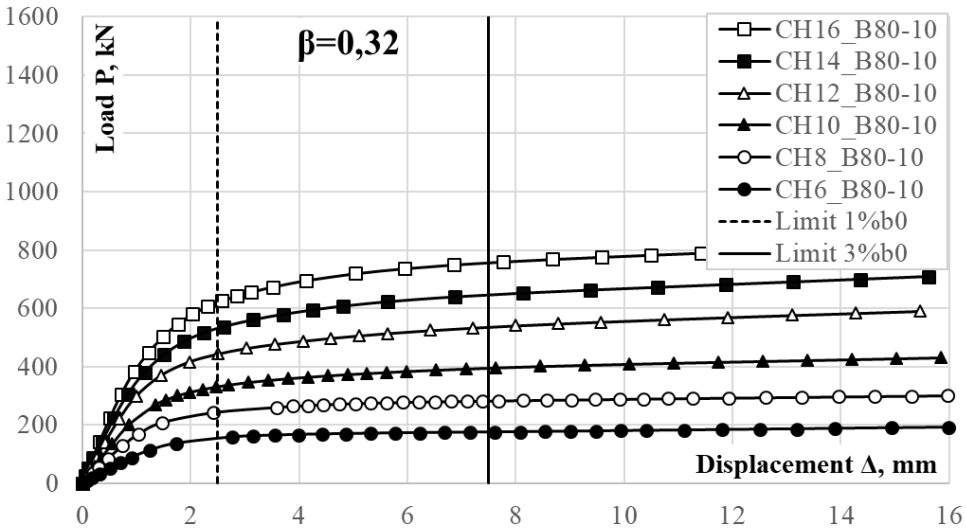

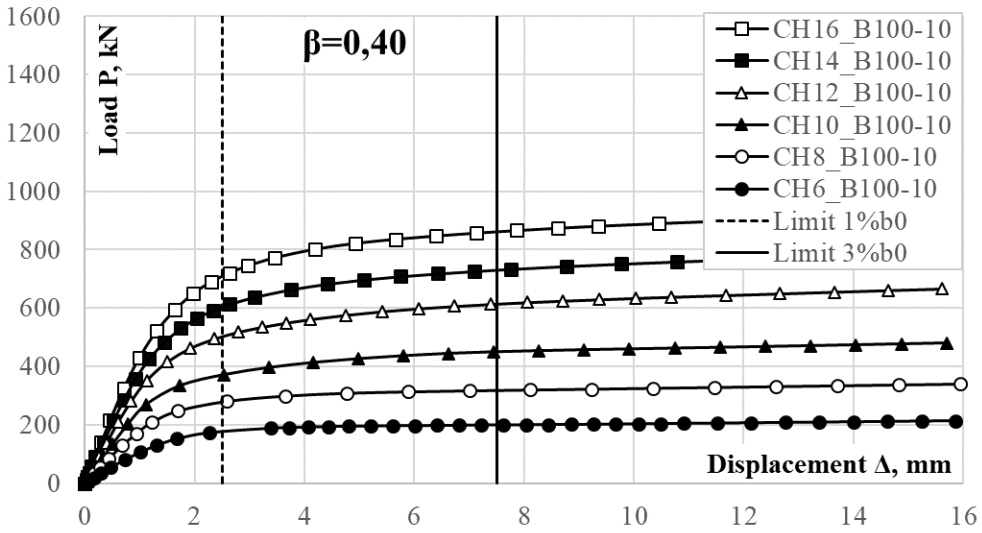
β=0,40
Load P, kN
Displacement Δ, mm
CH16_B100-10
CH14_B100-10
CH12_B100-10
CH10_B100-10
CH8_B100-10
CH6_B100-10
Limit 1%b0
Limit 3%b0

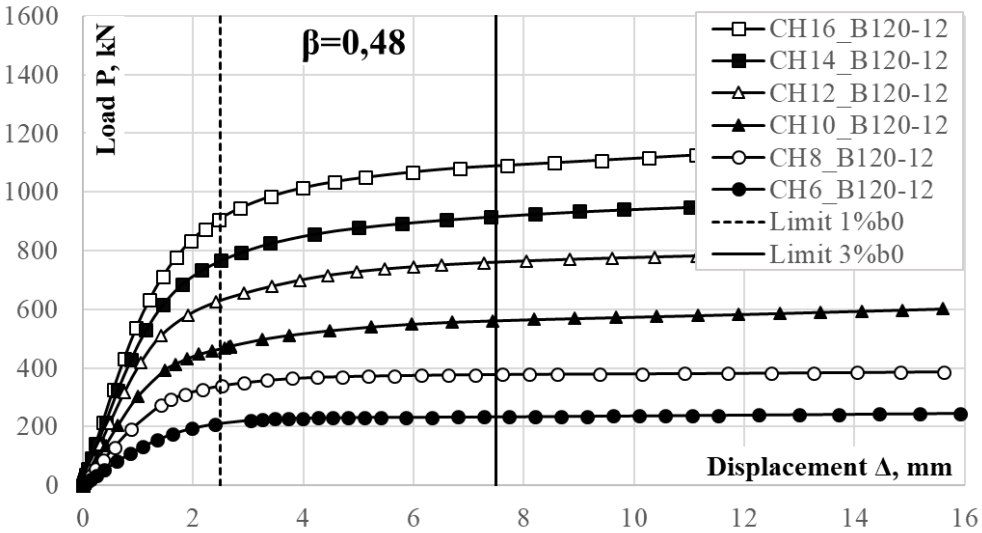
β=0,48
Load P, kN
Displacement Δ, mm
CH16_B120-12
CH14_B120-12
CH12_B120-12
CH10_B120-12
CH8_B120-12
CH6_B120-12
Limit 1%b0
Limit 3%b0

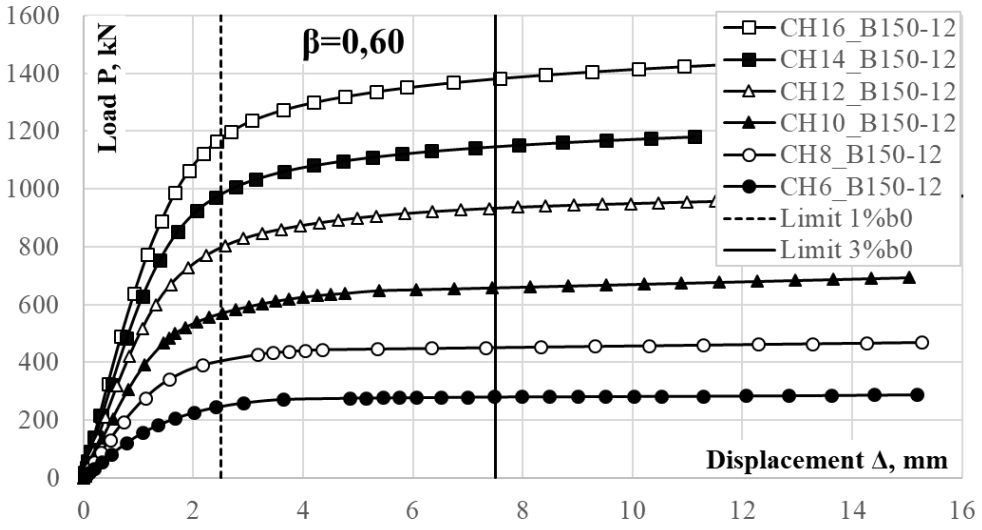
β=0,60
Load P, kN
Displacement Δ, mm
CH16_B150-12
CH14_B150-12
CH12_B150-12
CH10_B150-12
CH8_B150-12
CH6_B150-12
Limit 1%b0
Limit 3%b0

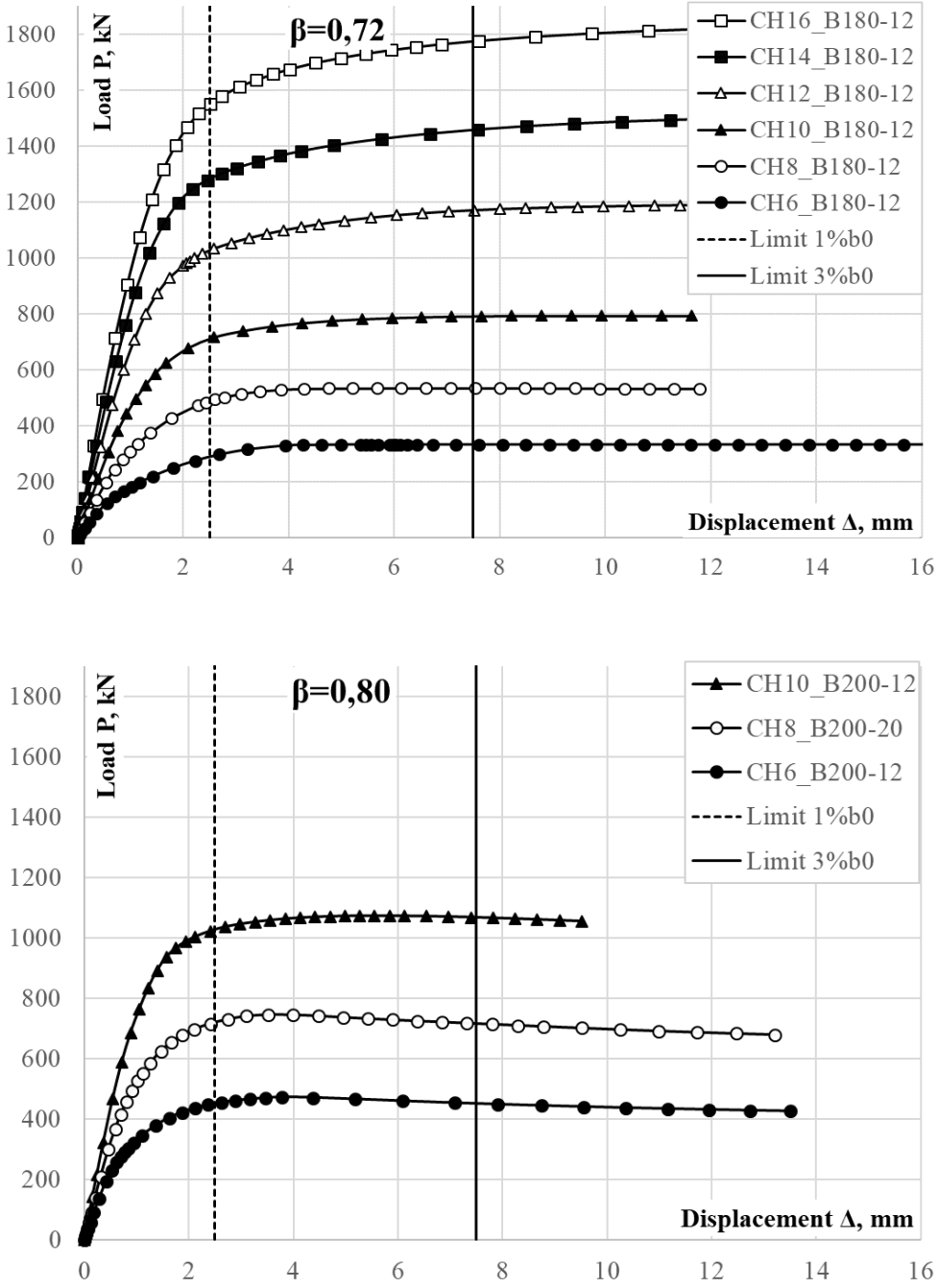

Figure 5.8 Load-displacement curves collected around individual values of width-to-width ratios β

While many load-deformation curves lack conspicuous peak loads, the adoption of the $3\%b_0$ deformation criterion has been debated and applied to estimate the ultimate load. However, it should be noted that this criterion does not account for the complex failure modes uncovered in simulations across all types of offset joints.

The interplay between the applied load's eccentricity and the adopted ultimate limit force is illustrated in Figure 5.9. The patterns delineating changes in resistance relative to eccentricities

on the diagrams cast doubt on the suitability of utilizing the criterion established by Lu et al. [76] to evaluate resistance for offset T-joints. The pronounced correlation between load eccentricities and the joints' geometrical characteristics (parameters β and γ), vividly depicted in Figure 5.9, underscores the significance of this correlation, particularly when considering data collected through the width-to-thickness ratio.

5.4.3 Concluding Remarks

The results from finite element analyses of steel tubular T-joints with offset, encompassing a wide range of geometrical parameters, have been meticulously presented and scrutinized. The primary conclusions drawn from this study can be summarized as follows.

Drawing from the conducted numerical investigations and insights gleaned from existing literature, it is crucial to emphasize that the $3\%b_0$ criterion falls short in accommodating the distinctive combined failure modes witnessed in offset joints. Consequently, for the design of RHS welded joints with offset, it is advisable to seek alternative approaches beyond the propositions set forth by Lu et al. [76]. One possible alternative is to consider the load corresponding to the 5% maximum principal strain, as suggested by Annex C of EN 1993-1-5:2006 (CEN 2006).

The numerical results obtained from simulations exhibited noteworthy agreement with the experimental outcomes of RHS tubular T-joints conducted for the validation procedure.

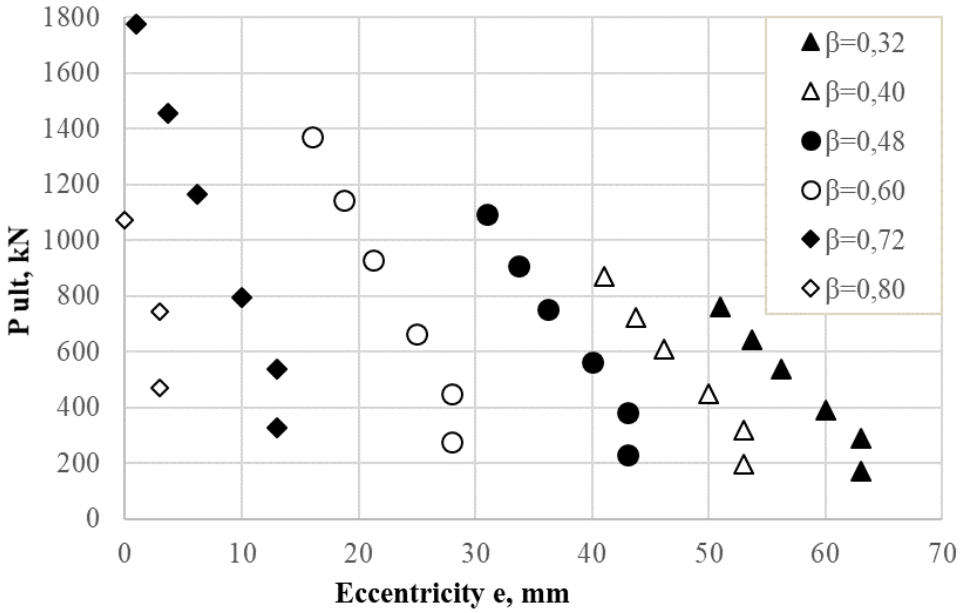

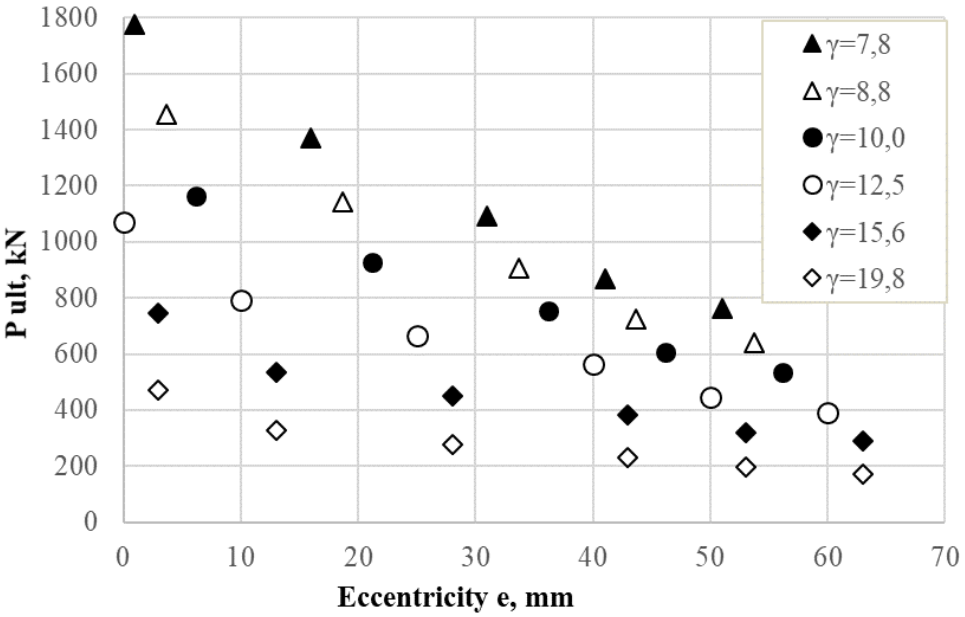

Figure 5.9 Impact of Eccentricity on the Load at $3\%b_0$

CHAPTER 6:
ANALYTICAL RESISTANCE OF SCE RHS JOINTS SUBJECTED TO CONCENTRATED FORCE

The chapter encompasses the creation of a plastic mechanism model designed for laterally offset joints featuring different brace-to-chord eccentricities. It further includes a detailed comparison of analytical models aimed at assessing the strength of laterally offset T-connections. Additionally, a step-by-step procedure is outlined to validate the proposed model. This validation process involves numerical simulations conducted by Kalmykova and Wald [49] [50] along with those conducted by Bu, Wei, and Packer [12].

6.1 DESIGNING T-CONNECTIONS USING PLASTIC MECHANISM MODELS

Usually, the design of welded RHS connections involves an analysis of potential failure modes, followed by estimating the limit state for each mode individually. Initially, Kato and Nishiyama [52] examined the primary five failure modes for RHS T-connections subjected to concentrated force, a classification later summarized in CIDECT [32]. Their findings highlighted the strong dependence of the failure mode type on the width-to-width ratio β. This ratio dictates the nature of $P - \Delta$ (force-displacement) diagrams and the distribution of regions with concentrated plastic strains across the connection's structure. It was established that, with the exception of modes where $\beta \approx 1.0$, characterized by the local yielding of the chord web without affecting the chord face, most failure modes exhibit a combined mechanism involving plastic failure of the chord face alongside web crippling.

A quick overview of existing design methods for RHS connections under axial force reveals that many are rooted in yield line mechanism analyses, where the patterns of yield lines mirror the actual configurations of the connection's ultimate deformations. Additionally, [141] highlights that the yield line approach provides an upper-bound solution for the yield load. Consequently, a wide range of mechanisms should theoretically be examined to find the lowest acceptable value as the failure load. Nevertheless, various studies have shown that simplified yield line patterns yield strengths up to 10% higher than more intricate patterns with yield fans or those featuring numerous yielding lines. Interestingly, for classic stepped T-connections with the brace aligned along the chord's centreline and placed in the side walls of the chord, the yield load capacity experiences only minor influence from the yield line pattern and the level of chord loading. The calculation method involves equating the work performed by the external force with the work carried out by the plastic hinge system.

To predict the plastic resistance of T-connections under the influence of concentrated forces, numerous plastic mechanism models have been developed through the yield line method and enhanced by various researchers. The most renowned and notable works [52], [155], [48], [156]

and [26] were crafted in the late 20th century and form the foundation of modern design standards and guidelines [2], [6], [15], [16], [33] and [34]. What distinguishes these models primarily lies in their assumptions concerning the disposition of plastic hinges along the chord's cross-section, which coincides with the vertical plane traversing the axis of symmetry of the brace.

An extensive comparative analysis of the predictive models and derived formulas outlined in [52], [155], [48], [156] and [26] was conducted by Feng and Young [44], utilizing results from tests conducted on T-connections crafted from stainless steel. It became evident that accurately accounting for the arrangement of plastic hinges significantly impacts the resultant values of predicted capacity. This examination revealed that for cold-formed stainless steel RHS T- and X-connections, the average ratios of failure load to design strength ranged from 0.59 to 0.92, with a maximum coefficient of variation of 0.366. Based on these parameters, it can be inferred that models adopted for estimating the combined resistance of T-connections, without differentiating between the resistance of the chord face and chord walls, may possess limitations and shortcomings.

It's worth noting that, except for the model formulated by Zhao and Hancock [157], all other models failed to consider the behaviour of plastic hinges formed at the chord webs. However, substantial plastic deformations at the chord webs were often observed almost simultaneously with the yielding of the chord flange during tests outlined in [8]. This observation underscores the necessity of incorporating into design procedures an assessment of the concurrent resistance of the chord face and chord webs.

In studies conducted by Beque and Cheng [8] and [18], as well as by Nogueira et al [94], the behaviour of chord webs has undergone thorough examination. In these works, novel design methodologies have been formulated for RHS X-connections that fail due to chord web buckling. These methodologies have been rigorously validated through a series of tests and numerical simulations. The proposed analytical approaches, which estimate chord web buckling while accounting for refined assumptions, provide satisfactory solutions for fully welded T-connections with $\beta = 1.0$. However, these studies do not present a comprehensive solution to the design challenges faced by RHS connections exposed to combined failures, such as those with values of $\beta \approx 0.8$ or SCE RHS connections [8].

To date, there have been few published works on the topic of offset connection design. Apart from the pioneering experimental investigation by Dawe et al. [25] concerning laterally offset T- and N-connections with preloaded chords, few works have explored the behaviour of offset connections. Noteworthy contributions to this area of study have been made by Bu, Wei, and Packer [11], as well as Wei and Packer [146]. These studies have involved comprehensive research endeavours aimed at establishing a robust analytical model to estimate the resistance of offset connections. The proposed models were subjected to validation through a combination of numerical simulations and experimental tests. However, it's essential to acknowledge that the

foundational assumptions underpinning the primary design equation in [11] and [146], assuming the absence of a web resistance component in the virtual works equation, may have inherent limitations or potential inaccuracies.

In the pursuit of expanding knowledge about the design of offset connections, the research is thought to conduct a comparative analysis of results obtained from various codes, calculation techniques, and analytical models, including the model put forth by [11]. In conclusion, it was deduced that the analytical model developed to ascertain the resistance of connections with matching branch and chord sidewalls, as explored in [11] and [146], is not applicable to SCE RHS connections. Discrepancies in the design strength of SCE RHS connections, derived from numerical simulations and calculated using the analytical equation presented in [11], were substantial, ranging from 2.9% to 35.3%. Furthermore, there was no consistent trend in the fluctuation of design strength. An additional crucial finding relates to the suitability of criteria initially formulated for stepped (co-axial) welded RHS connections in extrapolating the ultimate resistance of offset RHS T-connections. The utilization of the methodologies outlined in design codes and guidelines has been demonstrated to lead to a substantial underestimation of the true design strength of SCE RHS connections.

Given the preceding analysis, it can be concluded that there is currently no universal analytical model that adequately evaluates the resistance of SCE RHS connections with different types of branch offsets from the connection central plane. Consequently, the primary goal is to formulate and validate suitable physical relationships that facilitate numerical estimation of the resistance for T-connections across a wide spectrum of eccentricities and various types of branch offsets.

6.2 ANALYTICAL MODEL FOR DESIGNING SCE RHS X-TYPE CONNECTIONS

6.2.1 Zhao and Hancock's Membrane Mechanism Model

Plastic mechanism model developed by Zhao and Hancock [157] was used as the basis for developing the present model to calculate the design strength of the SCE RHS connections. The aforementioned plastic mechanism models did not consider the plastic hinges at the chord webs, which are commonly observed during the tests in the ultimate limit state. Typical graphs of load versus flange deflection and web deflection demonstrate that the flange and web yield almost simultaneously. The model of Zhao and Hancock [157] consists of a set of yield lines in the chord webs and flanges with their own rotation capacities, capable of accounting for the membrane force in the chord flange and the strain hardening of the material. This model can be used to predict the yield load, post-yield behaviour, and ultimate load of RHS T-connections with tubular sections subjected to concentrated force.

The design strength of connections based on the abovementioned model can be determined using the design equation obtained from virtual work principle. For more details, go to the Chapter 2.4.7.

6.2.2 Membrane mechanism model for SCE RHS connections

Based on the membrane mechanism model [157], the strength of SCE RHS T-type connections for RHS tubular members can also be determined using the pattern of yield lines, with a slight modification.

The current model is visually represented in Figure 6.1 and is further detailed in the summary provided in Table 6.1. For a comprehensive understanding of the model's geometry, please refer to the derivations and calculations presented in the Annex A.

In the developed model, the web deformation Δ_w is presumed to be equal to $\beta\Delta$. This assumption draws from observations derived from numerical simulations and tests conducted by the authors in [50].

Within the scope of this study, the model size J is computed for two scenarios: one that considers the membrane effect in the chord flange and another that disregards it. As indicated in the comparative analysis conducted for model calibration, incorporating membrane forces following Mouty's membrane model [87], [88] leads to conservative solutions when estimating the design strength of offset T-connections characterized by low values of β (as indicated in column 6 of Table 6.3). The complex nature of the membrane force distribution around the brace of offset connections serves as an obvious reason behind this phenomenon. Furthermore, the research of Davies [26] has demonstrated that membrane effects in the transverse direction within stepped RHS X-type connections can be negligible. However, this assertion may introduce some uncertainty and result in incorrect solutions for offset connections.

Regarding the case where the membrane effect is taken into account, the model size J is determined by optimizing the function $P(J)$.

$$\frac{dP}{dJ} = \frac{dP_m}{dJ} + \sum_{i=3,4,7}^{13} k_i \frac{\Delta P_i}{\Delta J} = 0, \tag{14}$$

and can be calculated by solving an equation

$$aJ^2 + bJ - c = 0, \tag{15}$$

where

$$a = 1 + n_1 k + \frac{2e_1}{1 - e_1}, \tag{16}$$

$$b = 2n_1(b_0 + b_1)\sqrt{\left(1 + e_y\right)^2 - 1}\,, \tag{17}$$

$$c = \frac{e_2^2 h_0^2 n_1}{k} + e_1 h_0^2 + n_1 h_0 \beta. \tag{18}$$

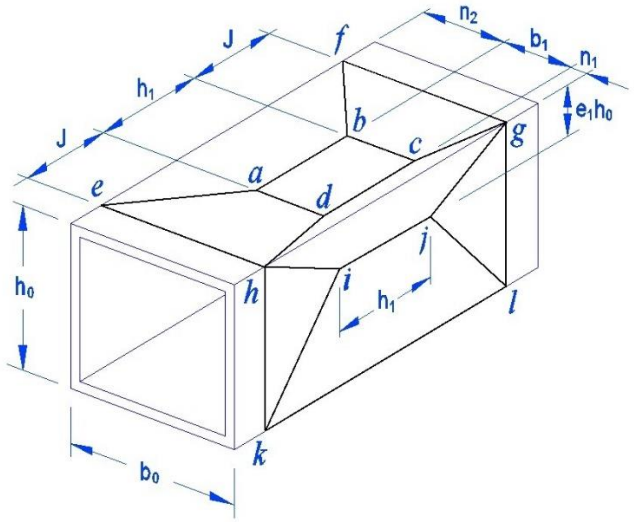

a) General view - brace side

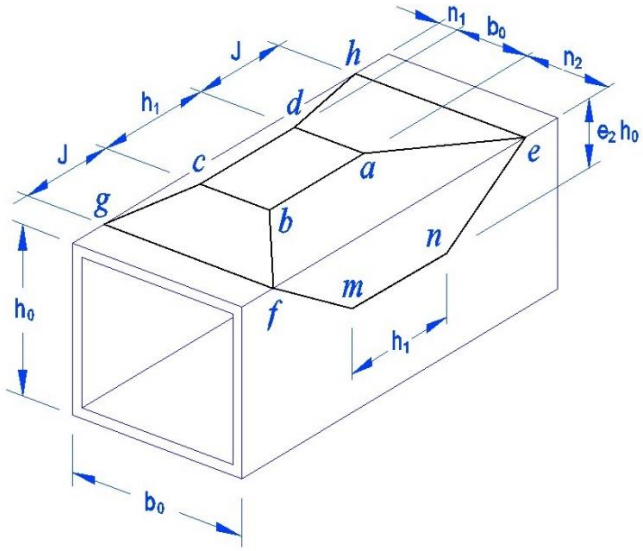

b) General view – opposite-to-brace side

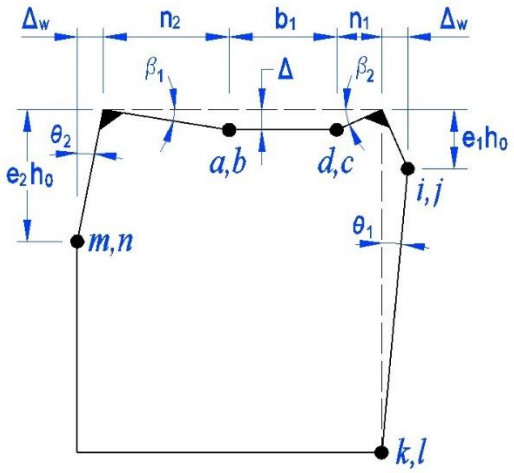

c) Cross sections – transverse

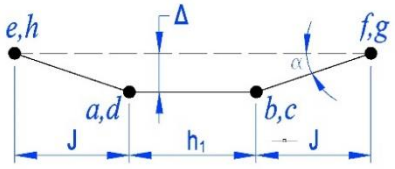

d) Cross sections – longitudinal

Figure 6.1 Proposed yield line model for SCE RHS connections

When disregarding the membrane effect, the expression for the minimum condition of the function $P(J)$ is reformulated as follows:

$$\frac{dP}{dJ} = \sum_{i=1}^{13} k_i \frac{\Delta P_i}{\Delta J} = 0. \tag{19}$$

The model size can be calculated as follows:

$$J = \sqrt{\frac{b_1 + b_0 + n_1 + n_2 + \frac{e_1^2 h_0^2}{n_1} + \frac{e_1 h_0^2 (1 - e_1)}{n_1} + \beta h_0 - \beta e_2 h_0}{\frac{2}{n_1} + \frac{1}{n_2} + \frac{2e_1}{n_1(1 - e_1)} + \frac{\beta}{e_2 h_0}}} \tag{20}$$

The design strength of SCE RHS connections can be determined using the design equation obtained from virtual work principle, which is summarized as follows:

$$N_{Rd} = \sum_{i=1}^{13} k_i P_i. \tag{21}$$

The contributions to the overall yield load stemming from each plastic hinge of types 1 to 13 can be found from the equations documented in column 7 of Table 6.1.

The predicted yield load derived from the developed model can be interpreted as the design strength or resistance of the SCE RHS connections. This yield load is then compared with the results of numerical simulations, as outlined below in Table 6.3. Additionally, a comparison is made between the predicted design strength, the values obtained using the design equations proposed in [11] for offset X-type connections, and in [15], [34], [162] for common stepped connections.

Table 6.1 The components of Eq. (21) for the adopted yield line mechanism

Hinge type No.	Number of hinges, k_i		Hinge nomenclature	Hinge rotation angle	Increment of angle δ (angle)	Hinge length, l_i	Virtual work, δW_i	Derivatives dP_i/dJ
1	2a	2b	3	4	5	6	7	8
1	2		ad, bc	α	$\frac{1}{J}\delta\Delta$	b_1	$M_p\frac{b_1}{J}\delta\Delta$	$-M_p\frac{b_1}{J^2}$
2	2		eh, fg	α	$\frac{1}{J}\delta\Delta$	b_0	$M_p\frac{b_0}{J}\delta\Delta$	$-M_p\frac{b_0}{J^2}$
3	1		ab	β_1	$\frac{1}{n_1}\delta\Delta$	h_1	$M_p\frac{h_1}{n_1}\delta\Delta$	0
4	1		dc	β_2	$\frac{1}{n_2}\delta\Delta$	h_1	$M_p\frac{h_1}{n_2}\delta\Delta$	0
5	2		ae, bf	ψ_1	$\frac{\sqrt{n_1^2+J^2}}{n_1 J}\delta\Delta$	$\sqrt{n_1^2+J^2}$	$M_p\frac{n_1^2+J^2}{n_1 J}\delta\Delta$	$M_p\left[\frac{1}{n_1}-\frac{n_1}{J^2}\right]$
6	2		dh, cg	ψ_2	$\frac{\sqrt{n_2^2+J^2}}{n_2 J}\delta\Delta$	$\sqrt{n_2^2+J^2}$	$M_p\frac{n_2^2+J^2}{n_2 J}\delta\Delta$	$M_p\left[\frac{1}{n_2}-\frac{n_2}{J^2}\right]$
7	1		ij	$\beta_2+\theta_1$	$\frac{n_1(1-e_1)+n_2e_1}{n_1n_2(1-e_1)}\delta\Delta$	h_1	$M_p h_1\left[\frac{n_1(1-e_1)+n_2e_1}{n_1n_2(1-e_1)}\right]\delta\Delta$	0
8	1		mn	θ_2	$\frac{e_1}{e_2n_1}\delta\Delta$	h_1	$M_p\frac{e_1h_1}{e_2n_1}\delta\Delta$	0
9	2		gj, hi	ψ_3	$\frac{\sqrt{e_1^2h_0^2+J^2}}{n_1 J}\delta\Delta$	$\sqrt{e_1^2h_0^2+J^2}$	$M_p\frac{e_1^2h_0^2+J^2}{n_1 J}\delta\Delta$	$M_p\left[\frac{1}{n_1}-\frac{e_1^2h_0^2}{n_1J^2}\right]$
10	2		ik, jl	ψ_5	$\frac{\sqrt{(1-e_1)^2h_0^2+J^2}}{n_1 J}\frac{e_1}{(1-e_1)}\delta\Delta$	$\sqrt{(1-e_1)^2h_0^2+J^2}$	$M_p\frac{(1-e_1)^2h_0^2+J^2}{n_1 J}\frac{e_1}{(1-e_1)}\delta\Delta$	$M_p\frac{e_1}{(1-e_1)}\left[\frac{1}{n_1}-\frac{(1-e_1)^2h_0^2}{n_1J^2}\right]$

Hinge type No.	Number of hinges, k_i		Hinge nomenclature	Hinge rotation angle	Increment of angle δ (angle)	Hinge length, l_i	Virtual work, δW_i	Derivatives dP_i/dJ
1	2a	2b	3	4	5	6	7	8
11	1		kl	θ_1	$\frac{e_1}{n_1(1-e_1)}\delta\Delta$	$2J+h_1$	$M_p\frac{e_1(2J+h_1)}{n_1(1-e_1)}\delta\Delta$	$M_p\frac{2e_1}{n_1(1-e_1)}$
12	2		fm, ne	ψ_6	$\frac{\beta\sqrt{e_2^2h_0^2+J^2}}{e_2h_0J}$	$\sqrt{e_2^2h_0^2+J^2}$	$M_p\left[\frac{\beta e_2h_0}{J}+\frac{\beta J}{e_2h_0}\right]\delta\Delta$	$M_p\left[\beta\left(\frac{1}{e_2h_0}+\frac{e_2h_0}{J^2}\right)\right]$
13	2		hk, gl	ψ_4	$\frac{\beta}{J}\delta\Delta$	h_0	$M_p\frac{\beta h_0}{J}\delta\Delta$	$-M_p\frac{\beta h_0}{J^2}$

6.3 EVALUATING DESIGN STRENGTH BY THE PROPOSED PLASTIC MECHANISM MODELS

The strengths of SCE RHS T-type connections, obtained using equations (19) and (20), were subjected to a comparative analysis against results from numerical simulations. Additionally, they were compared to the design strengths calculated through existing design equations presented in building code [15] and contemporary studies focused on the design of offset connections [11], [157]. This comparison encompassed various scenarios, including the plasticization of the chord face and sidewall failure limit states as per EN 1993-1-8. Moreover, the comparison involved average strengths acquired for the chord face and sidewall, the combined failure mode proposed by Bu et al. in [11], and the original model developed by Zhao and Hancock in [157] for stepped connections without brace shift, utilizing Eq. (11) and data from Table 2.1. The findings of this comparative analysis are detailed in Table 6.2.

6.3.1 Model for chord face plasticization limit state

The design methodology in compliance with EN 1993-1-8:2005 [15] is employed to forecast the strength of conventional stepped welded T-type connections among RHS members. The geometry of the connections falls within the scope of validity outlined in Eurocode.

To circumvent local brace failure, the brace thickness was chosen judiciously. Consequently, the predominant failure mode is Chord face failure for cases where β≤0.85, as specified in Table 9.14 of [15]:

$$N_{1,Rd} = C_f \frac{f_{y0} t_0^2}{\sin\theta}\left(\frac{2h_1}{b_0 \sin\theta} + 4\sqrt{1-\beta}\right)\frac{Q_f}{\gamma_{M5}}, \tag{22}$$

where C_f is a material factor, θ_1 is an included angle between brace member and the chord, and Q_f is a chord stress factor.

As can be seen from Table 2.1, even though the coefficient of variation is low, the use of Eq. (22) is not suitable for evaluating the load-bearing capacity of T-connections. The mean value of the design strength is very high, indicating that the use of the chord plasticisation limit state criterion of the stepped connections to evaluate the resistance of the SCE T-connections leads to a significant under-estimation of the design strength obtained by the proposed analytical model by more than 1.5 times.

6.3.2 Model for chord sidewall failure limit state

Connections where the branch and chord members possess similar or larger widths, denoted by $\beta > 0.8$, are recognized as full-width RHS connections. These connections are also referred to as matched connections. The failure of these matched connections is primarily governed by the chord webs' resistance against crippling. As outlined in [15], this failure mode can be determined through the following equation:

$$N_{2,Rd} = \frac{2\chi f_{y0} t_0}{\sin\theta}\left(\frac{h_1}{\sin\theta} + 5t_0\right). \tag{23}$$

In the compressed branch, the parameter χ is to be computed as per [15], employing the relevant buckling curve and treating the chord sidewalls as columns. The subsequent equations, namely Eqs. (24) to (26), furnish the essential elements required for the calculation of $N_{2,Rd}$:

$$\chi = \frac{1}{\phi + \sqrt{\phi^2 - \lambda^2}} \leq 1.0; \quad \phi = 0.5[1 + \alpha(\lambda - 0.2) + \lambda^2], \tag{24}$$

$$F_e = \frac{\pi^2 E}{(KL_c/r)^2}, \tag{25}$$

$$\lambda = \sqrt{\frac{f_{y0}}{F_e}}, \tag{26}$$

Here, L_c represents the length of the sidewall column, calculated in accordance with [15] using the formula $(h_0 - 2t_0)$. Additionally, r is the radius of gyration of the rectangular section of the sidewall column, computed as $r = \frac{t_0}{\sqrt{12}}$. In this context, K stands for the effective length factor (assumed as 1.0 for the current comparison), and E denotes the modulus of elasticity (205 000 MPa).

The values of $N_{2,Rd}$ for the SCE RHS T-type connections can be found in Table 6.2. These values, as presented in the table, are determined by applying Eq. (23) to a single branch and subsequently multiplied by a factor of two. Similar to Eq. (22), Eq. (23) tends to underestimate the resistance of T-type SCE RHS connections. Moreover, the computed values for the individual sidewall exhibit a notable coefficient of variation (> 20), making them unsuitable for indicating the bearing capacity of connections with brace offset.

6.3.3 Average resistance for equal stepped connection

The presented model is established on the fundamental assumption of concurrent deformation processes taking place in both the chord face and sidewalls. Hence, it is pertinent to compute the average value of $N_{3,Rd}$ lying between the resistances dictated by the limit states of chord face

plasticization and sidewall failure. This estimation is intended for non-offset connections featuring comparable brace and chord geometries.

Individual calculations of design strengths for the chord face and sidewall substantially underestimate the design strength derived from the proposed analytical model. To ascertain the average resistance, the formulas for stepped connections with $\beta < 0.8$ (Eq. (22)) and full-width connections ($\beta \geq 0.8$) sharing the same bearing length along the chord (Eqs. (23) to (26)) are employed. Values obtained from Eq. (22) are combined with those from Eq. (23) for two branches, and the sum is divided by two.

This approach yields the mean value of the design strength, demonstrating the model's utility for evaluating the bearing capacity of T-type SCE RHS connections. Nevertheless, the relatively substantial coefficient of variation imposes limitations on the practical applicability of this approach.

6.3.4 Bu-Wei-Packer approach

Welded offset RHS connections were recently studied by Kalmykova and Wald [50] and Wei and Packer [146]. Later, Bu, Wei and Packer completed their studies by their final work [11]. The publications emphasize that the design resistance of the structure and its components is defined by a combined yield-line mechanism formula. An analytical equation based on a combined yield line approach was developed in [11] to predict the strength of fully laterally offset RHS-to-RHS X-type connections with a width-to-width ratio $\beta \leq 0.925$.

$$N_{4,Rd} = \frac{f_{y0} t_0^2}{\sin\theta}\left(\frac{b_1}{b_0 \sin\theta}\left[\frac{1}{2(1-\beta)} + 2\gamma\chi\right] + 2\sqrt{2\gamma\chi + \frac{1}{1-\beta}}\right), \tag{27}$$

where γ is the chord width-to-double-thickness ratio, χ is a reduction factor applied to yield stress for sidewall ‘column’ buckling calculated by Eq. (24).

A thorough comparison between the outcomes yielded by Eq. (27) and the values computed using the proposed plastic mechanism model for T-type sections reveals that employing equations designed for fully offset RHS-to-RHS X-type connections tends to yield conservative estimations of the connection's resistance (column 10 in Table 6.2), especially for SCE RHS connections with non-aligned brace and chord sidewalls. This is particularly noticeable for specimens featuring low values of γ within the low-to-middle range of β.

To conduct a comparative assessment of the presented model against the numerical simulations executed in [11], certain improvements were applied to the developed model. The structure of the core expressions (Eqs. (14) to (20)) and the constituents outlined in Table 6.1 remained unaltered. However, the count of hinges considered was changes, as shown in column 2b of

Table 6.1. Additionally, for evaluating X-type connections, the factor $k = e_1/e_2$ was adopted within the range of 0.175 to 0.3, and the model size J is expressed as:

$$J = \sqrt{\frac{h_0^2\left[\left(\frac{e_1^2 + e_1}{2n_1}\right) - \frac{2\beta}{h_0} - \frac{b_0 + n_1}{h_0^2} - e_2 e_1\right]}{\left(\frac{2}{n_1} + \frac{e_2}{e_1} + \frac{e_1}{n_1(1 - e_1)}\right)}} \tag{28}$$

The proposed model, when applied to design fully offset RHS-to-RHS X-type connections studied by Bu, Wei, and Packer [11], [146], demonstrates satisfactory results, as depicted in Table 6.3. The table presents a comparison among the numerical simulations conducted in [11], the computational outcomes derived from the presented model (Eqs. (14) to (20)), Table 6.1), and the model formulated by Wei and Packer in [146]. In the Wei and Packer model, the parameter χ was calculated following the guidelines of EC3 [15] and the corresponding buckling curve "*c*". As a result, the values of X-connections' resistance obtained through Eq. (27) surpass those acquired from numerical simulations, particularly for the low-to-middle values of γ within the entire range of adopted width-to-width ratios. Despite the low coefficient of variation, the approach used to account for buckling in the chord web seems to lead to an overestimation of the mean deviation. On the other hand, even though the coefficient of variation is approximately 20%, the model proposed in this study offers more dependable results due to its tendency to slightly underestimate the design strengths in the context of numerical simulations.

6.3.5 Plastic mechanism model developed by Zhao and Hancock

The original plastic mechanism model developed by Zhao and Hancock [157] has been incorporated in the comparison to highlight the necessity for adjustments in order to obtain reliable results when assessing the design strength of fully offset and SCE connections with eccentricity. The primary equations governing the rotation capacities of the yield lines are provided in Table 2.1.

Upon reviewing column 11 in Table 6.2, it becomes apparent that the unmodified original model is unsuitable for offset connections. Despite a tolerable coefficient of variation, the substantial mean deviation renders the model inadequate, resulting in a notable underestimation of the actual capacity of RHS SCE connections as estimated by the traditional Zhao and Hancock model.

6.3.6 Comparison with outcomes of experimental research

To validate the current model, a series of comparisons with available test results was conducted. While experimental outcomes primarily serve as reference data for the validation of numerical models [165], it should be noted that the number of tests specifically targeting offset connections

is limited. Nonetheless, the present study undertook certain comparisons with test data obtained from Kalmykova and Wald [50], Dawe et al. [25], and Wei and Packer [146]. The final column in Table 6.2 confirms the suitability of the proposed model. Notably, the maximum relative deviation from the conservative side (i.e., when the predicted design strength surpasses that obtained from the tests) remains below 15%. Other discrepancies fall within an acceptable range, characterized by negligible absolute deviations.

Table 6.2 Comparison of proposed analytical model with resistances obtained using other models and tests

Specimen label	Geometry			Comparison							
	e, [mm]	β	γ	$P_M/F_{FEM,s}$	$P_{M,me}/F_{FEM,3\%}$	$P_M/N_{1,Rd}$	$P_M/N_{2,Rd}$	$P_M/N_{3,Rd}$	$P_M/N_{4,Rd}$	$P_M/N_{5,Rd}$	P_M/F_{exp}
1	2	3	4	5	6	7	8	9	10	11	12
2.02.T.Sy.Co.235, [50]	0	0.3	12.5								1.131
1.01.T.Ec.Co.355, [50]	23	0.3	12.5								0.713
CH6_B80-10	63	0.32	19.8	0.844	0.672	1.648	2.124	1.292	0.996	2.845	
CH8_B80-10	63		15.6	0.809	0.638	1.648	1.961	1.230	0.980	3.430	
CH10_B80-10	60		12.5	0.882	0.692	1.554	1.543	1.031	0.856	3.590	
CH12_B80-10	56.2		10.0	0.948	0.741	1.463	1.174	0.838	0.735	3.557	
CH14_B80-10	53.7		8.8	0.989	0.773	1.415	1.032	0.756	0.688	3.464	
CH16_B80-10	51		7.8	1.025	0.800	1.372	0.947	0.704	0.663	3.328	
CH6_B100-10	53	0.4	19.8	0.838	0.703	1.636	1.768	1.148	0.934	2.795	
CH8_B100-10	53		15.6	0.833	0.692	1.636	1.705	1.121	0.940	3.296	
CH10_B100-10	50		12.5	0.876	0.726	1.544	1.392	0.960	0.834	3.371	
CH12_B100-10	46.2		10	0.950	0.785	1.455	1.136	0.817	0.742	3.275	
CH14_B100-10	43.7		8.8	0.997	0.823	1.409	1.017	0.747	0.700	3.160	
CH16_B100-10	41		7.8	1.025	0.846	1.369	0.939	0.699	0.675	3.014	
CH6_B120-12.5	43	0.48	19.8	0.847	0.748	1.602	1.635	1.082	0.939	2.702	
CH8_B120-12.5	43		15.6	0.823	0.721	1.602	1.346	0.948	0.841	3.092	
CH10_B120-12.5	40		12.5	0.821	0.717	1.512	1.170	0.844	0.771	3.072	
CH12_B120-12.5	36.2		10	0.907	0.791	1.427	1.009	0.745	0.706	2.914	
CH14_B120-12.5	33.7		8.8	0.942	0.821	1.384	0.943	0.704	0.683	2.781	
CH16_B120-12.5	31		7.8	0.966	0.843	1.346	0.904	0.677	0.672	2.631	
CH6_B150-12.5	28	0.6	19.8	0.850	0.796	1.480	1.631	1.052	0.975	2.400	
CH8_B150-12.5	28		15.6	0.846	0.787	1.480	1.132	0.819	0.768	2.644	
CH10_B150-12.5	25		12.5	0.850	0.791	1.407	1.058	0.769	0.739	2.532	
CH12_B150-12.5	21.2		10	0.907	0.846	1.341	0.973	0.714	0.707	2.331	
CH14_B150-12.5	18.7		8.8	0.930	0.870	1.309	0.942	0.693	0.700	2.195	

Specimen label	Geometry			Comparison							
	e, [mm]	β	γ	$P_M/F_{FEM,s}$	$P_{M,me}/F_{FEM,3\%}$	$P_M/N_{1,Rd}$	$P_M/N_{2,Rd}$	$P_M/N_{3,Rd}$	$P_M/N_{4,Rd}$	$P_M/N_{5,Rd}$	P_M/F_{exp}
1	2	3	4	5	6	7	8	9	10	11	12
CH16_B150-12.5	16		7.8	0.964	0.906	1.284	0.930	0.682	0.703	2.053	
CH6_B180-12.5	13	0.72	19.8	0.854	0.862	1.323	1.863	1.093	1.073	1.920	
CH8_B180-12.5	13		15.6	0.840	0.841	1.323	1.248	0.848	0.832	2.041	
CH10_B180-12.5	10		12.5	0.860	0.868	1.283	1.207	0.821	0.825	1.887	
CH12_B180-12.5	6.2		10	0.898	0.919	1.257	1.154	0.791	0.817	1.684	
CH14_B180-12.5	3.7		8.8	0.924	0.957	1.252	1.145	0.786	0.826	1.560	
CH16_B180-12.5	1		7.8	0.965	1.014	1.257	1.162	0.795	0.852	1.437	
CH6_B200-12.5	3	0.8	19.8	0.852		1.361	2.355	1.263	1.327		
CH8_B200-12.5	3		15.6	0.870		1.361	1.364	0.908	0.935		
CH10_B200-12.5	0		12.5	0.959		1.381	1.464	0.957	1.009		
T1. Bu et al [11]		0.5	15.9								0.883
T2. Bu et al [11]		0.5	10.7								1.092
T3. Bu et al [11]		0.75	15.9								0.985
T4. Bu et al [11]		0.75	10.7								1.217
T8. Dawe [25]	25.5	0.66	12.5								1.052
T9. Dawe [25]	25.6	0.66	12.2								0.956
T10. Dawe [25]	25.6	0.66	12.1								1.335
	Mean			0.900	0.800	1.428	1.314	0.889	0.832	2.700	
	Standard deviation			0.062	0.086	0.122	0.374	0.179	0.144	0.617	
	COV. %			6.897	10.696	8.530	28.450	20.183	17.361	22.856	

Note.

1. In calculations using presented model, the values of $k = \frac{e_2}{e_1}$ is adopted equal to 0.85 for comparisons with tests.
2. Abbreviations:
   P_M is the strength obtained using the proposed plastic mechanism model,
   $P_{M,me}$ is the strength obtained with the proposed plastic mechanism model, taking into account a membrane effect,

$F_{FEM,s}$ is the strength obtained from a shell FE model in Abaqus, assuming $3\%b_0$ deformation limit,
$F_{FEM,3\%}$ is the strength obtained from a solid FE model in Abaqus, assuming $3\%b_0$ deformation limit,
$N_{1,Rd}$ is the design resistance of a chord face according to EN 1993-1-8:2003,
$N_{2,Rd}$ is the design resistance of a chord web according to EN 1993-1-8:2003,
$N_{3,Rd}$ is the average resistance for an equal stepped connection,
$N_{4,Rd}$ is the design resistance according to Bu-Wei-Packer approach,
$N_{5,Rd}$ is the strength obtained with the plastic mechanism model by Zhao and Hancock,
F_{exp} is the strength obtained from laboratory experiments, assuming $3\%b_0$ deformation limit.

Table 6.3 Comparison of proposed analytical model with numerical simulations of X-type connections and analytical model presented in [11]

Specimen label[1]	Geometry				Comparison				
	e^2, [mm]	β	γ	$k = \frac{e_2}{e_1}$	F_{SK}	F_{BWP}	F_{FEM}	F_{SK}/F_{FEM}	F_{BWP}/F_{FEM}
1	2	3	4	5	6	7	8	9	10
		0.25	10	0.175	1570.2	2127.9	-	-	-
			15	0.175	697.9	1107.1	761.0	0.917	1.455
			20	0.175	392.5	652.5	476.0	0.825	1.371
			25	0.175	251.2	408.2	352.0	0.714	1.160
			30	0.175	174.5	268.6	264.0	0.661	1.017
			35	0.175	128.2	185.3	200.0	0.641	0.926
		0.4	10	0.200	1889.8	2593.6	1762.0	1.073	1.472
			15	0.200	839.9	1365.7	947.0	0.887	1.442
			20	0.200	472.4	807.8	614.0	0.769	1.316
			25	0.200	302.4	504.5	429.0	0.705	1.176
			30	0.200	210.0	335.8	321.0	0.654	1.046
			35	0.200	154.3	238.2	251.0	0.615	0.949
		0.5	10	0.225	2131.7	2916.7	1910.0	1.116	1.527
			15	0.225	947.4	1543.5	1084.0	0.874	1.424
			20	0.225	532.9	914.3	676.0	0.788	1.353
			25	0.225	341.1	582.2	476.0	0.717	1.223
			30	0.225	236.8	396.6	352.0	0.673	1.127
			35	0.225	174.0	284.9	272.0	0.640	1.047
		0.6	10	0.250	2463.7	3258.6	2429.0	1.014	1.342
			15	0.250	1094.9	1729.5	1261.0	0.868	1.372
			20	0.250	615.9	1035.9	748.0	0.823	1.385
			25	0.250	394.2	673.8	526.0	0.749	1.281
			30	0.250	273.7	465.6	358.0	0.765	1.301
			35	0.250	201.1	339.3	295.0	0.682	1.150

[1] Non-specified as per [11]

Specimen label[1]	Geometry				Comparison				
	e^2, [mm]	β	γ	$k = \frac{e_2}{e_1}$	F_{SK}	F_{BWP}	F_{FEM}	F_{SK}/F_{FEM}	F_{BWP}/F_{FEM}
1	2	3	4	5	6	7	8	9	10
		0.75	10	0.275	3413.4	3855.5	3034.0	1.125	1.271
			15	0.275	1516.9	2048.6	1536.0	0.988	1.334
			20	0.275	853.2	1257.8	898.0	0.950	1.401
			25	0.275	546.1	835.3	624.0	0.875	1.339
			30	0.275	379.2	590.7	450.0	0.843	1.313
			35	0.275	278.6	441.3	340.0	0.819	1.298
		0.85	10	0.300	4800.3	4437.6	3577.0	1.342	1.241
			15	0.300	2133.0	2355.8	1854.0	1.150	1.271
			20	0.300	1199.8	1455.8	1081.0	1.110	1.347
			25	0.300	767.9	978.6	738.0	1.040	1.326
			30	0.300	533.3	702.6	526.0	1.014	1.336
			35	0.300	391.8	533.9	392.0	0.999	1.362
	Mean							0.869	1.277
	Standard deviation							0.177	0.145
	COV, %							20.360	11.350

Note.
The values of $k = \frac{e_2}{e_1}$ is adopted in a range 0.175…0.3 in calculations using presented model for X-type connections

CHAPTER 7:
CONCLUSIONS AND RECOMMENTATIONS

The introduction of lateral offset in X-type RHS connections, where the brace member's vertical plane shifts from the chord centreline toward the chord wall, significantly impacts the connection's resistance. This influence cannot be disregarded in the analytical approaches developed for the design of offset RHS-to-RHS connections. To tackle the challenge of determining the design strength of RHS to RHS X-type connections, several theoretical and laboratory studies have been undertaken [50], [11], [146]. This study presents a comprehensive analytical model capable of estimating the design strength of RHS T-type connections under axial compression, encompassing a wide spectrum of width-to-width ratio β and width-to-double thickness ratio γ.

The proposed model for RHS T-type connections under axial compression is rooted in the plastic mechanism model developed by Zhao and Hancock [157] for stepped RHS T-type connections subjected to axial force.

The model's development entails two key steps: validation through test results and verification [165], which encompasses evaluating the model through numerical simulations. The numerical simulation program [50] encompassed 33 models spanning a broad array of γ values within each β ratio range, ranging from 0.32 to 0.8.

In many instances, using different methods to determine the analytical resistance of X-type connections yields unsatisfactory results, with overestimation of the actual resistance obtained from numerical simulations. Nonetheless, the analytical expression (27) founded on the combined yield-line mechanism proposed by Bu, Wei, and Packer [11] offers satisfactory design strength values for fully offset RHS-to-RHS X-type connections with a brace member flush against the chord wall. However, this equation may not accurately apply to X-type connections with non-matching surfaces between the brace and chord, leading to substantial underestimation of the design strength when contrasted with results from numerical simulations.

The analytical equations introduced in the present model offer viable solutions for both types of offset T-type connections across an extensive range of γ and β ratios. Furthermore, the model's applicability extends to the design of X-type RHS to RHS connections in both configurations. The comparative analysis presented in Table 2.1, comparing design strength values derived from the developed equations to outcomes from nonlinear numerical FE simulations conducted by the authors in [49] and by Bu et al. in [11], demonstrates good agreement and sufficient accuracy of the proposed model.

BIBLIOGRAPHY

[1] ABAQUS. 2010. *ABAQUS/Standard Version 6.10 User's Manual: Volumes I-III.* Pawtucket, Rhodle Island: Hibbittt, Karlsson & Sorensen Inc.

[2] American Institute of Steel Construction (2005). Specification for structural steel buildings. ANSI/AISC 360-05. American Institute of Steel Construction, Chicago, USA.

[3] American Welding Society (2002). AWSD 1.1: Structural welding code. Miami, USA.

[4] Ahmadi, H., Lotfollahi-Yaghin, M. A., Yong-Bo, S., & Aminfar, M. H. (2012). Parametric study and formulation of outer-brace geometric stress concentration factors in internally ring-stiffened tubular KT-joints of offshore structures. *Applied Ocean Research*, 38, 74-91.

[5] Ahmadi, H., & Zavvar, E. (2016). The effect of multi-planarity on the SCFs in offshore tubular KT-joints subjected to in-plane and out-of-plane bending loads. *Thin-Walled Structures*, *106*, 148-165.

[6] Standards Association of Australia (1998). Steel structures: AS 4100-1998. Sydney, Australia.

[7] Becque, J. (2010). Inelastic plate buckling. *Journal of engineering mechanics*, *136*(9), 1123-1130.

[8] Becque, J., & Cheng, S. (2017). Sidewall buckling of equal-width RHS truss X-joints. Journal of Structural Engineering, 143(2), 04016179.

[9] Bian, L. C., & Lim, J. K. (2003). Fatigue strength and stress concentration factors of CHS-to-RHS T-joints. *Journal of Constructional Steel Research*, *59*(5), 627-640.

[10] Bittencourt, M. C., de Lima, L. R. O., Vellasco, P. D. S., da Silva, J. G. S., & Neves, L. D. C. (2007). A numerical analysis of tubular joints under static loading. *Proceedings of APCOM'07 in conjunction with EPMESC XI*, 3-6.

[11] Bu, X. D., Wei, F., & Packer, J. A. (2021). Laterally offset RHS X-connections. *Journal of Structural Engineering*, *147*(1), 04020286.

[12] Canadian Standards Association (2009). CSA-S16-09: Design of steel structures. Toronto, Canada.

[13] Cao, J. J., Packer, J. A., & Yang, G. J. (1998). Yield line analysis of RHS connections with axial loads. *Journal of Constructional Steel Research*, *48*(1), 1-25.

[14] CEN, European Committee for Standardization (2005). EN 1993-1-1. Design Steel Structures – Part 1-1: General rules and rules for buildings. Brussels, Belgium.

[15] CEN, European Committee for Standardization (2006). EN 1993-1-8. Design of steel structures - Part 1-8: Design of joints. Brussels, Belgium.

[16] CEN, European Committee for Standardization (2005). EN 1993-1-9. Design of steel structures - Part 1-9: Fatigue. Brussels, Belgium.

[17] CEN, European Committee for Standardization (2005). EN 1994-1-1. Design of composite steel and concrete structures - Part 1-1: General rules and rules for buildings. Brussels, Belgium.

[18] Cheng, S., & Becque, J. (2016). A design methodology for side wall failure of RHS truss X-joints accounting for compressive chord pre-load. *Engineering Structures*, *126*, 689-702.

[19] Chen, Y., & Wang, J. (2015). Axial compression physical testing of traditional and bird beak SHS T-joints. *Journal of Central South University*, *22*(6), 2328-2338.

[20] Chen, Y., Shao, Y.B. (2016). Static Strength of square tubular Y-joints with reinforced chord under axial compression. *Advanced Steel Construction 12 (2016): 211−226.*

[21] Cheng, B., Qian, Q., & Zhao, X. L. (2015). Numerical investigation on stress concentration factors of square bird-beak SHS T-joints subject to axial forces. *Thin-Walled Structures*, *94*, 435-445.

[22] Cheng, B., Qian, Q., & Zhao, X. L. (2015). Stress concentration factors and fatigue behaviour of square bird-beak SHS T-joints under out-of-plane bending. *Engineering Structures*, *99*, 677-684.

[23] Cheng, C., Yongbo, S., & Jie, Y. (2013). Experimental and numerical study on fire resistance of circular tubular T-joints. *Journal of Constructional Steel Research*, *85*, 24-39.

[24] Neves, L. C., Lima, L. D., Jordão, S., & Silva, J. D. (2005). Structural Analysis of “T” and “KT” Joints of a Steel Truss Structure Using the Finite Element Method. In *Proceedings of the Tenth International Conference on Civil, Structural and Environmental Engineering Computing* (pp. 1-15).

[25] Dawe, J. L., Liu, Y., Zhang, R., & Dukuze, A. (2006). Experimental study of offset HSS connections. *Journal of Structural Engineering*, *132*(5), 717-725.

[26] Davies, G. (1990). Developments in joint research. *Steel construction today*, *4*(1), 7-16.

[27] Davies, G., & Packer, J. A. (1982). Predicting the strength of branch plate–RHS connections for punching shear. *Canadian journal of civil engineering*, *9*(3), 458-467.

[28] Dutta, D., & Mang, F. (1983). Fatigue Tests and Design of Offshore Tubular Joints.

[29] Garifullin, M., Bronzova, M., Jokinen, T., Heinisuo, M., & Kovačič, B. (2016). Effect of fillet welds on initial rotational stiffness of welded tubular joints. *Procedia Engineering*, *165*, 1643-1650.

[30] Garifullin, M., Pajunen, S., Mela, K., Heinisuo, M., & Havula, J. (2017). Initial in-plane rotational stiffness of welded RHS T joints with axial force in main member. Journal of Constructional Steel Research, 139, 353-362.

[31] Gho, W. M., Gao, F., & Yang, Y. (2006). Strain and stress concentration of completely overlapped tubular CHS joints under basic loadings. *Journal of Constructional Steel Research*, *62*(7), 656-674.

[32] Giddings, T. W., & Wardenier, J. (1986). CIDECT Monograph No 6–The Strength and Behaviour of Statically Loaded Welded Connections In Structural Hollow Sections.

[33] International Institute of Welding (1989). Design recommendations for hollow section joints—predominantly statically loaded. 2nd ed. Genoa (Italy): IIW Doc. XV-701-89; 1989.

[34] International Institute of Welding (2013). Static design procedure for welded hollow-section joints – Recommendations, 4th Edition. IIW Doc. XV-1439-13. ISO/FDIS 14346.

[35] Jaspart, J. P., & Weynand, K. (2015). Design of hollow section joints using the component method. *Tubular Structures XV*, 403-410.

[36] Jurčíková, A., & Rosmanit, M. (2012). FEM model of joint consisting RHS and HEA profiles. *Procedia Engineering*, *40*, 183-188.

[37] Jurcíková, A., Rosmanit, M. (2013). Recommendations for numerical modelling and analytical assessment of a planar steel CHS joint. *Transactions of the VŠB – Technical University of Ostrava No. 2, 2013, Vol. XIII, Civil Engineering Series*.

[38] Fadden, M. F., & McCormick, J. P. (2012). Finite Element Modeling of HSS-to-HSS Moment Connections. In *15th World Conf. Earthq. Eng. Lisbon Port*.

[39] Feng, R., & Young, B. (2008). Tests of concrete-filled stainless steel tubular T-joints. *Journal of Constructional Steel Research*, *64*(11), 1283-1293.

[40] Feng, R., & Young, B. (2008). Experimental investigation of cold-formed stainless steel tubular T-joints. *Thin-Walled Structures*, *46*(10), 1129-1142.

[41] Feng, R., & Young, B. (2010). Tests and behaviour of cold-formed stainless steel tubular X-joints. *Thin-Walled Structures*, *48*(12), 921-934.

[42] Feng, R., & Young, B. (2011). Design of cold-formed stainless steel tubular T-and X-joints. *Journal of Constructional Steel Research*, *67*(3), 421-436.

[43] Feng, R., & Young, B. (2013). Stress concentration factors of cold-formed stainless steel tubular X-joints. *Journal of Constructional Steel Research*, *91*, 26-41.

[44] Feng, R., & Young, B. (2015). Theoretical analysis of cold-formed stainless steel tubular joints. *Engineering Structures*, *83*, 99-115.

[45] Feng, R., Chen, Y., Wei, L., & Ruan, X. (2015). Behaviour of CHS brace-to-H-shaped chord X-joints under in-plane bending. *Journal of Constructional Steel Research*, *114*, 8-19.

[46] Fenkli, M., Çelik, İ., Kimilli, N., & Sivri, M. (2017). Investigation of Capacity on the Hollow Sections Connections with Stiffening Plate. *Advanced Steel Construction*, *13*(1).

[47] Jin, M., Zhao, J., Chang, J., & Zhang, D. (2012). Experimental and parametric study on the post-fire behaviour of tubular T-joint. *Journal of Constructional Steel Research*, *70*, 93-100.

[48] Jubb, J. E. M., & Redwood, R. G. (1966, May). Design of joints to box sections. In *The Institution of Structural Engineers Conference on Industrialised Building and the Structural Engineer, UK*.

[49] Kalmykova, S., & Wald, F. (2021). Peculiarities of resistance definition for welded offset T-joint between RHS members. *ce/papers*, *4*(2-4), 2465-2471.

[50] Kalmykova, S., & Wald, F. (2019). Full-scale experimental study of welded RHS T-joints with offset and it main outcomes. *Grant journal*, *8*(1), 76-81.

[51] Kamba, T., & Taclendo, C. (1998). CHS column connections without stiffener. In *Eighth International Symposium on Tubular Structures, Singapore* (Vol. 26, No. 28).

[52] Kato, B., Nishiyama. I. (1980). *T-joints made of rectangular tubes*. In: Proceedings of the 5th International Conference on Cold-Formed Steel Structures, St. Louis (MI, USA), 1980.

[53] Korol, R.M., Mirza, F.A. (1982). Finite Element Analysis of RHS T-Joints. *Journal of the Structural Division, 1982, Vol. 108, Issue 9, Pg. 2081-2098*.

[54] Kosteski, N. (2001). Branch plate-to-rectangular hollow structural section connections (Doctoral dissertation).

[55] Kosteski, N., Packer, J. A., & Puthli, R. S. (2003). A finite element method based yield load determination procedure for hollow structural section connections. *Journal of Constructional Steel Research*, *59*(4), 453-471.

[56] Kvočák, V., & Beke, P. (2008). Experimental analysis of "T"-joints created from various types of sections". *Journal of Civil Engineering*, *3*(2), 51-60.

[57] Kvocák, V., & Beke, P. (2010). Cross-section stiffness ratios and the resistance of joints composed of various sections. In *Modern Building Materials, Structures and Techniques. Proceedings of the International Conference*, *Litva*.

[58] Kvočák, V., Beke, P., & Vargová, R. (2012). Joint composed of various section. *Procedia Engineering*, *40*, 44-49.

[59] Kwasniewski, L., & Bojanowski, C. (2015). Principles of verification and validation. *Journal of Structural Fire Engineering*, *6*(1), 29-40.

[60] Kurobane, Y., Makino, Y., & Ochi, K. (1984). Ultimate resistance of unstiffened tubular joints. *Journal of Structural Engineering*, *110*(2), 385-400.

[61] Kurobane, Y., Packer, J. A., Wardenier, J., & Yeomans, N. (2004). Design guide for structural hollow section column connections. CIDECT Design Guide No. 9. *Köln: TÜV-Verlag*.

[62] Lee, M.M.K., & Wilmshurst, S. R. (1995). Numerical modelling of CHS joints with multiplanar double-K configuration. *Journal of constructional steel research*, *32*(3), 281-301.

[63] Lee, M.M.K., Llewelyn-Parry, A. (1998). Ultimate strength of ring stiffened T-joints: A theoretical model. In *Proceedings of the 8th International Symposium on Tubular Structures. Singapore*.

[64] Lee, M.M.K., & Llewelyn-Parry, A. (1999). Strength of ring-stiffened tubular T-joints in offshore structures—: a numerical parametric study. *Journal of Constructional Steel Research*, *51*(3), 239-264.

[65] Lee, M.M.K., (1999b). Strength, stress and fracture analyses of offshore tubular joints using finite elements. *Journal of Constructional Steel Research 51 (1999), 265-286.*

[66] Lee, M. M. K., & Llewelyn-Parry, A. (2004). Offshore tubular T-joints reinforced with internal plain annular ring stiffeners. *Journal of Structural Engineering*, *130*(6), 942-951.

[67] Lie, S. T., Chiew, S. P., Lee, C. K., & Yang, Z. M. (2005). The ultimate behaviour of cracked square hollow section T-joints. In *Fourth International Conference on Advances in Steel Structures* (pp. 1099-1106). Elsevier Science Ltd.

[68] Lima, L.R.O., Neves, L.F.C., Silva, J.G.S., Vellasco, P.C.G.S., Andrade, S.A.L., (2007). *Parametric analysis of RHS T joints under static loading.* CC2007 - 11th International Conference on Civil, Structural and Environmental Engineering Computing, Saint Julians, Proceedings of the 9th International Conference on the Application of Artificial Intelligence to Civil, Structural and Environmental Engineering, Edinburgh, Civil Comp Press 1: 1-15.

[69] Lip, H., Rasmussen, Kim J.R. (2006). *Strength of Welded T-Joint Truss Connections between Equal Width Cold-Formed RHS*. Research Report No.R831. The University of Sydney. Department of Civil Engineering, Centre for Advanced Structural Engineering.

[70] Teh, L. H., & Rasmussen, K. J. (2007). Strength of arc-welded T-joints between equal width cold-formed RHS. *Journal of Constructional Steel Research*, *63*(4), 571-579.

[71] Liu, D.K., Wardenier, J. and van der Vegte, G.J. (2004). New chord stress functions for rectangular hollow section joints. *Proceedings of the 14th International Offshore and Polar Engineering Conference*. Toulon, France, International Society of Offshore and Polar Engineers (ISOPE), Vol. IV.

[72] Liu, M. L., Zhao, J. C., & Jin, M. (2009). Study on load capacity and deformation of T-joints with reinforced ring at elevated temperatures. *China Offshore Platform*, *24*(5), 17-23.

[73] Liu, M., Zhao, J., & Jin, M. (2010). An experimental study of the mechanical behaviour of steel planar tubular trusses in a fire. *Journal of Constructional Steel Research*, *66*(4), 504-511.

[74] Liu, G., Zhao, X., & Huang, Y. (2015). Prediction of stress distribution along the intersection of tubular T-joints by a novel structural stress approach. *International Journal of Fatigue*, *80*, 216-230.

[75] Liu, Y., Wang, F., Yang, Q., & Shang, X. (2015). Research on the performance of T-type RHS Joints. In *2015 International Conference on Advanced Engineering Materials and Technology* (pp. 939-942). Atlantis Press.

[76] Lu Yu, Y., L.H., de Winkel, G.D., Wardenier, J. (1994). Deformation limit for the ultimate strength of hollow section joints. *Proceedings of the 6th International Symposium on Tubular Structures*. Melbourne, Australia, A.A. Balkema, pp. 341-347.

[77] Lu Yu, Y., Wardenier, J. (1994). The static strength and behaviour of uniplanar and multiplanar connections between I-beams and RHS columns. Connections in Steel Structures III, 1996, pp. 127-135.

[78] Mashiri, F. R., & Zhao, X. L. (2004). Plastic mechanism analysis of welded thin-walled T-joints made up of circular braces and square chords under in-plane bending. *Thin-Walled Structures*, *42*(5), 759-783.

[79] Mashiri, F. R., Zhao, X. L., & Grundy, P. (2004). Stress concentration factors and fatigue behaviour of welded thin-walled CHS–SHS T-joints under in-plane bending. *Engineering Structures*, *26*(13), 1861-1875.

[80] Mashiri, F. R., Zhao, X. L., Hirt, M. A., & Nussbaumer, A. (2007). Size effect of welded thin-walled tubular joints. *International Journal of Structural Stability and Dynamics*, *7*(01), 101-127.

[81] Mashiri, F. R., & Zhao, X. L. (2010). Square hollow section (SHS) T-joints with concrete-filled chords subjected to in-plane fatigue loading in the brace. *Thin-Walled Structures*, *48*(2), 150-158.

[82] De Matos, R. M. M. P., Costa-Neves, L. F., de Lima, L. R. O., Vellasco, P. C., & da Silva, J. G. S. (2015). Resistance and elastic stiffness of RHS" T" joints: part I-axial brace loading. *Latin American Journal of Solids and Structures*, *12*, 2159-2179.

[83] De Matos, R. M. M. P., Costa-Neves, L. F., de Lima, L. R. O., Vellasco, P. C., & da Silva, J. G. S. (2015). Resistance and Elastic Stiffness of RHS" T" Joints: Part II-Combined Axial Brace and Chord Loading. *Latin American Journal of Solids and Structures*, *12*, 2180-2207.

[84] Martinez-Saucedo, G., Packer, J. A., & Willibald, S. (2006). Parametric finite element study of slotted end connections to circular hollow sections. *Engineering structures*, *28*(14), 1956-1971.

[85] Morris, G. A., & Packer, J. A. (1988). Yield line analysis of cropped-web warren truss joints. *Journal of Structural Engineering*, *114*(10), 2210-2224.

[86] Moazed, R., Fotouhi, R., Szyszkowski, W., & Bitner, D. (2010). Welded T-joint connections of square thin-walled tubes under a multi-axial state of stress. *The Journal of Strain Analysis for Engineering Design*, *45*(8), 629-646.

[87] Mouty J. (1976). Calus des Changes Ultimes des Assemblages Soudes de Profils Creux Carres et Rectan-gulaires, Construction Metallique, No.2, pp. 37-58, Paris, France.

[88] Mouty, J. (1977). *Theoretical prediction of welded joint strength*. Proceedings of the International Symposium on Hollow Structural Sections. Toronto, Canada.

[89] Neves, L. F. D. C. (2004). *Comportamento monotónico e cíclico de ligações de eixo fraco e tubulares em estruturas metálicas e mistas aço-betão* (Doctoral dissertation).

[90] Nizer, A., de Lima, L. R., da S. Vellasco, P. C., de Andrade, S. A., da S. Goulart, E., da Silva, A. T., & da C. Neves, L. F. (2016). Experimental and numerical assessment of RHS T-joints subjected to brace and chord axial forces. *Steel Construction*, *9*(4), 315-322.

[91] N'diaye, A., Hariri, S., Pluvinage, G., & Azari, Z. (2009). Stress concentration factor analysis for welded, notched tubular T-joints under combined axial, bending and dynamic loading. *International journal of fatigue*, *31*(2), 367-374.

[92] Nguyen, M.P., Fung, T.C., Tan, K.H. (2010). An experimental study of structural behaviours of CHS T-joints subjected to brace axial compression in fire condition. *Tubular structures XIII, Hong Kong, 725–32.*

[93] Nobre, D. S., de Lima, L. R., Vellasco, P. C. D. S., Costa-Neves, L. F., & Silva, A. T. D. (2015). Evaluation of CHS tubular KK joints. *Latin American Journal of Solids and Structures*, *12*, 2143-2158.

[94] Nogueira, M. M., de Lima, L. R., Vellasco, P. C. D. S., & Young, B. (2022). Semi-analytical formulation for stainless steel tubular T-joints chord sidewall failure. *Thin-Walled Structures*, *179*, 109505.

[95] Packer, J. A., Davies, G., & Coutie, M. G. (1980). Yield strength of gapped joints in rectangular hollow section trusses. In *Proceedings of the Institution of Civil Engineers*, *69*(4), 995-1013.

[96] Packer, J. A. (1993). Moment connections between rectangular hollow sections. *Journal of Constructional Steel Research*, *25*(1-2), 63-81.

[97] Packer J.A., Henderson J.E. (1997). Hollow structural section connections and trusses: A design guide. *Willowdale (Ontario): Canadian Institute of Steel Construction*.

[98] Packer, J. A., Mashiri, F. R., Zhao, X. L., & Willibald, S. (2007). Static and fatigue design of CHS-to-RHS welded connections using a branch conversion method. *Journal of Constructional Steel Research*, *63*(1), 82-95.

[99] Packer J.A., Wardenier J., Zhao X.L., van der Vegte G.J., & Kurobane Y. (2009). Design guide for rectangular hollow section (RHS) joints under predominantly static loading. CIDECT, 2nd Edition, 2009. (CIDECT Series: Construction with hollow steel sections, Vol. 3.). *Geneva*.

[100] Qian, X. D., Choo, Y. S., Van Der Vegte, G. J., & Wardenier, J. (2008, September). Evaluation of the new IIW CHS strength formulae for thick-walled joints. In *Proceedings of the 12th*

International Symposium on Tubular Structures, Shanghai. Taylor & Francis, London (pp. 271-280).

[101] Redwood, R. G. (1965). The behaviour of joints between rectangular hollow structural members. *Civil Engineering and Public Works Review*, *60*(711), 1463-1469.

[102] Schumacher, A., & Nussbaumer, A. (2006). Experimental study on the fatigue behaviour of welded tubular K-joints for bridges. *Engineering structures*, *28*(5), 745-755.

[103] Shao, Y., Zheng, Y., Zhao, H., & Yang, D. (2016). Performance of tubular T-joints at elevated temperature by considering effect of chord compressive stress. *Thin-Walled Structures*, *98*, 533-546.

[104] Shao, Y., Zhao, H., & Yang, D. (2017). Discussion on two methods for determining static strength of tubular T-joints at elevated temperature. *Advances in Structural Engineering*, *20*(5), 704-721.

[105] Shen, W., & Choo, Y. S. (2012). Stress intensity factor for a tubular T-joint with grouted chord. *Engineering Structures*, *35*, 37-47.

[106] Schumacher, A., & Nussbaumer, A. (2006). Experimental study on the fatigue behaviour of welded tubular K-joints for bridges. *Engineering structures*, *28*(5), 745-755.

[107] Da Silva, L. S., & Coelho, A. G. (2001). An analytical evaluation of the response of steel joints under bending and axial force. *Computers & Structures*, *79*(8), 873-881.

[108] Da Silva, L. S. (2008). Towards a consistent design approach for steel joints under generalized loading. *Journal of Constructional Steel Research*, *64*(9), 1059-1075.

[109] Da Silva, R. S., Lima, L., Vellasco, P. C. G. S., Silva, J., & Neves, L. (2012). Numerical evaluation of CHS K joints. *International Journal of Modelling and Simulation for Petroleum Industry*, *6*(1).

[110] Da Silva R.S., Lima, L.R.O., Vellasco, P.C.G.S., Silva, J.G.S., Freitas, A.M.S., Nunes, G.V. (2012). Overview of Tubular Joints – EC3 X New CIDECT Formulations. In *Proceedings of the Connections VII - 7th International Workshop on Connections in Steel Structures*. Timisoara, 2012. Vol. 1. p. 1-10.

[111] Soh, A. K., & Soh, C. K. (1990). A parametric stress analysis of T/Y and K square-to-square tubular joints. *Journal of Constructional Steel Research*, *15*(3), 173-190.

[112] Steenhuis, M., Gresnigt, N., & Weynand, K. (1994, January). Pre-design of semi-rigid joints in steel frames. In *Proceedings of the Second State of the Art Workshop on Semi-Rigid Behaviour of Civil Engineering Structural Connections* (pp. 131-140).

[113] Szlendak, J., & Brodka, J. (1985). Yield and buckling strength of T, Y and X joints in rectangular hollow section trusses. Technical note. In *Proceedings of the Institution of Civil Engineers*, *79*(1), 167-180.

[114] Szlendak, J., & Brodka, J. (1985). Strengthening of T moment of RHS joints. In *Proceedings of the Institution of Civil Engineers*, *79*(4), 717-727.

[115] Szlendak, J. (1991). Beam-column welded RHS connections. *Thin-walled structures*, *12*(1), 63-80.

[116] Tong, L., Fu, Y., Liu, Y., & Zhao, X. L. (2014). Stress concentration factors of diamond bird-beak SHS T-joints under brace loading. *Thin-Walled Structures*, *74*, 201-212.

[117] Tong, L., Xu, G., Liu, Y., Yan, D., & Zhao, X. L. (2015). Finite element analysis and formulae for stress concentration factors of diamond bird-beak SHS T-joints. *Thin-Walled Structures*, *86*, 108-120.

[118] Lipp, A., & Ummenhofer, T. (2015, April). Influence of tensile chord stresses on the strength of CHS X-joints—Experimental and numerical investigations. In *Proc. 15th Int'l Symposium on Tubular Structures, Tubular Structures XV* (pp. 379-386).

[119] Van der Vegte, G. J., De Koning, C. H. M., Puthli, R. S., & Wardenier, J. (1991). Numerical simulation of experiments on multiplanar tubular steel X-joints. *International journal of offshore and polar engineering*, *1*(03).

[120] Van der Vegte, G.J., Makino, Y., Wardenier, J. (2004). The influence of boundary conditions on the chord load effect for CHS gap K-joints. In *Proceedings of the 5th International Workshop Connections in Steel Structures V, Amsterdam*, Netherlands, 433-444.

[121] Van Wingerde, A. M., Puthli, R. S., Wardenier, J., Dutta, D., & Packer, J. A. (1992, June). Design recommendations and commentary regarding the fatigue behaviour of hollow section joints. In *ISOPE International Ocean and Polar Engineering Conference* (pp. ISOPE-I). ISOPE.

[122] Van Wingerde, A. M., Packer, J. A., & Wardenier, J. (1997). SCF formulae for fatigue design of K-connections between square hollow sections. *Journal of Constructional Steel Research*, *43*(1-3), 87-118.

[123] Van der Vegte, G.J., Makino, Y. (2006). *Ultimate strength formulation for axially loaded CHS uniplanar T-joints*. International Journal of Offshore and Polar Engineering, International Society of Offshore and Polar Engineers (ISOPE), Vol. 16, No. 4, pp. 305-312.

[124] Van der Vegte, G.J., Wardenier, J., Makino, Y. (2007). Effect of chord load on ultimate strength of CHS X-joints. *International Journal of Offshore and Polar Engineering, International Society of Offshore and Polar Engineers (ISOPE), Vol. 17, No. 4, pp. 301-308*.

[125] Van der Vegte, G.J., Wardenier, J., Qian, X.D., Choo, Y.S. (2008a). *Reanalysis of the moment capacity of CHS joints*. Proceedings of the 12th International Symposium on Tubular Structures. Shanghai, China, Taylor & Francis Group, pp. 579-588.

[126] Van der Vegte, G.J., Wardenier, J., Zhao, X.-L. and Packer, J.A. (2008b). *Evaluation of new CHS strength formulae to design strengths*. Proceedings of the 12th International Symposium on Tubular Structures. Shanghai, China, Taylor & Francis Group, pp. 313-322.

[127] Van der Vegte, G. V. D., Wardenier, J., & Puthli, R. S. (2010). FE analysis for welded hollow-section joints and bolted joints. In *Proceedings of the Institution of Civil Engineers-Structures and Buildings*, *163*(6), 427-437.

[128] Van der Vegte, G. J., & Wardenier, J. (2014). Evaluation of the recent IIW (2012) and ISO (2013) strength equations for axially loaded CHS K gap joints. *Steel Construction*, *7*(2), 97-106.

[129] Van Wingerde, A.M. (1992) The fatigue behaviour of T- and X-joints made of square hollow sections. *Heron*, *37*(2), 3-182.

[130] Van Wingerde, A. M., Packer, J. A., & Wardenier, J. (1995). Criteria for the fatigue assessment of hollow structural section connections. *Journal of Constructional Steel Research*, *35*(1), 71-115.

[131] Van Wingerde, A. M., Packer, J. A., & Wardenier, J. (1997). SCF formulae for fatigue design of K-connections between square hollow sections. *Journal of Constructional Steel Research*, *43*(1-3), 87-118.

[132] Van Wingerde, A. M., Packer, J. A., & Wardenier, J. (2001). Simplified SCF formulae and graphs for CHS and RHS K-and KK-connections. *Journal of Constructional Steel Research*, *57*(3), 221-252.

[133] Voth, A. P., & Packer, J. A. (2012). Numerical study and design of T-type branch plate-to-circular hollow section connections. *Engineering Structures*, *41*, 477-489.

[134] Wald, F., Kwasniewski, L., Gödrich, L., & Kurejková, M. (2014, May). Validation and verification procedures for connection design in steel structures. In *12th International Conference on Steel, Space and Composite Structures* (pp. 111-120).

[135] Wald, F., Šabatka, L., Kabeláč, J., Kolaja, D., & Pospíšil, M. (2015). Structural Analysis and Design of Steel Connections Using Component Based Finite Element Model (CBFEM). *Journal of Civil Engineering and Architecture*, *9*, 895-901.

[136] Wald, F., Sokol, Z., Steenhuis, C. M., & Jaspart, J. P. (2008). Component method for steel column base plates. *Heron*, *53*(1/2).

[137] Wald, F., Vild, M., Kuříková, M., Kožich, M., & Kabeláč, J. (2019, December). Component based Finite Element Design of Seismically Qualified Joints. In *Journal of Physics: Conference Series* (Vol. 1425, No. 1, p. 012002). IOP Publishing.

[138] Wald, F., Vild, M., Kuříková, M., Kabelác, M., Sekal, D., Maier, N., Da Silva. L.S., Couchaux, M. (2020). Component based finite element design of steel joints. *Civil Engineering Design*; 2: 78–89.

[139] Wang, B., Hu, N., Kurobane, Y., Makino, Y., & Lie, S. T. (2000). Damage criterion and safety assessment approach to tubular joints. *Engineering structures*, *22*(5), 424-434.

[140] Wang, W., Chen, Y., Meng, X., & Leon, R. T. (2010). Behaviour of thick-walled CHS X-joints under cyclic out-of-plane bending. *Journal of Constructional Steel Research*, *66*(6), 826-834.

[141] Wardenier, J., (1982). *Hollow Section Joints*. Delft University Press, Delft University of Technology, Delft, The Netherlands.

[142] Wardenier, J., Van der Vegte, G. J., & Liu, D. K. (2007). Chord stress function for rectangular hollow section X and T joints. In *ISOPE International Ocean and Polar Engineering Conference* (pp. ISOPE-I). ISOPE.

[143] Wardenier, J., van der Vegte, G. J., & Liu, D. K. (2007). Chord stress functions for K gap joints of rectangular hollow sections. *International Journal of Offshore and Polar Engineering*, *17*(03).

[144] Wardenier, J., van der Vegte, G. J., Makino, Y., & Marshall, P. W. (2008, September). Comparison of the new IIW (2008) CHS joint strength formulae with those of the previous IIW (1989) and the new API (2007). In *Proceedings of the 12th International Symposium on Tubular Structures, Shanghai. Taylor & Francis, London* (pp. 281-292).

[145] Wardenier, J., Packer, J.A., Zhao, X-L., Van der Vegte, G.J. (2010). Hollow Sections in Structural Applications. CIDECT: *Geneva, Switzerland*.

[146] Wei, F., Packer J.A. (2019). Experimental study of laterally offset RHS X-connections. In *Proceedings of the 17th International Symposium on Tubular Structures*. Singapore, Research Publishing Services, pp. 526-533.

[147] Jaspart, J. P. (2002). Design of structural joints in building frames. *Progress in Structural Engineering and Materials*, *4*(1), 18-34.

[148] Jaspart, J. P., & Weynand, K. (2001). Extension of the component method to joints in tubular construction. In *Ninth International Symposium and Euroconference on Tubular Structures*. AA Balkema Publishers.

[149] Weynand, K., Jaspart J.-P. (2002). *Application of the component method to joints between hollow and open sections*. CIDECT research project 5BM. Aachen & Liege.

[150] Weynand, K., Busse, E., & Jaspart, J. P. (2017). First practical implementation of the component method for joints in tubular construction. In *Tubular Structures XI* (pp. 139-145). Routledge.

[151] Xu, J., Zhao, J., Song, Z., & Liu, M. (2012). Prediction of ultimate bearing capacity of Tubular T-joint under fire using artificial neural networks. *Safety science*, *50*(7), 1495-1501.

[152] Yang, Z. M., Lie, S. T., & Gho, W. M. (2007). Failure assessment of cracked square hollow section T-joints. *International journal of pressure vessels and piping*, *84*(4), 244-255.

[153] Yu, Y. (1997). The Static Strength of Uniplanar and Multiplanar Connections in Rectangular Hollow Sections.

[154] Young, B., & Hancock, G. J. (2001). Design of cold-formed channels subjected to web crippling. *Journal of Structural engineering*, *127*(10), 1137-1144.

[155] Zhao, X-L., Hancock, G.J. (1990). Tubular T-joints Subject to Combined Actions. In *10th International Specialty Conference on Cold-Formed Steel Structures*, 545-573.

[156] Zhao, X. L., & Hancock, G. J. (1991). T-joints in rectangular hollow sections subject to combined actions. *Journal of Structural Engineering*, *117*(8), 2258-2277.

[157] Zhao, X. L., & Hancock, G. J. (1991). Plastic mechanism analysis of T-joints in RHS under concentrated force. *NASA STI/Recon Technical Report N*, *93*, 21029.

[158] Zhao, X-L., Hancock, G., (1993). Plastic Mechanism analysis of T-joints in RHS subject to combined bending and concentrated force. In *Proceedings of the Fifth International Symposium on Tubular Connections held at Nottingham*, UK, August, E & FN Spon, London, 345-352.

[159] Zhao, X. L., & Hancock, G. J. (1993). A theoretical analysis of the plastic-moment capacity of an inclined yield line under axial force. *Thin-Walled Structures*, *15*(3), 185-207.

[160] Zhao, X. L. (2000). Deformation limit and ultimate strength of welded T-joints in cold-formed RHS sections. *Journal of constructional steel research*, *53*(2), 149-165.

[161] Zhao, X. L. (2003). Yield line mechanism analysis of steel members and connections. *Progress in Structural Engineering and Materials*, *5*(4), 252-262.

[162] Zhao, X. L., Wardenier, J., Packer, J. A., & van der Vegte, G. J. (2008). New IIW (2008) static design recommendations for hollow section joints. In *Proc., 12th Int. Symp. on Tubular Structures* (pp. 261-269).

[163] Zhou, F., & Young, B. (2006). Yield line mechanism analysis on web crippling of cold-formed stainless steel tubular sections under two-flange loading. *Engineering Structures*, *28*(6), 880-892.

[164] Zoetemeijer, P. (1990). Summary of the research on bolted beam-to-column connections. *Stevin rapport 6-90-2*.

[165] Šabatka, L., Wald, F., Kabeláč, J., Gödrich, L., & Navrátil, J. (2014, May). Component based finite element model of structural connections. In *Proceedings of the 12th International Conference on Steel, Space & Composite Structures* (pp. 28-30).

ANNEX A. GEOMETRY RELATIONS

The present model is shown in Figure 6.1 and summarized in Table 6.1. The geometry derivations are given in this Appendix.

The web deflection Δ_ω is assumed to be proportional to β ($=\frac{b_1}{b_0}$) and Δ, i.e. $\Delta_\omega = \beta\Delta$. Also, it is assumed for simplification that the ratio $k = \frac{e_2}{e_1} \approx \frac{\sqrt{e_2^2 h_0^2 + J^2}}{\sqrt{e_1^2 h_0^2 + J^2}}$;

Distances are assumed as $n_2 = a_w + r_{ext} + s$ and $n_1 = b_0 - b_1 - n_2$, where a_w is the weld size, r_{ext} is the corner radius of RHS, $s = 0$ is the distance between a weld toe and an arc end of RHS chord section.

A.1. ROTATION ANGLE α – FIGURE 6.1, d

$$\sin\alpha = \frac{\Delta}{\sqrt{\Delta^2 + J^2}}$$

$$\alpha = \arcsin\frac{\Delta}{\sqrt{\Delta^2 + J^2}} \qquad \text{(A1)}$$

Virtual change of the angle α

α is an angle differential

$$\delta\alpha = \frac{J}{\Delta^2 + J^2}\,\delta\Delta$$

If $\frac{\Delta^2}{J^2} \ll 1$ is assumed then

$$\delta\alpha = \frac{1}{J}\,\delta\Delta \qquad \text{(A2)}$$

A.2. ROTATION ANGLE β_1 – FIGURE 6.1, c

$$\sin\beta_1 = \frac{\Delta}{\sqrt{\Delta^2 + n_1^2}}$$

$$\beta_1 = \arcsin\frac{\Delta}{\sqrt{\Delta^2 + n_1^2}} \qquad \text{(A3)}$$

Virtual change of the angle β_1

β_1 is an angle differential

$$\delta\beta_1 = \frac{n_1}{\Delta^2 + n_1^2}\,\delta\Delta$$

If $\frac{\Delta^2}{n_1^2} \ll 1$ is assumed then

$$\delta\beta_1 = \frac{1}{n_1}\,\delta\Delta \tag{A4}$$

A.3. ROTATION ANGLE β_2 – FIGURE 6.1, c

$$\sin\beta_2 = \frac{\Delta}{\sqrt{\Delta^2 + n_2^2}}$$

$$\beta_2 = \arcsin\frac{\Delta}{\sqrt{\Delta^2 + n_2^2}} \tag{A5}$$

Virtual change of the angle β_2

β_2 -angle differential

$$\delta\beta_2 = \frac{n_1}{\Delta^2 + n_2^2}\,\delta\Delta$$

If $\frac{\Delta^2}{n_2^2} \ll 1$ is assumed then

$$\delta\beta_2 = \frac{1}{n_2}\,\delta\Delta \tag{A6}$$

A.4. ROTATION ANGLE ψ_1 – FIGURE A.1

$$\tan\gamma_1 = \frac{J}{\sqrt{n_1^2 + \Delta^2}}$$

$$\angle obf = 90°$$

$$\overline{bf} = \sqrt{J^2 + n_1^2}$$

$$\overline{bo} = \overline{ob} = \frac{\overline{bf}}{\tan\gamma_1} = \frac{\sqrt{J^2 + n_1^2}}{\tan\gamma_1} = \frac{\sqrt{J^2 + n_1^2} * \sqrt{\Delta^2 + n_1^2}}{J}$$

$$\tan\gamma_4 = \frac{\sqrt{J^2+\Delta^2}}{n_1}$$

$$\overline{bp} = \overline{pb} = \overline{bf} * \tan\gamma_4 = \frac{\sqrt{J^2+n_1^2} * \sqrt{J^2+\Delta^2}}{n_1}$$

$$\overline{op}^2 = \overline{of}^2 + \overline{pf}^2 = \overline{ob}^2 + \overline{pb}^2 + 2\overline{bf}^2$$

$$\cos\psi_1 = \frac{\overline{bo}^2 + \overline{pb}^2 - \overline{op}^2}{2 * \overline{bo} * \overline{bp}} = \frac{\overline{bo}^2 + \overline{pb}^2 - \overline{bo}^2 - \overline{pb}^2 - 2\overline{bf}^2}{2 * \overline{bo} * \overline{bp}} = \frac{2\overline{bf}^2}{2 * \overline{bo} * \overline{bp}} =$$

$$= \frac{2 * \left(\sqrt{J^2+n_1^2}\right)^2 * n_1 J}{2 * \sqrt{J^2+n_1^2} * \sqrt{J^2+\Delta^2} * \sqrt{\Delta^2+n_1^2} * \sqrt{J^2+n_1^2}}$$

$$\cos\psi_1 = \frac{n_1 J}{\sqrt{J^2+\Delta^2} * \sqrt{\Delta^2+n_1^2}}$$

$$\psi_1 = \arccos\left(\frac{n_1 J}{\sqrt{J^2+\Delta^2} * \sqrt{\Delta^2+n_1^2}}\right) \quad \text{(A7)}$$

Virtual change of the angle Ψ_1

ψ_1 -angle differential

$$\delta\psi_1 = \frac{n_1 J(n_1^2+J^2+2\Delta^2)}{(n_1^2+J^2)(\Delta^2+J^2)\sqrt{n_1^2+J^2+\Delta^2}}\,\delta\Delta$$

Assuming $\frac{\Delta^2}{n_1^2} \ll 1$; $\frac{\Delta^2}{J^2} \ll 1$ and $\frac{\Delta^2}{n_1^2+J^2} \ll 1$

$$\delta\psi_1 = \frac{\sqrt{n_1^2+J^2}}{n_1 J}\,\delta\Delta \quad \text{(A8)}$$

A.5. ROTATION ANGLE ψ_2 – FIGURE A.1

$$\tan\gamma_7 = \frac{\sqrt{J^2+\Delta^2}}{n_2}$$

$$\tan\gamma_8 = \frac{J}{\sqrt{n_2^2+\Delta^2}}$$

$$\cos\psi_2 = \frac{\overline{ct}^2 + \overline{cs}^2 - \overline{st}^2}{2 * \overline{ct} * \overline{cs}}$$

$$\overline{cg} = \sqrt{J^2+n_2^2}$$

$$\overline{ct} = \overline{tc} = \frac{\overline{cg}}{\tan\gamma_8} = \frac{\sqrt{J^2+n_2^2}}{\tan\gamma_8} = \frac{\sqrt{J^2+n_2^2} * \sqrt{\Delta^2+n_2^2}}{J}$$

$$\overline{cs} = \overline{sc} = \overline{cg} * \tan\gamma_7 = \frac{\sqrt{J^2+n_2^2} * \sqrt{J^2+\Delta^2}}{n_2}$$

$$\overline{st}^2 = \overline{sg}^2 + \overline{tg}^2 = \overline{cs}^2 + \overline{ct}^2 + 2\overline{cg}^2$$

$$\cos\psi_2 = \frac{\overline{ct}^2 + \overline{cs}^2 - \overline{st}^2}{2 * \overline{ct} * \overline{cs}} = \frac{\overline{ct}^2 + \overline{sc}^2 - \overline{cs}^2 - \overline{ct}^2 - 2\overline{cg}^2}{2 * \overline{ct} * \overline{cs}} = \frac{-2\overline{cg}^2}{2 * \overline{ct} * \overline{cs}} =$$

$$= \frac{-2 * \left(\sqrt{J^2+n_2^2}\right)^2 * n_2 J}{2 * \sqrt{J^2+n_2^2} * \sqrt{J^2+\Delta^2} * \sqrt{\Delta^2+n_2^2} * \sqrt{J^2+n_2^2}}$$

$$-\cos\psi_2 = \cos\psi_2 = \frac{n_2 J}{\sqrt{J^2+\Delta^2} * \sqrt{\Delta^2+n_2^2}}$$

$$\psi_2 = \arccos\left(\frac{n_2 J}{\sqrt{J^2+\Delta^2} * \sqrt{\Delta^2+n_2^2}}\right) \quad \text{(A9)}$$

Virtual change of the angle Ψ_2

ψ_2 is an angle differential

$$\delta\psi_2 = \frac{n_2 J(n_2^2 + J^2 + 2\Delta^2)}{(n_2^2+J^2)(\Delta^2+J^2)\sqrt{n_2^2+J^2+\Delta^2}}\,\delta\Delta$$

Assuming $\frac{\Delta^2}{n_2^2} \ll 1$; $\frac{\Delta^2}{J^2} \ll 1$ and $\frac{\Delta^2}{n_2^2+J^2} \ll 1$

$$\delta\psi_2 = \frac{\sqrt{n_2^2+J^2}}{n_2 J}\,\delta\Delta \quad \text{(A10)}$$

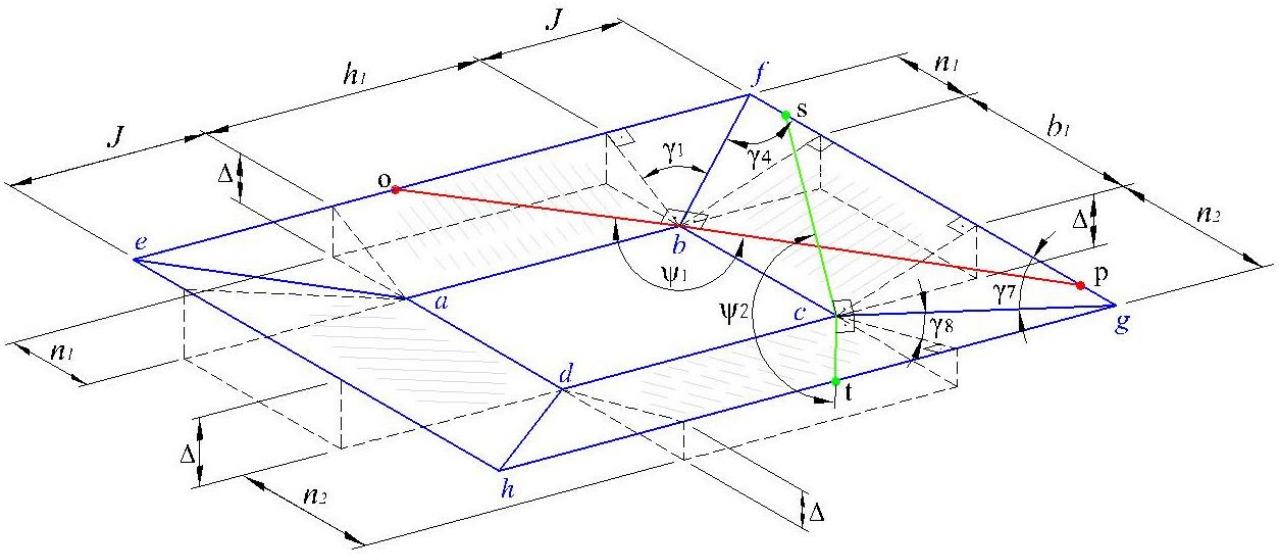

a) Main Scheme

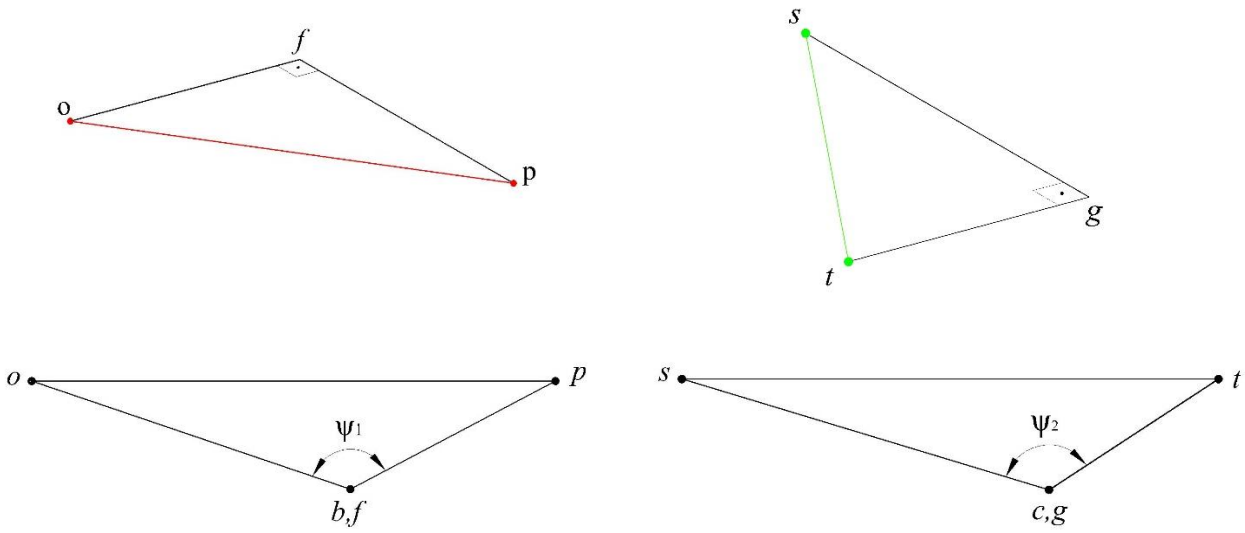

b) Supporting schemes

Figure A.1 Rotation Angles Ψ_1 and Ψ_2

A.6. ROTATION ANGLE ψ_3 – FIGURE A.2

$$\cos\psi_3 = \frac{\overline{jq}^2 + \overline{jr}^2 - \overline{qr}^2}{2 * \overline{jq} * \overline{jr}}$$

$$\overline{jr}^2 = \overline{gq}^2 + \overline{gr}^2 = \overline{qj}^2 + \overline{jr}^2 + 2\overline{gj}^2$$

$$\frac{\overline{jg}}{\overline{qj}} = \tan\gamma_2 \rightarrow \overline{qj} = \frac{\overline{jg}}{\tan\gamma_2}$$

$$\tan\gamma_2 = \frac{J}{\sqrt{\Delta_w^2 + e_1^2}}$$

$$\frac{\overline{jg}}{\overline{qj}} = \tan\gamma_2 \rightarrow \overline{qj} = \frac{\overline{jg}}{\tan\gamma_2}$$

$$\tan\gamma_5 = \frac{\sqrt{J^2 + \Delta_w^2}}{e_1}$$

$$\frac{\overline{jr}}{\overline{jg}} = \tan\gamma_5 \rightarrow \overline{jr} = \overline{jg}\ \tan\gamma_5$$

$$\cos\psi_3 = \frac{\overline{qj}^2 + \overline{jr}^2 - \overline{jq}^2 - \overline{jr}^2 - 2\overline{qj}^2}{2 * \overline{jq} * \overline{jr}} = \frac{-2\overline{gj}^2}{2 * \overline{jq} * \overline{jr}} = \frac{-\overline{gj}^2}{\frac{\overline{gj}}{\tan\gamma_2} * \overline{gj} * \tan\gamma_5} = -\frac{\tan\gamma_2}{\tan\gamma_5}$$

$$-\cos\psi_3 = \cos\psi_3 = \frac{\tan\gamma_2}{\tan\gamma_5} = \frac{e_1 * J}{\sqrt{J^2 + \Delta^2} * \sqrt{\Delta^2 + n_2^2} * \sqrt{J^2 + n_2^2}}$$

$$\cos\psi_3 = \frac{n_2 J}{\sqrt{J^2 + \Delta_w^2} * \sqrt{\Delta_w^2 + e_1^2}}$$

$$\psi_3 = \arccos\left(\frac{n_2 J}{\sqrt{J^2 + \Delta_w^2} * \sqrt{\Delta_w^2 + e_1^2}}\right) \quad \text{(A11)}$$

Virtual change of the angle Ψ_3

ψ_3 is an angle differential

$$\delta\psi_3 = \frac{\sqrt{e_1^2 h_0^2 + J^2}}{n_1 J}\ \delta\Delta \quad \text{(A12)}$$

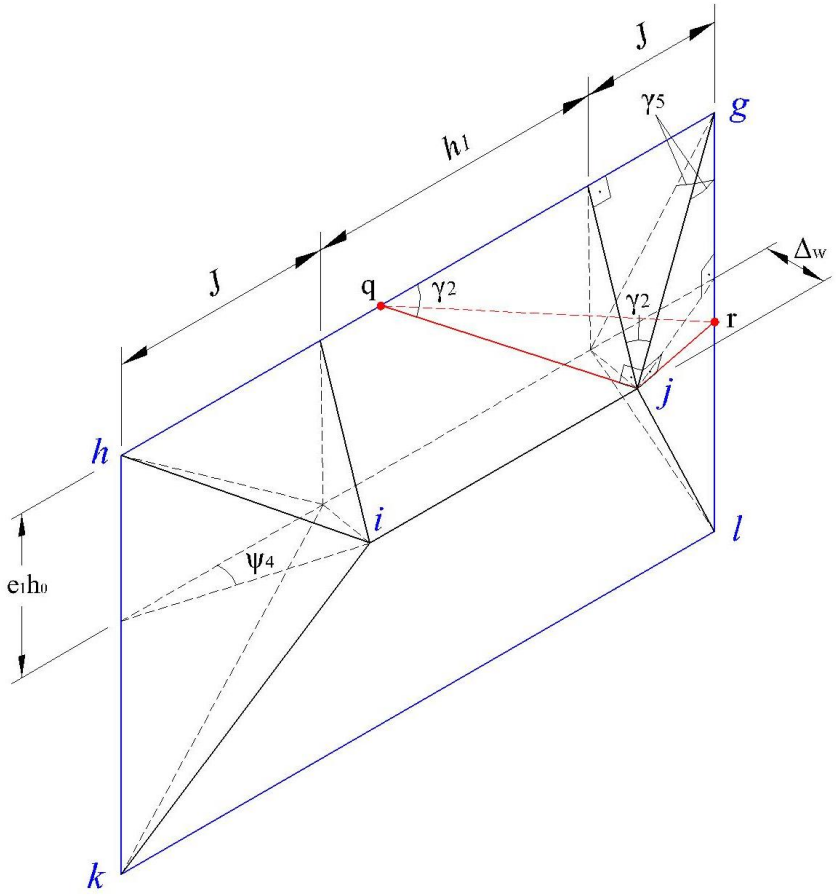

a) Main Scheme

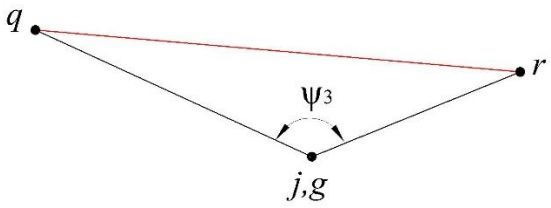

b) Supporting scheme

Figure A.2 Rotation Angle Ψ_3 and Ψ_4

A.7. ROTATION ANGLE ψ_4 – FIGURE A.2

$$\tan\psi_4 = \frac{\Delta_w}{J} = \frac{\beta\Delta}{J}$$

$$\psi_4 = \arctan\left(\frac{\beta\Delta}{J}\right) \quad \text{(A13)}$$

Virtual change of the angle Ψ_4

ψ_4 -angle differential

$$\delta\psi_4 = \frac{\beta/J}{1+\left(\frac{\beta\Delta}{J}\right)^2}\,\delta\Delta$$

If $\frac{\Delta^2}{J^2} \ll 1$ is assumed then

$$\delta\psi_4 = \frac{\beta}{J}\,\delta\Delta \quad \text{(A14)}$$

A.8. ROTATION ANGLE ψ_5 – FIGURE A.3

$$\cos\psi_5 = \frac{\overline{sj}^2 + \overline{tj}^2 - \overline{st}^2}{2 * \overline{sj} * \overline{tj}}$$

$$\overline{st}^2 = \overline{sl}^2 + \overline{tl}^2 = \overline{sj}^2 + \overline{tj}^2 + 2\overline{jl}^2$$

$$\frac{\overline{jl}}{\overline{sj}} = \tan\gamma_3 \rightarrow \overline{sj} = \frac{\overline{jl}}{\tan\gamma_3}$$

$$\tan\gamma_3 = \frac{J}{\sqrt{(1-e_1)^2 + \Delta_w^2}}$$

$$\frac{\overline{tj}}{\overline{jl}} = \tan\gamma_6 \rightarrow \overline{tj} = \overline{jl} * \tan\gamma_6$$

$$\tan\gamma_6 = \frac{\sqrt{J^2 + \Delta_w^2}}{1-e_1}$$

$$\cos\psi_5 = \frac{\overline{sj}^2 + \overline{tj}^2 - \overline{sj}^2 - \overline{tj}^2 - 2\overline{jl}^2}{2 * \overline{sj} * \overline{tj}} = \frac{-2\overline{jl}^2}{2 * \frac{\overline{jl}}{\tan\gamma_3} * \overline{jl} * \tan\gamma_6} = -\frac{\tan\gamma_3}{\tan\gamma_6}$$

$$-\cos\psi_5 = \cos\psi_5 = \frac{\tan\gamma_3}{\tan\gamma_5} = \frac{J*(1-e_1)}{\sqrt{J^2+\Delta_w^2}*\sqrt{(1-e_1)^2+\Delta_w^2}}$$

$$\cos\psi_5 = \frac{J*(1-e_1)}{\sqrt{J^2+\Delta_w^2}*\sqrt{(1-e_1)^2+\Delta_w^2}}$$

$$\psi_5 = \arccos\left(\frac{J*(1-e_1)}{\sqrt{J^2+\Delta_w^2}*\sqrt{(1-e_1)^2+\Delta_w^2}}\right) \quad \text{(A15)}$$

Virtual change of the angle Ψ_5

Taking into account that $e_1 = \frac{n_1}{h_0}\beta$ and if $\frac{\Delta^2}{J^2} \ll 1$ is assumed then

ψ_5 is an angle differential

$$\delta\psi_5 = \left[\frac{\sqrt{(1-e_1)^2h_0^2+J^2}}{n_1 J} * \frac{e_1}{1-e_1}\right]\delta\Delta \quad \text{(A16)}$$

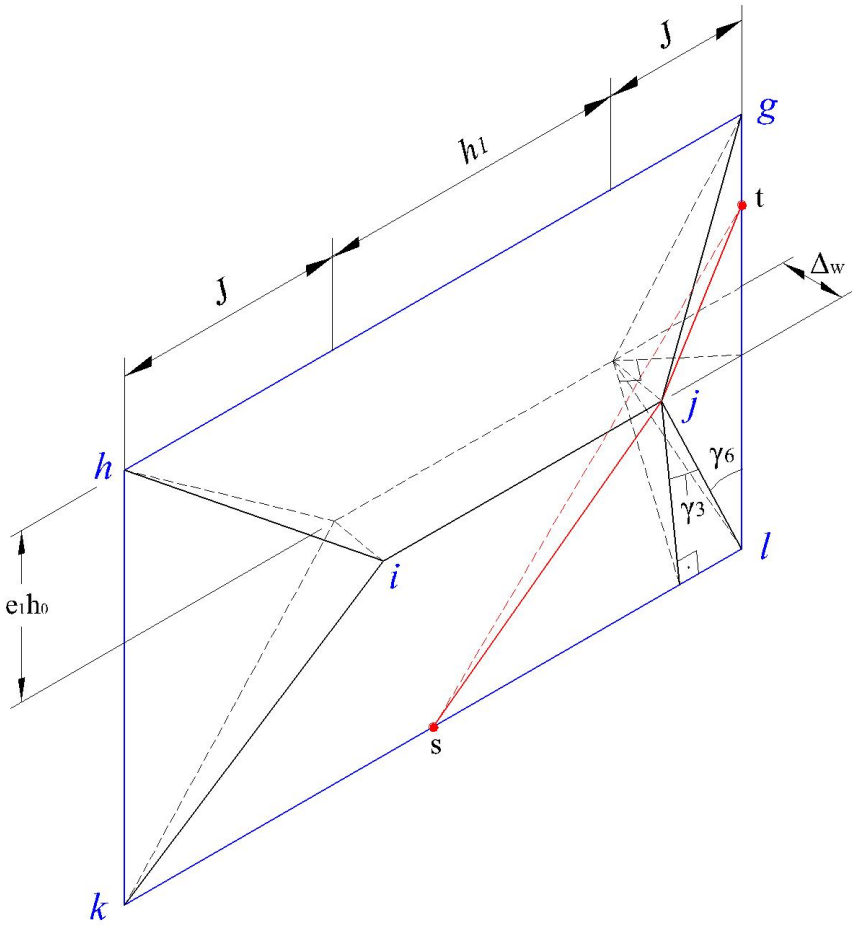

a) Main Scheme

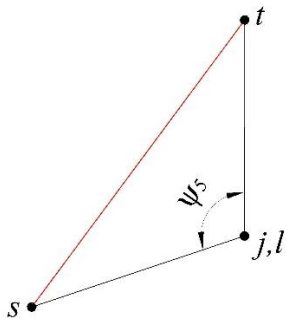

b) Supporting scheme

Figure A.3 Rotation Angles Ψ_5

A.9. ROTATION ANGLE ψ_6 – FIGURE A.4

$$\tan\psi_6 = \frac{\overline{uv}}{\overline{ov}}$$

$$\sin\gamma_{11} = \frac{\overline{fv}}{\overline{fm}} = \frac{\overline{ov}}{\overline{vm}} \quad \rightarrow \quad \overline{ov} = \frac{\overline{fv} * \overline{vm}}{\overline{fm}} = \frac{e_2 h_0 * J}{\sqrt{J^2 + (e_2 h_0)^2}}$$

$$\overline{uv} = \Delta_w$$

$$\tan\psi_6 = \frac{\Delta_w \sqrt{J^2 + (e_2 h_0)^2}}{J * e_2 h_0}$$

$$\psi_6 = \arctan\left(\frac{\beta\Delta * \sqrt{J^2 + (e_2 h_0)^2}}{J * e_2 h_0}\right) \tag{A17}$$

Virtual change of the angle Ψ_3

ψ_6 is an angle differential

$$\delta\psi_6 = \frac{\beta\sqrt{J^2 + e_2^2 h_0^2}}{e_2 h_0 J}\ \delta\Delta \tag{A18}$$

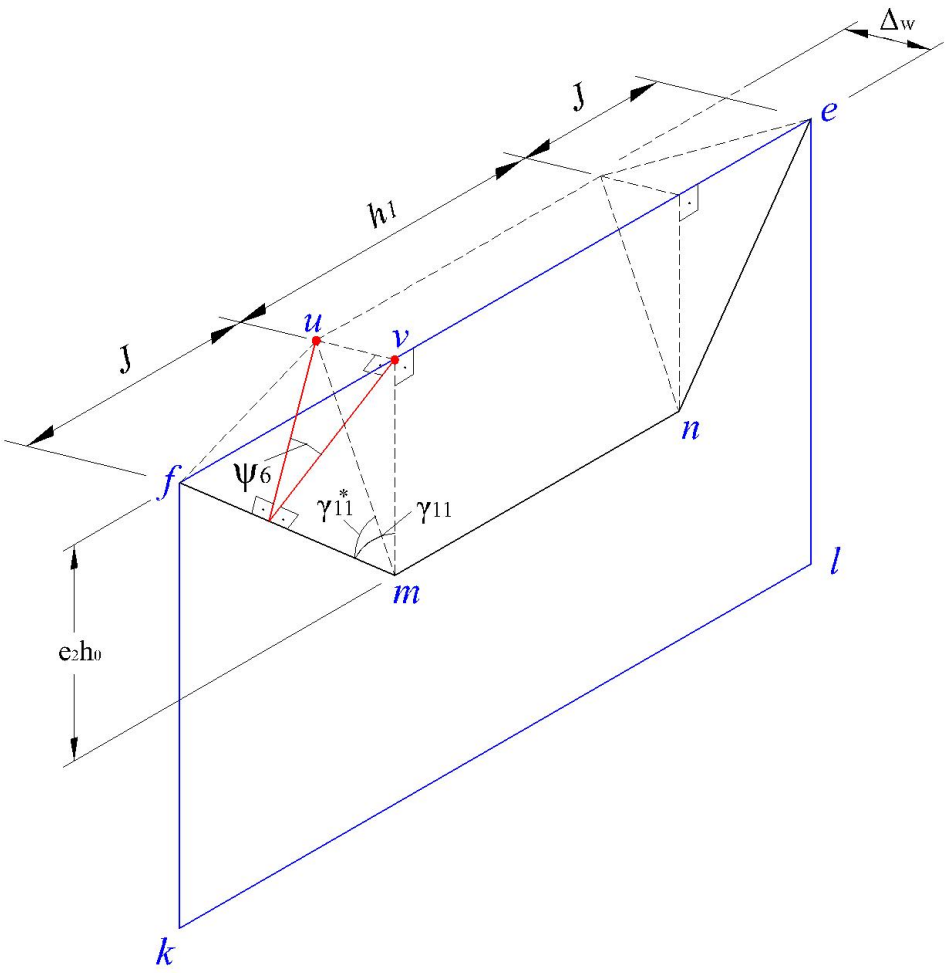

a) Main Scheme

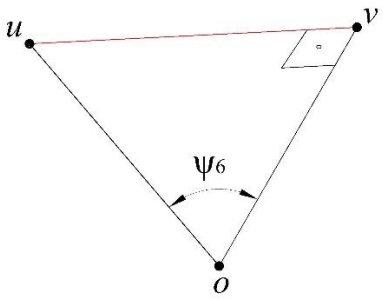

b) Supporting scheme

Figure A.4 Rotation Angles Ψ_6

A.10. ROTATION ANGLE θ_1 – FIGURE 6.1, c

$$\sin\theta_1 = \frac{\Delta_w}{\sqrt{\Delta_w^2 + (1-e_1)^2 h_0^2}}$$

Accounting for $\beta = \frac{e_1 h_0}{n_1}$ and virtual displacement $\Delta_w = \Delta * \beta = \Delta * \frac{e_1 h_0}{n_1}$

$$\sin\theta_1 = \frac{\Delta * \frac{e_1 h_0}{n_1}}{\sqrt{\Delta^2 * \left(\frac{e_1 h_0}{n_1}\right)^2 + (1-e_1)^2 h_0^2}} = \frac{\Delta * \frac{e_1 h_0}{n_1}}{\frac{e_1 h_0}{n_1}\sqrt{\Delta^2 + \frac{(1-e_1)^2 n_1^2}{e_1^2}}}$$

Finally

$$\sin\theta_1 = \frac{\Delta}{\sqrt{\Delta^2 + \frac{(1-e_1)^2 n_1^2}{e_1^2}}}$$

$$\theta_1 = \sin^{-1}\left(\frac{\Delta}{\sqrt{\Delta^2 + \frac{(1-e_1)^2 n_1^2}{e_1^2}}}\right) \quad \text{(A19)}$$

Virtual change of the angle θ_1

Taking into account that $e_1 = \frac{n_1}{h_0}\beta$ and if $\frac{\Delta^2}{J^2} \ll 1$ is assumed then

θ_1 is an angle differential

$$\delta\theta_1 = \left[\frac{e_1}{n_1(1-e_1)}\right]\delta\Delta \quad \text{(A20)}$$

Virtual change of the angle $\beta_2 + \theta_1$

$$\delta(\beta_2 + \theta_1) = \left(\frac{1}{n_2} + \frac{e_1}{n_1(1-e_1)}\right)\delta\Delta = \frac{n_1(1-e_1) + n_2 e_1}{n_1 n_2 (1-e_1)}\delta\Delta \quad \text{(A21)}$$

A.11. ROTATION ANGLE θ_2 – FIGURE 6.1, c

$$\sin\theta_2 = \frac{\Delta_w}{\sqrt{\Delta_w^2 + e_2^2 h_0^2}}$$

Assuming $A = \frac{e_2 n_1}{e_1}$

$$\sin\theta_2 = \frac{\Delta * \frac{e_1 h_0}{n_1}}{\sqrt{\Delta^2 * \left(\frac{e_1 h_0}{n_1}\right)^2 + e_2^2 h_0^2}} = \frac{\Delta}{\sqrt{\Delta^2 + \frac{e_2^2 n_1^2}{e_1^2}}}$$

Finally

$$\sin\theta_2 = \frac{\Delta}{\sqrt{\Delta^2 + A^2}}$$

$$\theta_2 = \sin^{-1}\left(\frac{\Delta}{\sqrt{\Delta^2 + A^2}}\right) \qquad \text{(A22)}$$

Virtual change of the angle θ_2

θ_2 -angle differential

$$\delta\theta_2 = \left[\frac{A}{\Delta^2 + A^2}\right] \delta\Delta$$

Taking into account that $\frac{\Delta}{A} \ll 1$ is assumed then

$$\delta\theta_2 = \frac{1}{A}\,\delta\Delta = \frac{e_1}{e_2 n_1}\delta\Delta \qquad \text{(C23)}$$

Details for each i-th hinge and virtual work are collected in Table 5.1.

A.12. DEFINITION OF THE MODEL SIZE *J*

Membrane effect is neglected.

Size model is defined from the minimum of the sum of derivatives

$$\sum_{i=1}^{13} k_i \frac{\Delta P_i}{\Delta J} = 0.0.$$

Where k_i is the number of *i*-th hinge, $\frac{\Delta P_i}{\Delta J}$ are derivatives from Table 6.1.

$$M_p \times \left[2 * \left(-\frac{b_1}{J^2} - \frac{b_0}{J^2}\right) + 2 * \left(\frac{1}{n_1} - \frac{n_1}{J^2}\right) + 2 * \left(\frac{1}{n_2} - \frac{n_2}{J^2}\right) + 2 * \left(\frac{1}{n_1} - \frac{e_1^2 h_0^2}{n_1 J^2}\right) + 2 * \frac{e_1}{(1-e_1)} * \left(\frac{1}{n_1} - \frac{(1-e_1)^2 h_0^2}{n_1 J^2}\right) + \frac{2e_1}{n_1(1-e_1)} + 2 * \beta\left(\frac{1}{e_2 h_0} + \frac{e_2 h_0}{J^2}\right) - 2 * \frac{\beta h_0}{J^2}\right] = 0$$

After reduction by $2 * M_p$

$$-\frac{b_1 + b_0}{J^2} + \frac{1}{n_1} - \frac{n_1}{J^2} + \frac{1}{n_2} - \frac{n_2}{J^2} + \frac{1}{n_1} - \frac{e_1^2 h_0^2}{n_1 J^2} + \frac{e_1}{n_1(1-e_1)} - \frac{e_1 h_0^2 (1-e_1)}{n_1 J^2} + \frac{e_1}{n_1(1-e_1)} + \frac{\beta}{e_2 h_0} + \frac{\beta e_2 h_0}{J^2} - \frac{\beta h_0}{J^2} = 0$$

After multiplication by J^2

$$-b_1 - b_0 + \frac{J^2}{n_1} - n_1 + \frac{J^2}{n_2} - n_2 + \frac{J^2}{n_1} - \frac{e_1^2 h_0^2}{n_1} + \frac{J^2 e_1}{n_1(1-e_1)} - \frac{e_1 h_0^2 (1-e_1)}{n_1} + \frac{J^2 e_1}{n_1(1-e_1)} + \frac{J^2 \beta}{e_2 h_0} + \beta e_2 h_0 - \beta h_0 = 0$$

Finally, quadratic equation for J-size is

$$\frac{J^2}{n_1} + \frac{J^2}{n_2} + \frac{J^2}{n_1} + \frac{J^2 e_1}{n_1(1-e_1)} + \frac{J^2 e_1}{n_1(1-e_1)} + \frac{J^2 \beta}{e_2 h_0} + \beta e_2 h_0 - b_1 - b_0 - n_1 - n_2 - \frac{e_1^2 h_0^2}{n_1} - \frac{e_1 h_0^2 (1-e_1)}{n_1} - \beta h_0 = 0$$

Equation coefficients are

$$a = \frac{2}{n_1} + \frac{1}{n_2} + \frac{2e_1}{n_1(1-e_1)} + \frac{\beta}{e_2 h_0}$$

$$b = 0$$

$$c = -1 * \left(b_1 + b_0 + n_1 + n_2 + \frac{e_1^2 h_0^2}{n_1} + \frac{e_1 h_0^2 (1-e_1)}{n_1} + \beta h_0 - \beta e_2 h_0\right)$$

Solution of the equation

$$J = \sqrt{\frac{b_1 + b_0 + n_1 + n_2 + \frac{e_1^2 h_0^2}{n_1} + \frac{e_1 h_0^2 (1-e_1)}{n_1} + \beta h_0 - \beta e_2 h_0}{\frac{2}{n_1} + \frac{1}{n_2} + \frac{2e_1}{n_1(1-e_1)} + \frac{\beta}{e_2 h_0}}}$$

A.13. DEFINITION OF THE MODEL SIZE *J* FOR X-CONNECTIONS TO CHECK THE MODEL [11]

Membrane effect is neglected. Yield lines No.4 and No.6 are excluded.

Size model is defined from the minimum of the sum of derivatives

$$\sum_{i=1}^{8} k_i \frac{\Delta P_i}{\Delta J} = 0.0.$$

Where k_i is the number of *i*-th hinge, $\frac{\Delta P_i}{\Delta J}$ are derivatives from Table 6.1.

$$M_p \times \left[4 * \left(-\frac{b_1}{J^2} - \frac{b_0}{J^2}\right) + 4 * \left(\frac{1}{n_1} - \frac{n_1}{J^2}\right) + 2 * \left(\frac{1}{n_1} - \frac{e_1^2 h_0^2}{n_1 J^2}\right) + 2 * \frac{e_1}{(1-e_1)} * \left(\frac{1}{n_1} - \frac{(1-e_1)^2 h_0^2}{n_1 J^2}\right) + 2 * \frac{2e_1}{n_1(1-e_1)} + 4 * \beta\left(\frac{1}{e_2 h_0} + \frac{e_2 h_0}{J^2}\right) - 2 * \frac{\beta h_0}{J^2}\right] = 0$$

After reduction by $4 * M_p$

$$-\frac{b_1 + b_0}{J^2} + \frac{1}{n_1} - \frac{n_1}{J^2} + \frac{1}{2n_1} - \frac{e_1^2 h_0^2}{2n_1 J^2} + \frac{e_1}{2n_1(1-e_1)} - \frac{e_1 h_0^2 (1-e_1)}{2n_1 J^2} + \frac{e_1}{n_1(1-e_1)} + \frac{\beta}{e_2 h_0} + \frac{\beta e_2 h_0}{J^2} - \frac{\beta h_0}{2J^2} = 0$$

After multiplication by J^2

$$-b_1 - b_0 + \frac{J^2}{n_1} - n_1 + \frac{J^2}{2n_1} - \frac{e_1^2 h_0^2}{2n_1} + \frac{J^2 e_1}{2n_1(1-e_1)} - \frac{e_1 h_0^2 (1-e_1)}{2n_1} + \frac{J^2 e_1}{n_1(1-e_1)} + \frac{J^2 \beta}{e_2 h_0} + \beta e_2 h_0 - \frac{\beta h_0}{2} = 0$$

Finally, quadratic equation for J-size is

$$\frac{J^2}{n_1} + \frac{J^2}{2n_1} + \frac{J^2 e_1}{2n_1(1-e_1)} + \frac{J^2 e_1}{n_1(1-e_1)} + \frac{J^2 \beta}{e_2 h_0} - b_1 - b_0 - n_1 - \frac{e_1^2 h_0^2}{2n_1} - \frac{e_1 h_0^2 (1-e_1)}{2n_1} - \frac{\beta h_0}{2} + \beta e_2 h_0 = 0$$

Equation coefficients are

$$a = \frac{1}{n_1} + \frac{1}{2n_2} + \frac{e_1}{2n_1(1-e_1)} + \frac{e_1}{n_1(1-e_1)} + \frac{\beta}{e_2 h_0}$$

$$b = 0$$

$$c = -1 * \left(b_1 + b_0 + n_1 + \frac{e_1^2 h_0^2}{2n_1} + \frac{e_1 h_0^2 (1-e_1)}{2n_1} + \frac{\beta h_0}{2} - \beta e_2 h_0\right)$$

Solution of the equation

$$J = \sqrt{\frac{b_1 + b_0 + n_1 + \frac{e_1^2 h_0^2}{2n_1} + \frac{e_1 h_0^2 (1 - e_1)}{2n_1} + \frac{\beta h_0}{2} - \beta e_2 h_0}{\frac{1}{n_1} + \frac{1}{2n_2} + \frac{e_1}{2n_1(1 - e_1)} + \frac{e_1}{n_1(1 - e_1)} + \frac{\beta}{e_2 h_0}}}$$